

**DYNAMIC TRANSDUCTION CHARACTERIZATION OF  
MAGNETOSTRICTIVE ACTUATORS**

by

Anthony E. Ackerman

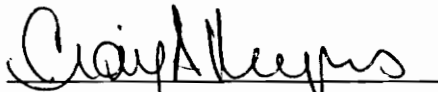
Thesis submitted to the Faculty of the  
Virginia Polytechnic Institute and State University  
in partial fulfillment of the requirements for the degree of

MASTER OF SCIENCE

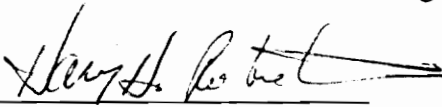
in

Mechanical Engineering

APPROVED:



Dr. Craig A. Rogers, Chairman



Dr. Harry H. Robertshaw



Dr. Chen Liang

December, 1993  
Blacksburg, Virginia

C.2

LO  
5655  
V855  
1993  
A224  
C.2

DYNAMIC TRANSDUCTION CHARACTERIZATION OF  
MAGNETOSTRICTIVE ACTUATORS

by

Anthony E. Ackerman

Committee Chairman: Dr. Craig A. Rogers

Mechanical Engineering

**Abstract**

The objective of this thesis is to develop an analysis approach for formulation of transduction or input/output representations for magnetostrictive actuators. This transduction model is developed through application of an electro-magneto-mechanical impedance modeling approach which combines both the mechanical dynamics and coupled behavior of the actuator device. Lumped and continuous mechanical impedance elements model the actuator dynamics and the constitutive relationships for Terfenol-D characterize the electro-magneto-mechanical interaction. Experimental analysis of a Terfenol-D actuator serves to verify the developed models and provides an indication of actuator non-linearity.

The developed transduction model allows for various device behavior analysis including dissipative power consumption, force and stroke output, and efficiency as a transducer. An actuator design strategy based upon the dynamics of the actuator and a driven external system is presented and allows for analysis of various actuator behaviors in terms of device parameters. The Terfenol-D actuator as a collocated actuator/sensor is also made possible with the transduction model.

# Acknowledgements

I would like to thank the Air Force Office of Scientific Research (AFOSR) for providing financial sponsorship of this research. Also, I would like to thank Dr. Zheng Geng at Intelligent Automation, Inc. for supplying the actuator and providing many needed actuator parameters.

I would like to thank Dr. Craig Rogers for the fantastic facilities and equipment provided for the students at CIMSS. I also want to thank Dr. Chen Liang, Dr. Zaffir Chaudhry, and Fanping Sun for their help and advice in many stages of this thesis. And I want to thank all my friends at CIMSS for the many hours of conversation and humor which helped pull me through some of the difficult times. Thanks again to Craig Dempsey, Dave Kiel, Frederic ("Go Home") Lalande, Tony Ganino, Chris Waldhart, and many others.

And I also want to give a very special thanks to Jacqueline Serbu whose friendship, love, and support were instrumental in my successful completion of this thesis. Thank you again Jackie...

# Contents:

Chapter 1: Introduction	1
1.1 Terfenol-D As A Magnetostrictive Element	2
1.1.1 Physics of the Magnetostrictive Effect	2
1.1.2 Characterization of Terfenol-D Material Properties	5
1.2 General Applications of Terfenol-D	14
1.3 Terfenol-D Actuators	15
1.3.1 Actuator Layout and Parameters	15
1.3.2 Actuator Modeling Literature Review	16
1.3.3 Experimental Usage of the Terfenol-D Actuator	18
Literature Review	
1.4 Transducer Literature Review	19
1.5 Scope and Objectives	25
1.6 Thesis Outline	26
Chapter 2: Development of a Dynamic Actuator Model	28
2.1 Introduction	28
2.2 Discussion of Lumped Impedances	30
2.3 Actuator Subsystem Representation	34
2.4 Mechanical Aspects	35
2.5 Electrical Aspects	58
2.6 Description of Electro-magneto-mechanical Interaction	61
2.7 Development of a Transduction Expression	64
2.8 Analysis of the Terfenol-D Transducer	73

2.9	Creating Transfer Function Representations	75
2.10	Determination of Actuator Mechanical and Electrical Properties	77
2.11	Determining the Lumped Fixture Impedance	82
2.12	Concluding Remarks	83
Chapter 3: Experimental Analysis		85
3.1	Experimental Setup	85
3.2	Model Evaluation	89
3.3	Actuator Time-domain Behavior and Non-linearities	110
3.4	Concluding Remarks	115
Chapter 4: Hybrid Actuator/Structure Design Strategy		119
Chapter 5: Conclusions and Future Work		116
5.1	Summary of the Thesis	116
5.2	Contributions	119
5.3	Future Work	130
References		134
Appendix A: Non-linear Time Domain/Spectra of Actuator Behavior		138
Appendix B: Matlab and Mathematica Codes		154
Vita		174

# List of Figures:

<b>Number</b>	<b>Title</b>	<b>Page</b>
1.1	Increase in Material Magnetization With Respect to an Applied Magnetic Field	3
1.2	The Magnetic Flux Density Variation With Applied Magnetic Field for a Ferromagnetic Material	6
1.3	The Relationship Between Induced Strain and Induced Flux Density for Terfenol-D	8
1.4	Induced Strain as a Function of Applied Magnetic Field and Mechanical Prestress	8
1.5	The Relationship Between Terfenol-D Elastic Modulus and Material Strain for Varying Driving Fields	9
1.6	Decreasing Available Magnetostriction at Magnetic Saturation for High Temperatures With 7.6 MPa Prestress	10
1.7	The Effects of Stoichiometry Variation on Available Magnetostriction for a Range of Temperatures	11
1.8	Illustration of a Bias Point for Linear, Bi-directional Operation of a Terfenol-D Based Actuator	12
1.9	Exploded View of the Modeled Terfenol-D Actuator	16
1.10	Two-port Network Descriptions of Transducer Operation	23
2.1	General Representation of Mechanical Impedance	29
2.2	Representation of a Lumped Mass	30
2.3	Representation of a Lumped Stiffness	31
2.4	Representation of a Lumped Damper	32

2.5	Parallel and Series Configurations for Lumped Impedance Elements	33
2.6	Terfenol-D Actuator Configuration Showing Mechanical and Electrical Subsystems	34
2.7	Complete Mechanical Impedance Diagram	35
2.8	Representation of the Terfenol-D Rod With a Fixed Boundary Condition and Applied External Force	37
2.9	Impedance Model of the Terfenol-D Actuator	40
2.10	Condensed Actuator Impedance Model	41
2.11	Actuator Impedance Configuration With Lumped Rod and External Impedances	46
2.12	Impedance Model of the Terfenol-D Actuator	47
2.13	Actuator Output Rod With Fixed Boundary Condition	49
2.14	Blocked and Free Actuator End Configurations	51
2.15	The Magnetic Flux Created By a Current Passing Through a Coil	59
2.16	Mechanical Impedance Configuration	65
2.17	Collapsed Mechanical Impedance Configuration	66
2.18	Schematic of the Terfenol-D Actuator	78
2.19	Dimensions of the Actuator Output Rod	79
2.20	Fixture Stiffness Configuration	82
2.21	Complete Fixture Impedance Configuration	83
3.1	Macintosh Quadra 950 and WCA Zonic Experimental Setup Used for Data Acquisition and Signal Processing	86
3.2	Experimental WCA Setup for Obtaining the Stroke to Current Transfer Function	87



3.3	HP 4194A Impedance Analyzer Using a 486 Computer for Actuator Electrical Impedance Data Acquisition	88
3.4	HP 4194A Impedance Analyzer Used for Coil Electrical Impedance Data Acquisition	88
3.5	Free-stroke to Current Experimental Transfer Function Taken From the WCA	89
3.6	Free-stroke to Voltage Experimental Transfer Function Taken From the WCA	94
3.7	Correlated Free-stroke to Voltage Transfer Function for the Terfenol-D Actuator	95
3.8	The Experimental Real Electrical Impedance of the Actuator Coil Taken With the HP 4194A Analyzer	98
3.9	The Experimental Imaginary Electrical Impedance of the Actuator Coil Taken With the HP 4194A Analyzer	99
3.10	The Correlated Real Electrical Impedance of the Terfenol-D Actuator Taken With the HP 4194A Analyzer	100
3.11	The Correlated Imaginary Electrical Impedance of the Terfenol-D Actuator Taken With the HP 4194A Analyzer	100
3.12	Free-stroke to Voltage Transfer Function Comparison Using Theoretical and Experimental Electrical Impedances	101
3.13	Theoretical Actuator Blocking Force to Voltage Transfer Function	102
3.14	Complete Actuator Impedance Configuration	103
3.15	Rod Input Force ( $F_3$ ) to Voltage Transfer Function	104
3.16	The Dynamic Stress Magnitude Developed in the Terfenol-D Rod	105

3.17	The Total State of Stress in the Terfenol-D Rod	107
3.18	Terfenol-D Actuator Dissipative Power Consumption for Blocked and Free Boundary Conditions	108
3.19	Transducer Energy Ratios as a Function of Material Properties and for the Free Terfenol-D Actuator	109
3.20	Actuator Non-linear Output Acceleration With a 20 Hz Driving Voltage	110
3.21	Actuator Non-linear Coil Current With a 20 Hz Driving Voltage	111
3.22	Actuator Non-linear Output Acceleration With a 600 Hz Driving Voltage	111
3.23	Actuator Non-linear Coil Current With a 600 Hz Driving Voltage	112
3.24	Actuator Non-linear Output Acceleration With a 3000 Hz Driving Voltage	112
3.25	Actuator Non-linear Output Acceleration With a 3300 Hz Driving Voltage	113
3.26	Actuator Non-linear Output Acceleration With a 3450 Hz Driving Voltage	113
3.27	Actuator Non-linear Output Acceleration With a 3600 Hz Driving Voltage	114
3.28	Correlated Free-stroke to Voltage Transfer Function for the Terfenol-D Actuator	117
4.1	The Terfenol-D Actuator Connected With a Spring-Mass Damper (SMD) System	119
4.2	The Actuator and SMD Impedance Magnitudes Showing the Location of Impedance Match and System Resonance	120
4.3	The Displacement of the Mass	121

4.4	The Interaction Force Between the Actuator and SMD System	122
4.5	Mass Displacement as a Function of Terfenol-D Rod Length and Cross-section	124
4.6	Interaction Force as a Function of Terfenol-D Rod Length and Cross-section	124
4.7	Mass Displacement as a Function of Fixture Spring Mass and Stiffness	126
4.8	Interaction Force as a Function of Fixture Spring Mass and Stiffness	127
4.9	Example of Decreased Mass Displacement With Increased Terfenol-D Rod Length at 1200 Hz	128
4.10	Example of Decreased Actuator/SMD Interaction Force With Increased Terfenol-D Rod Cross-section at 600 Hz	128
4.11	Energy Ratios For the Terfenol-D Actuator/SMD Combination and For the Free Actuator Showing Maximum Transducer Efficiencies	129
5.1	The Region of Operation for a Terfenol-D Actuator Between Two Curves Representing Minimum and Maximum Stress Levels	138
A.1	Actuator Non-linear Output Acceleration With a 30 Hz Driving Voltage (Time Domain)	144
A.2	Actuator Non-linear Output Acceleration With a 30 Hz Driving Voltage (Frequency Spectra)	144
A.3	Actuator Non-linear Coil Current With a 30 Hz Driving Voltage (Time Domain)	145
A.4	Actuator Non-linear Coil Current With a 30 Hz	145

	Driving Voltage (Frequency Spectra)	
A.5	Actuator Non-linear Output Acceleration With a 50 Hz	146
	Driving Voltage (Time Domain)	
A.6	Actuator Non-linear Output Acceleration With a 50 Hz	146
	Driving Voltage (Frequency Spectra)	
A.7	Actuator Non-linear Coil Current With a 50 Hz	147
	Driving Voltage (Time Domain)	
A.8	Actuator Non-linear Coil Current With a 50 Hz	147
	Driving Voltage (Frequency Spectra)	
A.9	Actuator Non-linear Output Acceleration With a 70 Hz	148
	Driving Voltage (Time Domain)	
A.10	Actuator Non-linear Output Acceleration With a 70 Hz	148
	Driving Voltage (Frequency Spectra)	
A.11	Actuator Non-linear Coil Current With a 70 Hz	149
	Driving Voltage (Time Domain)	
A.12	Actuator Non-linear Coil Current With a 70 Hz	149
	Driving Voltage (Frequency Spectra)	
A.13	Actuator Non-linear Output Acceleration With a 100 Hz	150
	Driving Voltage (Time Domain)	
A.14	Actuator Non-linear Output Acceleration With a 100 Hz	150
	Driving Voltage (Frequency Spectra)	
A.15	Actuator Non-linear Coil Current With a 100 Hz	151
	Driving Voltage (Time Domain)	
A.16	Actuator Non-linear Coil Current With a 100 Hz	151
	Driving Voltage (Frequency Spectra)	
A.17	Actuator Non-linear Output Acceleration With a 130 Hz	152

	Driving Voltage (Time Domain)	
A.18	Actuator Non-linear Output Acceleration With a 130 Hz	152
	Driving Voltage (Frequency Spectra)	
A.19	Actuator Non-linear Coil Current With a 130 Hz	153
	Driving Voltage (Time Domain)	
A.20	Actuator Non-linear Coil Current With a 130 Hz	153
	Driving Voltage (Frequency Spectra)	

## List of Tables:

Number	Title	Page
1.1	Representative Material Properties of Terfenol-D	13
2.1	Actuator System Parameters	77
2.2	Actuator Casing Properties	79
2.3	Actuator Output Rod Properties	80
3.1	Actuator Parameters Used for Theoretical to Experimental Correlation	96
3.2	Actuator Parameters Used for Theoretical to Experimental Correlation	97

## List of Symbols

### Terfenol-D Rod

$S$	strain
$T$	stress
$B$	flux density
$\bar{s}^H$	compliance (constant magnetic field)
$\bar{Y}^H$	elastic modulus (constant magnetic field)
$\rho$	density
$\mu^T$	permeability (constant mechanical stress)
$d$	"d" constant relating applied magnetic field to induced strain
$v_T$	rod displacement
$\kappa_T$	wave number
$C^H$	speed of sound (constant magnetic field)
$\eta$	mechanical loss factor
$A_T$	cross-sectional area
$l_T$	rod length
$K_T$	rod static stiffness
$\dot{x}_1$	output velocity
$F_1$	output force

### Mechanical Impedances

$Z_T$	Terfenol-D rod
$Z_F$	actuator fixture
$Z_R$	output rod

$Z_{RM}$	output rod as a mass
$Z_C$	series combination of the rod and external structure
$Z_H$	total impedance seen by the Terfenol-D rod
$Z_S$	external structure
$Z_{MEQ}$	total equivalent mass impedance (free actuator)
$Z_{KEQ}$	total equivalent stiffness impedance

### Electrical/Magnetic

$Z_E$	actuator electrical impedance
$Y_E$	actuator electrical admittance
$Z_{EF}$	electrical impedance (free actuator)
$Z_{EB}$	electrical impedance (blocked actuator)
$Z_{INDUCTOR}$	electrical impedance of the actuator coil as an inductor
$V_{tot}$	total voltage drop across the actuator coil
$I$	current in the coil
$L$	inductance of the coil
$\eta_e$	inductive loss factor of the coil
$N$	number of coil turns
$n$	turns per unit length ratio for the coil
$\Phi$	total magnetic flux in the Terfenol-D rod and coil

### Output Rod

$S_R$	strain
$F_R$	force
$T_R$	stress
$K_R$	stiffness
$A_R$	cross-sectional area
$l_R$	length
$\bar{Y}_R$	Youngs modulus
$\rho_R$	density
$m_{rod}$	mass
$v_R$	displacement
$\kappa_R$	wave number
$Z_O$	characteristic impedance
$v_{R_o}$	amplitude of the progressive wave solution
$R$	amplitude of a reflected wave
$\phi_R$	phase difference between a reflected and incident wave

### Transduction

$\phi_M$	transduction coefficient from the canonical representation
$\phi$	transduction coefficient for the mechanical dual form
$u$	actuator output velocity
$Z_{MO}$	open circuit mechanical impedance
$F_A$	force applied to the Terfenol-D rod
$F$	actuator output force
$V$	applied voltage



$k^2$  transducer energy ratio

Actuator/General

$\dot{x}_4$	actuator output velocity
$F_4$	actuator output force
$\omega$	driving frequency
$k_s$	fixture spring stiffness
$m_s$	fixture spring mass
$k_C$	fixture casing stiffness
$k_{eq}$	total equivalent fixture stiffness
$m_{eq}$	equivalent mass (free actuator)
$P_D$	dissipative power consumption
$P_R$	reactive power
$H$	applied magnetic field
$H_0$	magnetic bias field
$A, B$	constants used for solving wave equations
$\sigma_p$	mechanical prestress
$\mu_0$	baseline free permeability of the actuator coil

# Chapter 1

## Introduction

The use of induced strain materials as dynamic force generators and sensors has grown significantly with research efforts in the development of active mechanical systems. Magnetostrictive materials that strain in the presence of an applied magnetic field show great promise in industry applications because of improved stroke and force capabilities in comparison to piezoelectric ceramics. However, obtaining these behavior characteristics from magnetostrictive materials is more complex than with the piezoelectric counterparts.

The typical magnetostrictive actuator consists of a rod of magnetostrictive material surrounded by a wire coil or solenoid that applies a magnetic field to the material when a current is passed through the windings. Magnetic biasing is performed either with permanent magnets or a dc coil current. Also included inside the actuator is a prestress fixture usually consisting of a spring or other mechanism and an output shaft. The entire assembly is surrounded by a casing which serves as a portion of the prestress fixture, provides magnetic shielding, and completes the magnetic loop.

At present, these actuators are being manufactured and used in various applications without a comprehensive model of the actuator system dynamics and the involved

electro-magneto-mechanical interaction. This thesis will attempt to determine the transduction or input/output characteristics of magnetostrictive actuators through the development of a dynamic model that will include all mechanical and electrical aspects. This transduction model, once verified, will serve as a future tool for improvement of actuator designs and will provide appropriate specifications for usage as would be available with any commercially obtained magnetic shaker or other transducer device. The utility of the Terfenol-D actuator in control applications is also greatly improved with this transduction characterization. General industry applications of these magnetostrictive actuators will be limited until such design tools and specification information is available.

## **1.1 Terfenol-D As A Magnetostrictive Element**

The magnetostrictive effect, whereby a material expands or contracts in the presence of an external magnetic field, has been witnessed for some time in certain materials at cryogenic temperatures. The largest known magnetostrictive strain observed ( $\Delta l/l \approx 10^{-2}$ ) was at a temperature of 4 K (Clark, 1992). Until recently, giant magnetostrictive strains were limited to temperatures below 180 K. Increasing this temperature limitation to room temperature and higher was made possible with the alloying of rare-earth elements with iron to produce  $Tb_xDy_{1-x}Fe_{2-y}$  better known as Terfenol-D (Clark, 1992). The actuator used for this investigation is based on the induced-strain capabilities of Terfenol-D. The physics of this magnetically-induced material behavior and general characterization of Terfenol-D material properties are presented in the following subsections.

### **1.1.1 Physics of the Magnetostrictive Effect**

Many crystalline and amorphous materials exhibit the creation of domains on an atomic scale where existing magnetic dipoles will align themselves in a parallel configuration. These magnetic dipoles are usually the result of unpaired electrons in the atom valence shell as with ferromagnetic materials including iron, cobalt, and nickel. In general, these magnetic domains have a random orientation and there is no long-range magnetic moment present in the material (Smith, 1990). When an external magnetic field, designated as  $H$ , is applied to the material, several processes occur which produces the resulting material strain known as magnetostriction. At low values of  $H$ , magnetic domains that possess a favorable orientation with respect to the applied field grow at the expense of those domains which do not (Smith, 1990). This is known as the process of domain wall movement and is caused by the expansion and contraction of the bond lengths between atoms depending on the orientation of each domain with respect to the applied field  $H$ . The movement of domain walls requires less energy than the rotation of entire domains and thus stops at  $H$  levels far less than what is required to finish the magnetostriction process. Fig. 1.1 shows the regions for domain wall movement and

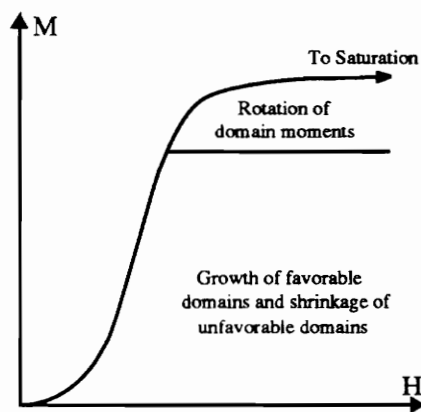


Figure 1.1: Increase in Material Magnetization With Respect to an Applied Magnetic Field (Smith, 1990)

domain rotation as the net magnetization  $M$  of the material increases to saturation with increasing applied field  $H$ . Typically the level of magnetization required to cause various degrees of domain alignment with an applied field differs with respect to different directions in the crystal lattice of the material. Some directions will be "magnetically easy" while others are considered "magnetically hard" (Clark, 1992). In other words, the domains in the easy directions in a crystal lattice will require less energy and lower applied fields to rotate while those in hard directions will require much more. This is magnetocrystalline anisotropy (Smith, 1990). A more complete description of the importance of the anisotropy is found in the next section detailing the material properties of Terfenol-D.

The magnetostriction process can be described by three stages (Clark, 1992):

1. Low magnetic field and little magnetization or magnetostriction has taken place.
2. Higher field levels and "jumping" between two or more magnetically easy directions each with varying amounts of magnetostriction.
3. Very high applied fields, near saturation, where the effective magnetic moment of the material rotates to the direction of the material rod axis assuming the applied field is also in that direction. Typically, this is how magnetostrictive actuators are designed.

The previously mentioned "jumping" process is best described as an abrupt conversion of stored magnetic energy into elastic energy (Clark, 1992) at a critical field level and is crucial to the construction of an effective magnetostrictive actuator. Jumping is made possible by applying external mechanical stress to the material. This serves to counteract internal stresses that develop during the process of domain movement and rotation. This

applied prestress must be greater than 5 MPa for most specimens and ensures that there exist magnetically easy directions that are nearly transverse or perpendicular to the axis of the specimen for zero applied field. The largest mechanical strains are available when the initial domain orientations are transverse (Fenn, Bushko and Gerver, 1993). Without the required prestress, the material will undergo magnetization by 180 degree domain wall movement and finally rotation of the magnetization moment (Clark, 1992). The latter process is the only one which will produce any magnetostriction. However, this induced strain is insignificant.

All aspects of the magnetostrictive effect are temperature dependent. Below the anisotropy compensation temperature of the material, the magnetically easy directions are typically those which do not provide any magnetostriction. Also, the available saturation magnetostriction decreases rapidly as temperature is increased above the anisotropy compensation temperature. For reference, the anisotropy compensation temperature occurs when the available magnetostriction to anisotropy ratio reaches a maximum.

### **1.1.2 Characterization of Terfenol-D Material Properties**

Development and preliminary characterization of the magnetostrictive material known as Terfenol-D was done at the Ames Laboratory at Iowa State University and at the Naval Ordnance Laboratory (now known as the Naval Surface Weapons Center). The name Terfenol-D is derived from the composition of the material. "Te" stands for terbium, "fe" for iron, and "D" for dysprosium. The "nol" designation was given because of the work done at the Naval Ordnance Laboratory (NOL). The chemical composition of the alloy is defined as  $Tb_x Dy_{1-x} Fe_{2-y}$ . Dr. A. Clark, one of the principle contributors to the development of Terfenol-D, describes the magnetostrictive effect in the material as being

highly complex (Clark, 1992). The formation of Terfenol-D takes place in the [112] crystallographic direction and growth occurs in twinned dendritic sheets. A model of the magnetostrictive effect in Terfenol-D was developed by Clark (1992) and accounts for unique effects caused by the complex structure of the material. In general, the behavior of the magnetostriction in Terfenol-D has been characterized as having a significant dependence on temperature, applied mechanical stress, and magnetic driving field. Also, the ratio of the available magnetostriction in the magnetically "easy" directions vs. the magnetically "hard" directions is very high (Clark, 1992).

The general behavior characteristics of Terfenol-D can be divided into three categories: magnetic, mechanical, and thermal. The magnetic behavior relates how induced-strain in the material is related to the applied driving field. The mechanical behavior shows the effect of driving field on certain mechanical properties. The thermal behavior shows the sensitivity of magnetostriction to temperature.

The relationship between the induced magnetic flux density in the material, designated as

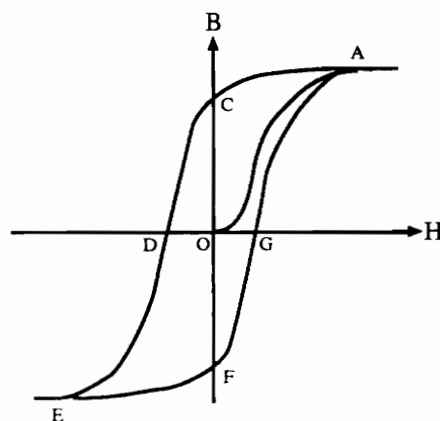


Figure 1.2: The Magnetic Flux Density Variation With Applied Magnetic Field For a Ferromagnetic Material (Smith, 1990)

B, that results from a driving magnetic field,  $H$ , is a hysteresis loop similar to that of any material that can be magnetized (Smith, 1990). Fig. 1.2 describes a cyclic magnetization and demagnetization of a material. Moving from no applied field to saturation follows the graph on path O-A. The magnetization, however, does not follow that path as the applied field is slowly decreased. Instead, the path A-C is traced and at levels of  $H = 0$ , a remaining flux density, known as the remnant induction, remains in the material. Application of a negative applied field is then required to return the material to a state of zero flux density which occurs at point D. Increasing this negative field until saturation at point E, removal of the negative field and application of a positive field then causes the material to trace the path E-F-G-A. This completes the loop on which the material properties will vary when further magnetization and demagnetization takes place. The width of this described hysteresis loop is a measure of how magnetically "soft" or "hard" a material is. This "soft" designation refers to the ability of a material to be both easily magnetized and demagnetized and can be applied to crystallographic directions as mentioned previously. The hysteresis loop can best be thought of as a measure of the amount of energy consumed by the material while the cyclic magnetization process is underway. "Soft" materials are easily magnetized and require less energy to complete a cycle than a "hard" material would. Therefore, this loop is narrow for a "soft" material and is wide for a "hard" material. The energy loss represented by the hysteresis loop is typically caused by material impurities and imperfections or by the character of the material structure in the case of Terfenol-D. These factors interfere with the domain wall movement and domain rotation processes that occur as the applied magnetic field varies. The slope of this hysteresis loop is the magnetic permeability  $\mu$  of Terfenol-D and is seen to be dependent on the level of the driving field  $H$ .

The induced flux density in the Terfenol-D described above is related to the induced



material strain as is shown in Fig. 1.3. Notice that there exists no energy losses or hysteresis between the induced strain  $S$  and flux density  $B$ . However, the combined relationship between induced strain  $S$  and applied magnetic field  $H$  shows the effects of the magnetic hysteresis.

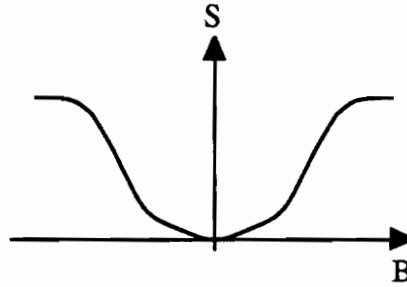


Figure 1.3: The Relationship Between Induced Strain and Induced Flux Density for Terfenol-D (Butler, 1988)

The  $S$  vs.  $H$  curves differ for varying applied mechanical pre-stress as is shown in Fig. 1.4. The slopes of these curves in the linear region are the representative "d" constants.

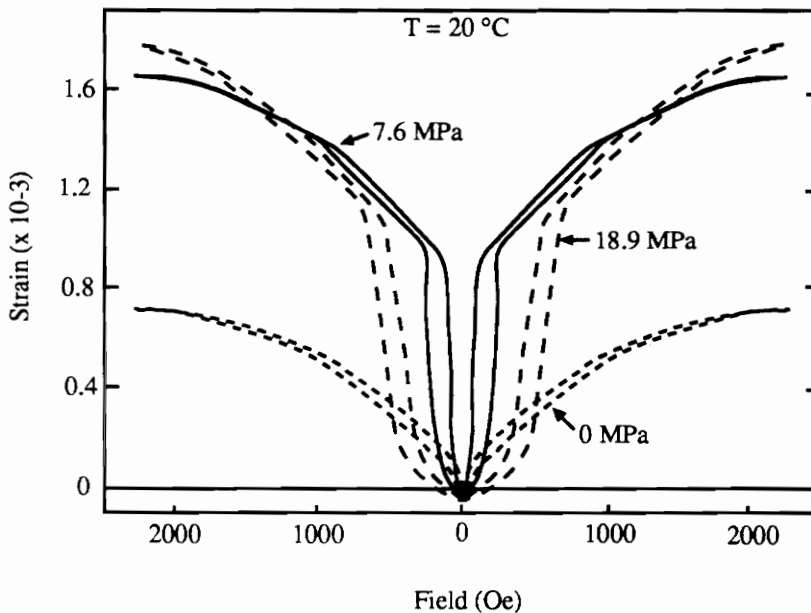


Figure 1.4: Induced Strain as a Function of Applied Magnetic Field and Mechanical Prestress (Clark, 1992)

As can be seen in Fig. 1.4,  $d$  is a function of the mechanical prestress. The  $d$  constant relates induced strain to applied magnetic field in the region where Terfenol-D is typically used. Further definition of this operation area is found later in this section.

Fig. 1.5 shows that Terfenol-D has a complex stress vs. strain relationship since the elastic modulus is a function of strain. Also, the material modulus is dependent on the level of the applied driving field  $H$ .

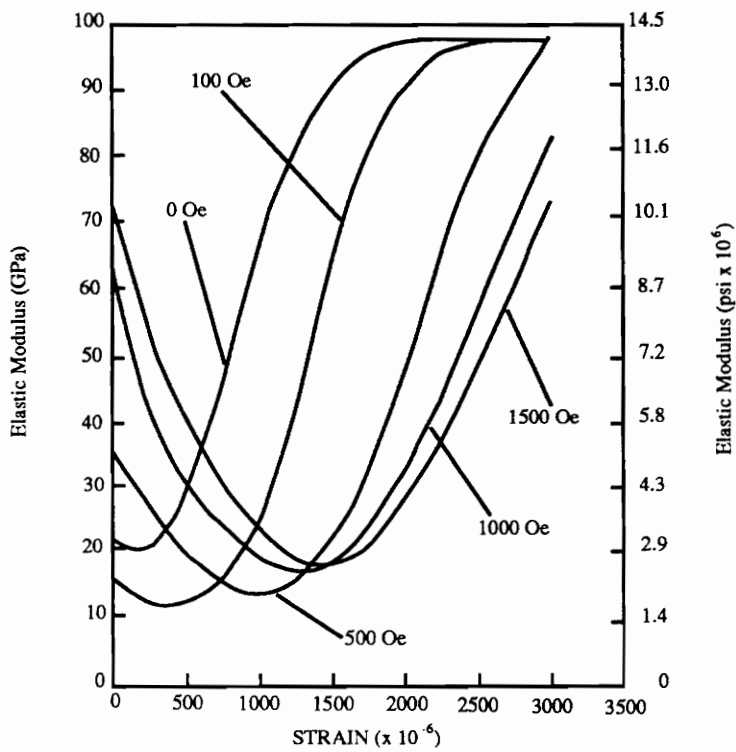


Figure 1.5: The Relationship Between Terfenol-D Elastic Modulus and Material Strain for Varying Driving Fields (Butler, 1988)

As was previously mentioned in the general description of the magnetostrictive effect, the strain available at magnetic saturation decreases significantly with increasing

temperatures. This effect can be seen in Fig. 1.6 for various driving fields.

The chemical composition of Terfenol-D ( $Tb_x Dy_{1-x} Fe_{2-y}$ ) can be tailored for requirements of differing applications by varying the composition percentages. Terfenol without the "D" designation refers to the compound  $TbFe_2$ . Substitution of dysprosium (Dy) for terbium was done to improve the magnetic and mechanical properties of the material. Specifically, dysprosium reduces the cubic magnetic anisotropy ( $k_1$ ) of the material. This acts to dramatically increase the ratio of the available magnetostriction to

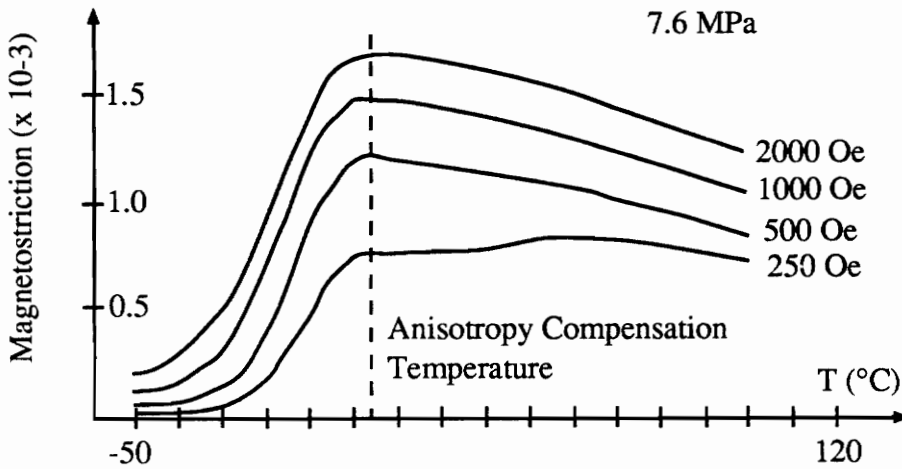


Figure 1.6: Decreasing Available Magnetostriction At Magnetic Saturation for High Temperatures With 7.6 MPa Prestress (Clark, 1992)

anisotropy thus providing larger and more uniform magnetostriction and less hysteresis (Clark, 1992). Experimentation regarding the effect of composition percentages of terbium and dysprosium on available magnetostriction were performed by Clark (1992) and is shown in Fig. 1.7.

Another important material behavior that can be altered through composition relates the temperature at which the important <111> directions in the crystal lattice are populated as magnetically "easy" directions for a given level of mechanical prestress. The population of the <111> or transverse directions affect the "jumping" effect and the magnitude of magnetostriction that will occur. Typically, for a terbium percent composition  $x < 0.3$ , the temperature required for population will decrease and vice-versa for  $x > 0.3$ . As a reference, for a typical sample of Terfenol-D where  $x = 0.3$  and  $y = 0.1$ , the required population temperature is near  $-10\text{ }^{\circ}\text{C}$  (Clark, 1992). Considering a wide range of appropriate performance requirements, the composition ratios for Terfenol-D are typically in the range of  $0.27 < x < 0.3$  and  $0.0 < y < 0.5$ .

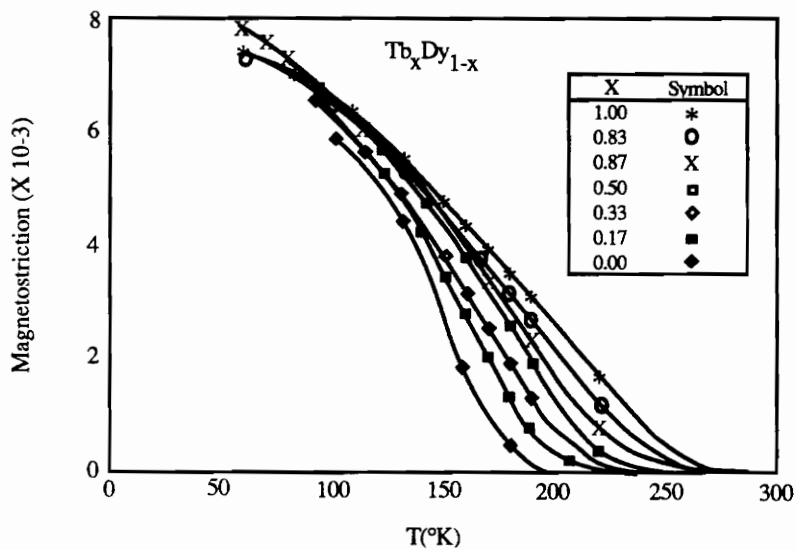


Figure 1.7: The Effects of Stoichiometry Variation on Available Magnetostriction for a Range of Temperatures (Clark, 1992)

Because of the complex relationships and non-linearities present in the behavior of Terfenol-D, the typical actuator using magnetostriction will operate in the linear range of

a strain  $S$  vs. applied field  $H$  curve for a certain level of prestress. This is accomplished by imposing an induced magnetic bias usually in the form of permanent magnets. Sometimes the bias point is established by adding a dc current to the sinusoidal driving current. However, in most cases this causes undesirable heating of the entire actuator because of the resistivity of the copper windings of the coil. With a bias point, the Terfenol-D will exhibit bi-directional strain around that point and will avoid the regions of non-linearity in the  $S$  vs.  $H$  relationship. A typical  $S$  vs.  $H$  curve with an operating bias point at  $(S_o, H_o)$  is shown in Fig. 1.8.

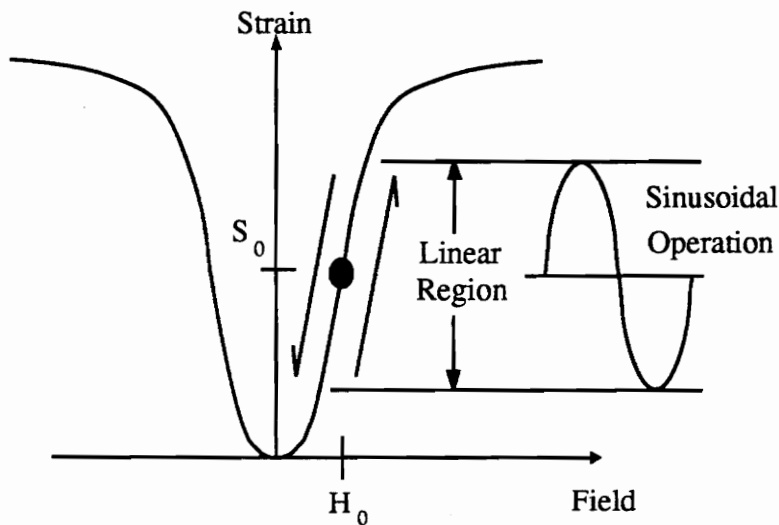


Figure 1.8: Illustration of a Bias Point For Linear, Bi-directional Operation of a Terfenol-D Based Actuator

When the Terfenol-D actuator operates in this linear region, the mechanical and electrical behavior of the material can be described by the well established constitutive relationships (Butler, 1988):

$$S = s^H T + dH$$

$$B = dT + \mu^T H$$

Below is a full listing of all relevant Terfenol-D parameters.

$S$	strain
$s^H$	material compliance (constant applied field)
$T$	stress
$d$	the "d" constant or slope of the S vs. H curve
$H$	applied magnetic field
$B$	induced flux density
$\mu^T$	material magnetic permeability (constant applied mechanical stress)

A listing of representative material properties, given by Butler (1988), are shown in Table

Property	Symbol	Value	Units
Density	$\rho$	9.25 e+3	$kg/m^3$
Youngs Modulus	$Y^H$	2.5-3.5 e+10	$N/m^2$
	$Y^B$	5.0-7.0 e+10	$N/m^2$
Speed of Sound	$C^H$	1.72 e+3	$m/sec$
	$C^B$	2.45 e+3	$m/sec$
Permeability	$\mu^H$	1.16 e-5	$Tm/A$
	$\mu^B$	5.65 e-6	$Tm/A$
d constant	d	1.50 e-8	$m/A$
g constant	g	1.28 e-3	$1/T$
Resistivity	$\rho_e$	60 e-8	$\Omega m$

Table 1.1: Representative Material Properties of Terfenol-D (Butler, 1988)

1.1. Note that values with the H subscript designate an open circuit condition and the B subscript designates a short circuit condition for the actuator coil leads. The properties shown above are representative figures for Terfenol-D materials. However, some of these properties change with chemical composition while others are functions of applied field, prestress and others as described in this section. The "g" constant above relates the level of current induced in the actuator coil when a stress is applied to the ends of the material. This is known as the Villari or converse effect (Pratt and Flatau, 1993). Knowledge of this converse effect has prompted research into development of a collocated actuator/sensor concept in which an actuator can actuate and sense concurrently. Further discussion of this capability is found in the Transducer Literature Review Section and an example of research effort is presented in the Actuator Modeling Literature Review Section.

Currently there exist two methods for production of Terfenol-D. The Free-Stand Zone Melt (FSZM) method provides the largest ultimate strain values for the material. The Modified Bridgman (MB) method allows for production of larger diameter rods (Butler, 1988). Manufacturers claim that produced Terfenol-D rods possess uniform crystal orientation which was a problem with early production attempts. This question of production reproducibility was tested with varying success (Goodfriend, Shoop, and McMasters, 1992).

## **1.2 General Applications of Terfenol-D**

The high force and high stroke capabilities of Terfenol-D have prompted significant investigation into applications for this material. Possible industry applications include force actuators for high precision machining processes and positioning of high accuracy

instrumentation (Hiller, Bryant, and Umegaki, 1989). Terfenol-D has also been considered for use in automobile lab setups and for fuel injector units (Dyberg, 1986). Because Terfenol-D possesses not only high force capabilities, but also excellent bandwidth and rise-time characteristics, there has been a large body of research performed on using Terfenol-D actuators for vibration isolation and for active control applications (Hiller, Bryant, and Umegaki, 1989; Haynes, Geng, and Teter, 1993). Other possible applications include development of low frequency sonar transducers (Oswin, Edenborough, and Pitman, 1988) and collocated actuator/sensor systems (Pratt and Flatau, 1993).

### **1.3 Terfenol-D Actuators**

Actuators based on the induced-strain capabilities of Terfenol-D possess most of the same features. However, some actuator designs have inherent problems with contact stiffnesses and improper alignment between elements and with proper completion of the magnetic loop. These factors can create significant difficulties in verification of any model of actuator performance.

#### **1.3.1 Actuator Layout and Parameters**

A diagram of the actuator used in this thesis is shown in Fig. 1.9. This actuator was supplied by Intelligent Automation, Inc. located in Rockville, Maryland. The Terfenol-D material, in rod form, is surrounded by a wire coil. Passing an alternating current through the coil creates an alternating magnetic field  $H$  and makes the rod vibrate. Because the Terfenol-D strain behavior is a rectified form of the sinusoidal electrical input, a magnetic dc offset is imposed to allow for bi-directional rod vibration and to



insure that the actuator operates in the linear portion of the material strain vs. applied field relationship. The actuator also possesses a pre-stress mechanism in the form of a spring. An exterior casing also functions as a portion of the prestress mechanism and provides shielding. An output rod transfers the vibrations of the Terfenol-D outside of the actuator casing.

### 1.3.2 Actuator Modeling Literature Review

Most of the present modeling of Terfenol-D actuators can be classified into two categories: static modeling and block diagram realizations. An example of a static approach used in a vibration control experiment is presented by Hiller, Bryant, and

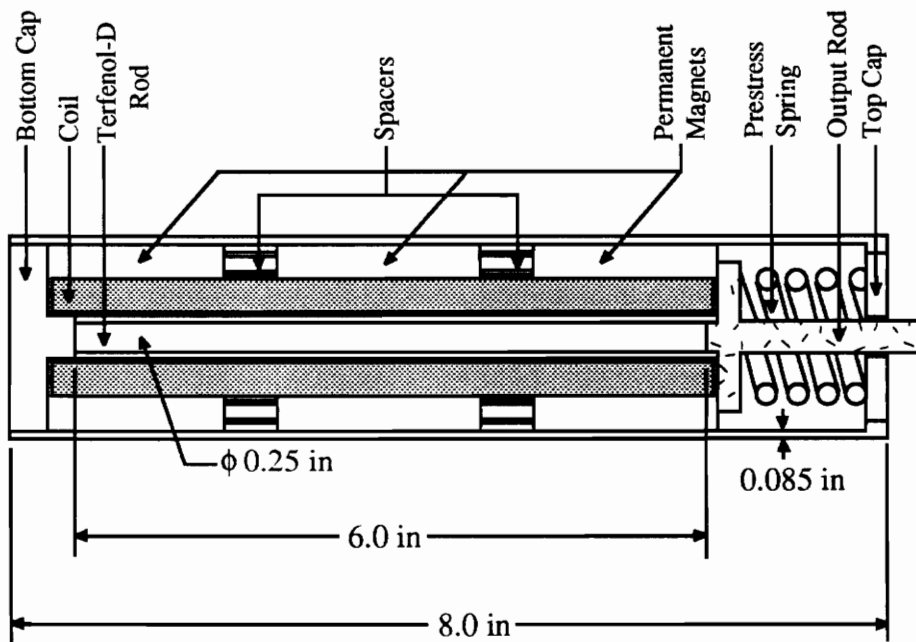


Figure 1.9: Exploded View of the Modeled Terfenol-D Actuator  
(Haynes, Geng, and Teter, 1993)

Umegaki (1989). A linear and frequency independent relationship between the derived system error signal, which was used as the voltage applied to the leads of the actuator coil, and the corresponding actuator stroke output was assumed. This thesis will attempt to show that the assumption of uniform strain in the Terfenol-D rod used in this investigation was incorrect. The feedback gains of the control system had to be determined experimentally because of the inadequacies of the actuator and system models. The experiment proved successful in the attempt to provide vibration isolation. However, the maximum driving current of 20 amps and use of an electrical dc bias are suspect. Another example of a statics-based modeling approach (Haynes, Geng, and Teter, 1993) represents the actuator output force and stroke as linear, frequency-independent functions of input current. The actuator modeled with this approach was used in a vibration isolation experiment that utilized an adaptive control system. With this setup the control system was able to adjust for inadequacies in the actuator model. Similar research involved vibration attenuation and disturbance rejection of a table system using Terfenol-D actuators (Bryant, et al., 1992a). Two separate approaches were utilized and compared for effectiveness. The first was a PID controller and the second was an ANN (adaptive neural network) controller. The ANN controller significantly outperformed the PID in this investigation because of the ability of the network to adjust for dynamic and electrical inadequacies and non-linearities not incorporated in the PID model.

The controls derived, block diagram realizations of Terfenol-D actuators produce transfer function behaviors that follow the trends of the actual actuators (Bryant and Wang, 1992b) but cannot quantify the dynamics and electro-magneto-mechanical interaction present in these devices. This can be seen best in the comparisons of the frequency response functions of the actuators modeled by Reed (1988). Much of the broad band

behavior of the model compares well with that of the actuator. However, the models used are unable to identify the effects of the electro-magneto-mechanical interaction as is evident by the resonant peaks present in only the experimental strain/current and current/force transfer functions.

Another investigated aspect of Terfenol-D actuator behavior involves the effects of thermal-induced strains on performance (Anjanappa and Bi, 1993). The actuator system is modeled as a SMD (spring-mass-damper) system with thermal effects included as additional terms in the Terfenol-D constitutive equations. This work focuses on the design aspects of producing a small, high-precision actuator that would be embedded into a host structure for vibration control or shape modification. In such a configuration the effects of poor heat transmission would cause non-negligible strain variation (Anjanappa and Bi, 1993).

Other actuator modeling work includes a phenomenological approach to representing the non-linear behavior and harmonics exhibited by Terfenol-D actuators in dynamic applications (Hall and Flatau, 1993). There have also been efforts in development of a collocated actuator/sensor system using a Terfenol-D actuator and a bridge circuit for self-sensing (Pratt and Flatau, 1993). This modeling work investigated the electro-mechanical transduction aspects of the actuator mostly from the electrical side. A similar use of this transduction representation as a design and analysis tool is presented in this thesis.

### **1.3.3 Experimental Usage of the Terfenol-D Actuator Literature Review**

The actuator modeling literature review gave numerous examples of Terfenol-D actuators

being used in vibration attenuation and isolation experiments (Hiller, Bryant, and Umegaki, 1989; Haynes, Geng, and Teter, 1993; Bryant et al., 1992). Terfenol-D actuators have also been successfully used for vibration control without any analytical model or adaptive controller (Flatau, Hall, and Schlesselman, 1992). Two commercially available Terfenol-D actuators (B&K 4809 and CM50) were used to attenuate the vibration of an aluminum beam by using inverted and amplified acceleration data as electrical input.

## 1.4 Transducer Literature Review

A transducer is defined as a device that provides an electric signal in response to a change in a measured physical quantity or condition known as the measurand (Norton, 1990). All transducers are classified as sensors because of this defined ability to convert a physical quantity into an electrical one. However, not all sensors are transducers (Norton, 1989). While transducers simply provide a usable electric signal in response to a specific measurand, other sensory devices, known as analyzers, perform analysis on collected data before presentation to the user. Such analyzers are commonly used in the analysis of chemicals and chemical processes. Depending on the specific application, transducers are often referred to by other names including sensors, detectors, and transmitters.

All transducers can be described by the following (Norton, 1989):

1. **Measurand**: The specific physical quantity that the device will measure.
2. **Transduction Principle**: The means by which the device converts the measurand into a usable electrical signal.
3. **Significant Feature**: A special feature which distinguishes a transducer from

other devices that are intended to measure the same measurand.

4. **Range:** The defined input and output capabilities of the device.

Transducers are generally divided into two major categories: non-self-generating and self-generating. The difference between these two groups involves the transduction principle used. Most transducers are non-self-generating or passive (Norton, 1989) and require an external source of electrical excitation to provide an electrical output in response to the measurand. Some passive transducers operate using capacitive transduction where a change in the measurand causes a change in the capacitance of the device. Thus, the change in electrical output is directly related to the change in the measurand. Other passive transducers operate in a similar manner, but relate changes in resistance and inductance to changes in the measurand.

Self-generating transducers require no external electric excitation to perform the sensing task. Common examples include piezoelectrics, photovoltaics, electromagnetics, and thermoelectrics (Norton, 1990). Piezoelectric devices operate using the commonly known piezoelectric effect wherein a force applied to the material produces an electrostatic charge and vice-versa. Piezoelectrics are commonly used to measure acceleration and strain. Photovoltaics use the voltage produced between two joined, dissimilar materials (usually a conductive metal and semiconductor or between two different types of semiconductors) when the combination is illuminated. These transducers are commonly used as light sensors. Electromagnetics use a measurand-induced flux change to perform transduction. Thermoelectrics, also known as thermocouples, use a temperature-induced change in the generated voltage between two joined, dissimilar conductive metals to produce an electric signal.

Transduction converse to that described above takes place with materials like piezoelectrics and with devices such as loudspeakers (Kinsler, et al., 1982). In this situation a mechanical output is produced in response to an applied electrical signal. In the case of piezoelectric ceramics, the mechanical output is in the form of induced strain. For a loudspeaker device the mechanical output is in the form of sound.

The coupling coefficient  $k$  of a transducer device defines the magnitude of the coupling between an electrical and mechanical system parameter. The coupling coefficient is generally derived from the constitutive equations that describe system behavior when two system parameters are linearly coupled. These constitutive equations are determined by differentiation of the free energy of the system as described by Ikeda (1990) and are shown as:

$$H = a_{11}\eta + a_{12}x$$

$$X = a_{12}\eta + a_{22}x$$

The cross term  $a_{12}$  defines the linear coupling of the system. The coupling coefficient  $k$  is defined as (Ikeda, 1990):

$$k^2 = \frac{a_{12}^2}{a_{11}a_{22}}$$

If  $a_{12} = 0$  then no coupling exists between the system parameters  $\eta$  and  $x$ .

In the case of Terfenol-D or any other magnetostrictive material, the coefficients of the constitutive equation and coupling coefficient are material properties as seen from the

constitutive equations for Terfenol-D previously shown as:

$$S = s^H T + dH$$
$$B = dT + \mu^T H$$

The coupling coefficient for Terfenol-D is then:

$$k^2 = \frac{d^2}{s^H \mu^T}$$

Generally, the ability of a transducer to provide a usable electric signal in response to an applied physical quantity is defined as electro-mechanical coupling. The coupling coefficient, designated as  $k$ , is defined as a measure of the magnitude of this electro-mechanical coupling and not a measure of the conversion efficiency of the transducer. However, the energy ratio, defined as  $k^2$ , is a measure of transducer efficiency and is dependent on operating and boundary conditions. The energy ratio  $k^2$  has been defined in numerous ways in the past (Ikeda, 1990). Generally, the energy ratio describes, in some manner, the ratio of energy stored in the transducer in relation to the energy input.

A representative value of a Terfenol-D coupling coefficient is in the range of 0.7-0.75 (Butler, 1988). However, because of the material property dependence on stress levels, driving field magnitude, and temperature, the coupling coefficient can vary out of this range significantly. In comparison, lead zirconate titanate (PZT) has a coupling coefficient in the range of 0.35-0.7.

An alternate description of the transduction energy conversion process has the form of a

two-port network (Kinsler et al., 1982) shown in Fig. 1.10. This network shows the electrical system properties at one port in relation to the mechanical properties at the other. The canonical transduction (input/output) equations defined by the two-port representation assume that a linear relationship exists between the coupled electrical and mechanical system parameters. The positioning of force  $F$  and velocity  $u$  depend on the type of transducer.

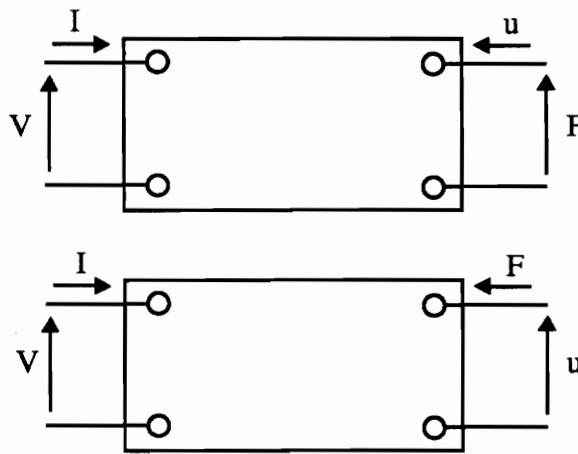


Figure 1.10: Two-port Network Descriptions of Transducer Operation  
(Kinsler et al., 1982)

- where:  $V$  is the applied voltage  
 $I$  is the current  
 $u$  is the velocity  
 $F$  is the force

The electrical and mechanical impedances that are defined by the network in Fig. 1.10 are presented as:



1. Blocked electrical impedance:  $Z_{EB} = (V/I)|_{u=0}$
2. Free electrical impedance:  $Z_{EF} = (V/I)|_{F=0}$
3. Open-circuit mechanical impedance:  $Z_{mo} = (F/u)|_{I=0}$
4. Short-circuit mechanical impedance:  $Z_{ms} = (F/u)|_{V=0}$

The canonical transduction equations developed from the network shown in Fig. 1.10 are given as:

$$V = Z_{EB}I + T_{em}u$$

$$F = T_{me}I + Z_{mo}u$$

where:  $T_{em}$ ,  $T_{me}$  are the transduction coefficients

The coupling coefficient  $k$  taken from the canonical equations is:

$$k^2 = \frac{T_{em}T_{me}}{Z_{EB}Z_{mo}}$$

There exist two separate types of transducers: reciprocal and antireciprocal. Reciprocal devices exhibit transduction behavior such that  $T_{em} = T_{me}$  while antireciprocal devices show  $T_{em} = -T_{me}$ .

The coupling coefficient developed from the two-port network is helpful in analyzing a device such as a Terfenol-D actuator because the expression provides more information concerning the frequency dependence of the device transduction and efficiency while the earlier coupling coefficient form is dependent on material properties only.

A rearranged form of the canonical transduction equations is known as the mechanical dual form (Kinsler et al., 1982) and is shown as:

$$V = Z_{EF} I + \phi F$$

$$u = \phi I + \frac{F}{Z_{mo}}$$

where:  $\phi = \phi_M / Z_{mo}$

$$\phi_M = T_{em} = T_{me}$$

Another important transducer aspect that is receiving research attention is the development of a collocated actuator/sensor. Such a system could perform actuation and "self-sensing" concurrently and would reduce the required instrumentation in configurations such as automatic control systems. A collocated actuator/sensor is made possible by use of the mechanical dual transduction equations shown above. There are four variables (two intensive and two extensive) in these expressions. Knowledge of any two variables allows for solution of the others. The voltage applied to a transducer and the resulting current are quantities that can be easily measured. Using those two measured electrical quantities, the output force and velocity (and position) of a transducer like the Terfenol-D actuator can be found concurrently.

## 1.5 Scope and Objectives

The focus of this thesis is to develop a model of the transduction behavior of a magnetostrictive actuator in order to improve the understanding of the dynamic and electro-magneto-mechanically coupled behavior of the device. The use of an impedance

modeling approach allows for improved accuracy in the representation of the dynamic behavior of the entire actuator system in an attempt to improve upon the modeling efforts of the past.

The objective of this thesis is to develop and experimentally verify a transduction expression for general Terfenol-D actuators and analyze the performance and efficiency of this transducer with respect to its design features. In conjunction with such an analysis, the development of a general design strategies and operating specifications are appropriate further steps toward complete characterization of the device.

## **1.6 Thesis Outline**

The first chapter of this thesis describes the research interests associated with Terfenol-D, the physics involved in the magnetically-induced material strain behavior, and general material characterization. Present and future applications of the material are discussed with a concentration on development and modeling of magnetostrictive transducers. Chapter 2 details the analytical development of a transduction representation for the magnetostrictive actuator using an impedance modeling approach. The electro-magneto-mechanical aspects of the actuator behavior are explored and the efficiencies of the magnetostrictive transducer are analyzed. The mechanical and electrical properties of the actuator are also determined. Chapter 3 details the experimental setup used for obtaining the transfer function and impedance data of the actuator and the separate coil. An analysis of this data and theoretical correlation is also discussed with implementation of a system identification technique for model improvement. A discussion of internal actuator force transfer, power consumption, and transducer efficiency is presented. Experimental time-domain and non-linear actuator behavior is also shown. Chapter 4 provides a

description of a general actuator design process based on the dynamic interaction between the actuator and a driven external structure. Chapter 5 provides a summary of the thesis and details the contributions made in this work. A future work section provides suggestions for further improvement of the model. Appendices show examples of the observed experimental actuator non-linearities in time and frequency formats and provides the computer codes used for theoretical simulations.

# Chapter 2

## Actuator Modeling Investigation

The modeling approach utilized in this thesis quantifies both the electrical frequency characteristics and the mechanical dynamics of the actuator system. These behaviors are then combined through the constitutive relationships for Terfenol-D and used to produce the transduction representation.

### 2.1 Introduction

This electro-magneto-mechanical modeling approach utilizes equivalent electrical impedances for structural elements in order to construct an accurate model of the actuator dynamics.

In an electrical sense, the general impedance definition is given as:

$$V = ZI$$

where:  $V$  is the voltage drop across the element  
 $Z$  is the electrical impedance of the element  
 $I$  is the current flowing through the element

The general impedance relationship for mechanical systems (Harris, 1988) is given as:

$$F = Z\dot{x} \quad (1)$$

where:  $F$  is an arbitrarily applied sinusoidal force  
 $Z$  is the impedance of the element  
 $\dot{x}$  is the resulting velocity

Figure 2.1 graphically illustrates the mechanical impedance concept. This impedance is often described as a dynamic or frequency dependent stiffness. The definition of mechanical mobility  $M$  is the inverse of impedance or:

$$M = \frac{\dot{x}}{F}$$

Modeling of mechanical systems is performed by completion of two tasks. The first involves breaking the system into a group of lumped masses, stiffness, and dampers. The second combines those lumped impedances in series and parallel combinations in order to

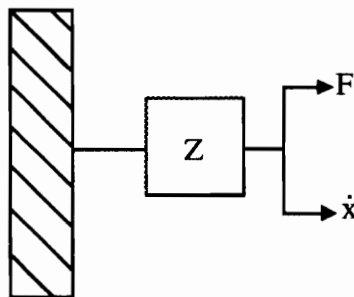


Figure 2.1: General Representation of Mechanical Impedance

reproduce the behavior of the entire system. Sometimes, however, certain components cannot be modeled with a lumped impedance and an expression for a continuous element must be used. Further discussion about the impedance of continuous elements is found later in this section and in the subsection detailing the mechanical modeling of the actuator.

## 2.2 Discussion of Lumped Impedances

The impedances of lumped masses, springs, and dampers is found by plugging into the general impedance expression Eq. (1) and solving for the impedance  $Z$  for each type of element. Heviside operators are also used for differentiation and integration.

Impedance of a mass:

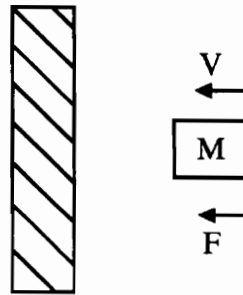


Figure 2.2: Representation of a Lumped Mass

The force required to accelerate a mass is known as:

$$F = ma = m\dot{V}$$

where:  $m$  is the mass  
 $a$  is the mass acceleration  
 $\dot{V}$  is the first derivative of the velocity (acceleration)  
 $V$  is the velocity ( $\dot{x}$ )

Plugging into Eq. (1) yields:

$$Z_{mass} = \frac{F}{V} = \frac{j\omega m V}{V} = j\omega m$$

Impedance of a spring:

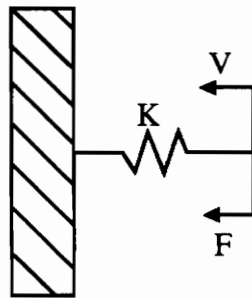


Figure 2.3: Representation of a Lumped Stiffness

The force required to compress a spring is known as:

$$F = kx = \frac{kV}{j\omega}$$

where:  $k$  is the spring stiffness  
 $x$  is the spring deflection



$V$  is the velocity ( $\dot{x}$ )

Plugging into Eq. (1) yields:

$$Z_{spring} = \frac{F}{V} = \frac{kV}{j\omega V} = \frac{k}{j\omega} = -\frac{k}{\omega} j$$

Impedance of a damper:

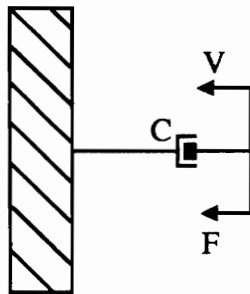


Figure 2.4: Representation of a Lumped Damper

The force required to compress a damper is known as:

$$F = cV$$

where:  $k$  is the spring stiffness  
 $c$  is the damping value  
 $V$  is the velocity ( $\dot{x}$ )

Plugging into Eq. (1) yields:

$$Z_{damper} = \frac{F}{V} = \frac{cV}{V} = c$$

Lumped impedance elements can be connected in two different ways: parallel and series. In the parallel configuration shown in Fig. 2.5 both impedance elements have the same displacement or velocity  $V$  but not the same share of the applied force  $F$ .

In the series configuration also shown in Fig. 2.5 the impedance elements have unequal displacements or velocities but equal forces.

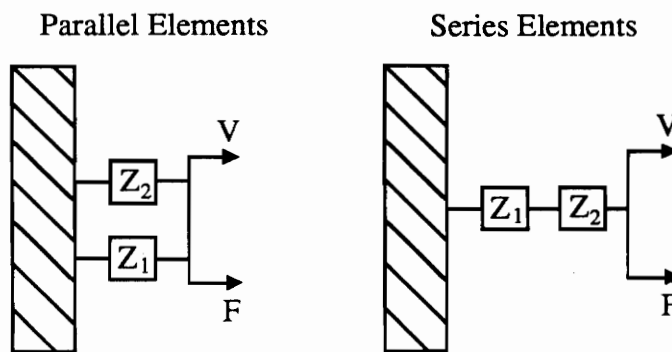


Figure 2.5: Parallel and Series Configurations for Lumped Impedance Elements

A complete mechanical impedance representation can be simplified to a simpler expression by using the rules governing impedance combination of lumped elements. Parallel lumped elements are combined by addition of the impedances. Series lumped elements are combined by addition of the mobilities. These combination rules are equivalent to that of electric capacitors or opposite to that of electric resistors with respect to the parallel and series rules.

The difficulty that arises with continuous elements is simply that the mechanical properties of mass, stiffness, and damping are continuous and in many cases lumped parameter values are not accurate for varying boundary conditions and geometries.

Further explanation of impedance modeling of lumped and continuous elements in mechanical systems is described by Snowdon (1968) and Harris (1988).

### 2.3 Actuator Subsystem Representation

In order to produce a dynamic model of the the actuator, the properties of the electrical and mechanical portions are first separated and investigated. Then the electro-magneto-mechanical interaction of the actuator device is developed through combining the

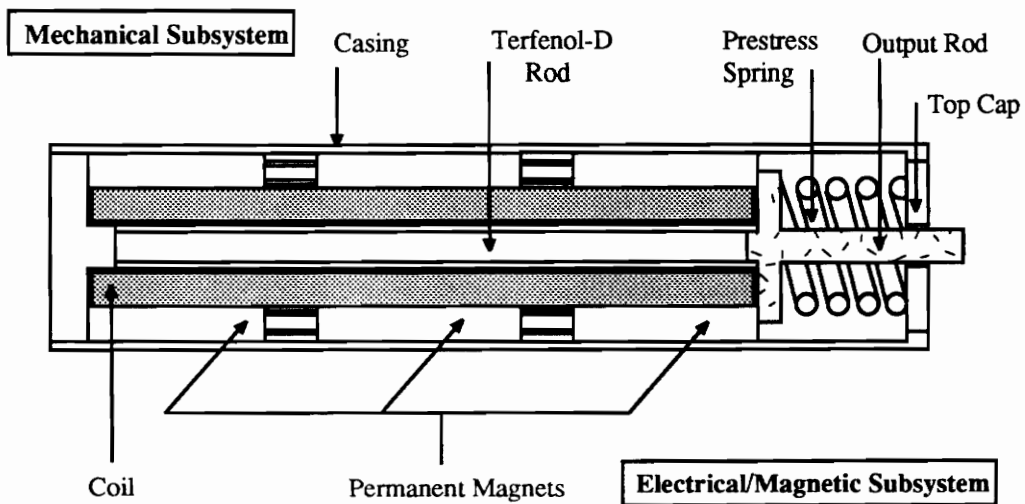


Figure 2.6: Terfenol-D Actuator Configuration Showing Mechanical and Electrical Subsystems

electrical and mechanical behaviors in the constitutive relationships for Terfenol-D. Figure 2.6 shows the complete actuator configuration and distinguishes between the mechanical and electrical subsystems.

## 2.4 Mechanical Aspects

The modeling approach involves developing impedance relationships for the magnetostrictive element and fixturing inside the actuator and to combine those expressions in such a way as to correctly simulate the behavior of the actuator. The developed mechanical impedance diagram including prestress fixture impedance  $Z_F$ , output shaft impedance  $Z_R$ , external impedance  $Z_S$ , output force  $\bar{F}_4$ , and velocity  $\bar{\dot{x}}_4$  is shown in Fig. 2.7.

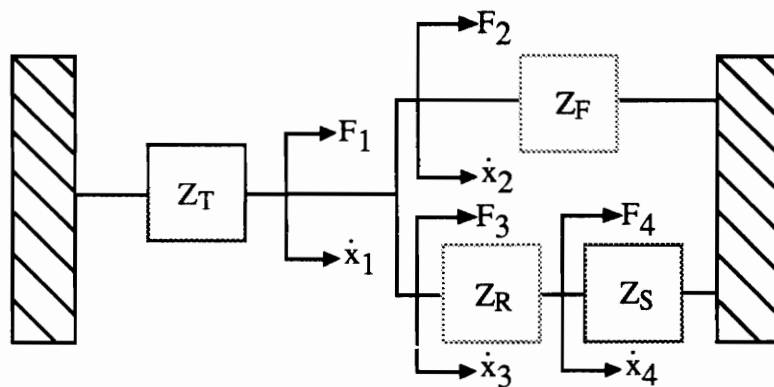


Figure 2.7: Complete Mechanical Impedance Diagram

Activation of the Terfenol-D rod and the actuator is produced by passing a current through the surrounding actuator coil which, in turn, induces a magnetic field and causes longitudinal or axial vibration in the rod. Vibration perpendicular to the longitudinal rod

axis is assumed insignificant for this study. The equation of motion (Thompson, 1988) for this longitudinal Terfenol-D rod vibration is found from applying Newton's law of motion to a strained differential rod element producing:

$$\frac{\partial^2 v_T}{\partial t^2} = (C^H)^2 \frac{\partial^2 v_T}{\partial y^2} \quad (2)$$

where:  $C^H = \sqrt{\frac{\bar{Y}^H}{\rho}}$

$$\bar{Y}^H = Y^H (1 + \eta j)$$

$\bar{Y}^H$  is the Youngs Modulus of Terfenol-D (constant magnetic field)

$\eta$  is the mechanical loss factor of Terfenol-D

$\rho$  is the density of Terfenol-D

$C^H$  is the propagation speed of sound in the Terfenol-D (constant magnetic field)

$v_T$  is the displacement of the rod in the y-direction

The solution to this differential equation has the following form:

$$v_T = \bar{v}_T e^{j\omega t} = [A \sin(\kappa_T y) + B \cos(\kappa_T y)] e^{j\omega t} \quad (3)$$

where:  $v_T$  is the displacement of the rod

$\bar{v}_T$  is the spatial displacement of the rod

$\omega$  is the vibration frequency

$\kappa_T$  is the wave number

A,B are arbitrary constants

and: 
$$\kappa_T = \frac{\omega}{C^H}$$

Note that all quantities with a bar notation indicate a spatial domain term except for the Youngs Modulus which indicates a complex variable.

The Terfenol-D rod is fixed at  $y = 0$  as shown in Fig. 2.8. Applying this boundary condition to the displacement relationship yields:

$$\bar{v}_T(0) = 0, B = 0$$

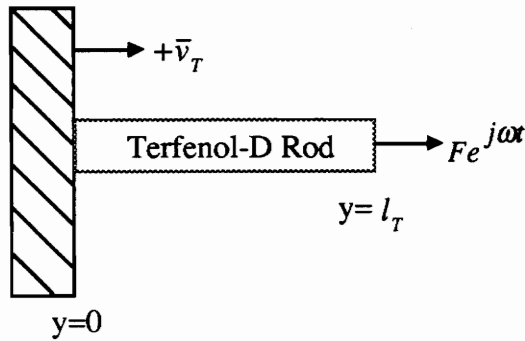


Figure 2.8: Representation of the Terfenol-D Rod With a Fixed Boundary Condition and Applied External Force

The equation of motion then becomes:

$$\bar{v}_T(y) = A \sin(\kappa_T y) \tag{4}$$

and

$$v_T(y) = [A \sin(\kappa_T y)] e^{j\omega x} \tag{5}$$

The impedance expression for the Terfenol-D rod first needs to be developed. Consider a Terfenol-D rod with no applied magnetic field. If a force  $F e^{j\omega x}$  is applied at  $y = l_T$  as is shown in Fig. 2.8, then the corresponding rod strain is:

$$S(l_T) = \left. \frac{dv_T(y)}{dy} \right|_{y=l_T} = [A \kappa_T \cos(\kappa_T l_T)] e^{j\omega x} \quad (6)$$

The stress  $T$  at  $y = l_T$  is related to both the rod strain  $S$  and applied force  $F$  as:

$$T(l_T) = S(l_T) \bar{Y}^H = \frac{F(l_T)}{A_T} \quad (7)$$

where:  $A_T$  is the cross-sectional area of the Terfenol-D rod

Plugging Eq. (6) into Eq. (7) and solving for the force  $F$  yields:

$$F(l_T) = A_T \bar{Y}^H A \kappa_T \cos(\kappa_T l_T) e^{j\omega x} \quad (8)$$

The  $A$  constant is then found to be:

$$A = \frac{F(l_T)}{\bar{Y}^H A_T \kappa_T \cos(\kappa_T l_T) e^{j\omega x}} \quad (9)$$

For the impedance definition Eq. (1), the velocity as a function of rod position is:

$$\dot{v}_T(y) = j\omega[A \sin(\kappa_T y)]e^{j\omega x} \quad (10)$$

The velocity at  $y = l_T$  is:

$$\dot{v}_T(l_T) = j\omega[A \sin(\kappa_T l_T)]e^{j\omega x} \quad (11)$$

Eliminating the constant A by plugging Eq. (9) into Eq. (11) yields:

$$\dot{v}_T(l_T) = j\omega \left[ \frac{F(l_T)}{\bar{Y}^H A_T \kappa_T \cos(\kappa_T l_T) e^{j\omega x}} \right] [\sin(\kappa_T l_T)] e^{j\omega x}$$

Further simplification yields:

$$\dot{v}_T(l_T) = F(l_T) \left\{ j\omega \frac{l_T}{\bar{Y}^H A_T} \left[ \frac{\tan(\kappa_T l_T)}{\kappa_T l_T} \right] \right\} \quad (12)$$

The static stiffness of the Terfenol-D rod is defined as:

$$K_T = \frac{A_T \bar{Y}^H}{l_T} \quad (13)$$

Plugging the static stiffness Eq. (13) into Eq. (12) yields:

$$\dot{v}_T(l_T) = F(l_T) \left\{ \frac{j\omega}{K_T} \left[ \frac{\tan(\kappa_T l_T)}{\kappa_T l_T} \right] \right\} \quad (14)$$



The impedance definition Eq. (1) relates applied force  $F(l_T) = F e^{j\omega x}$  and corresponding velocity. Both of these terms are present in Eq. (14). Therefore, Eq. (14) can be rearranged to yield the impedance expression of the Terfenol-D rod as:

$$Z_T = \frac{F(l_T)}{\dot{v}_T(l_T)} = \frac{1}{\frac{j\omega}{K_T} \left[ \frac{\tan(\kappa_T l_T)}{\kappa_T l_T} \right]} = \frac{K_T}{j\omega} \left[ \frac{\kappa_T l_T}{\tan(\kappa_T l_T)} \right] \quad (15)$$

The Terfenol-D rod, once inserted into the actuator system, has different boundary conditions at  $y = l_T$ . The entire mechanical impedance diagram is again shown in Fig. 2.9.

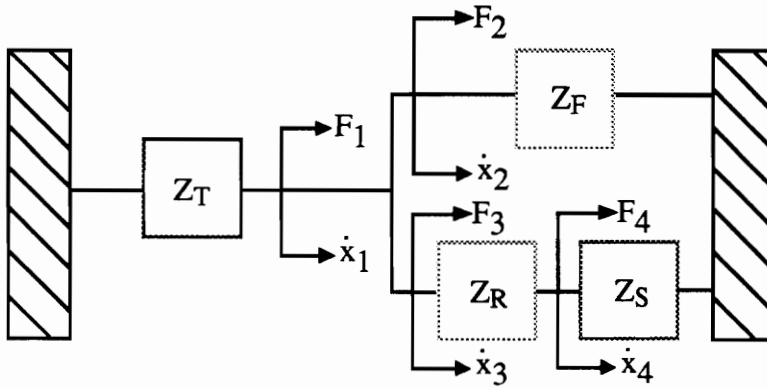


Figure 2.9: Mechanical Impedance Model of the Terfenol-D Actuator

The first simplification of the system impedance diagram shown in Fig. 2.9 involves combining the series combination of the rod impedance  $Z_R$  and external structure impedance  $Z_S$  into a lumped impedance  $Z_C$  shown as:

$$Z_C = \frac{Z_R Z_S}{Z_R + Z_S} \quad (16)$$

A further simplification combines the fixture impedance  $Z_F$  and the lumped series impedance  $Z_C$ . The only elements remaining in the condensed model are that of the Terfenol-D and all external impedances represented as  $Z_H$ :

$$Z_H = Z_F + Z_C = Z_F + \frac{Z_R Z_S}{Z_R + Z_S} \quad (17)$$

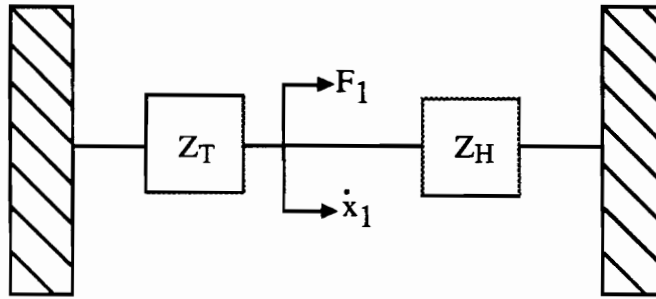


Figure 2.10: Condensed Actuator Impedance Model

The constant  $A$  must be found again for the revised boundary conditions. Using the impedance definition Eq. (1), the stress at  $y = l_T$  is:

$$T(l_T) = \frac{F(l_T)}{A_T} = \frac{-Z_H \dot{v}(l_T)}{A_T} = \frac{-Z_H v(l_T)}{A_T} j\omega \quad (18)$$

where:  $T$  is the stress on the rod

$A_T$  is the cross-sectional area of the Terfenol-D rod  
 $Z_H$  is the external impedance including fixturing and output shaft

Plugging in the displacement at  $y = l_T$  Eq. (4) yields the spatial rod stress as:

$$\bar{T}(l_T) = -\frac{[Z_H][A \sin(\kappa_T l_T)]}{A_T} j\omega \quad (19)$$

To solve for the A constant, the stress and displacement relationships will be plugged into the first constitutive equation for Terfenol-D. The two constitutive equations for Terfenol-D are:

$$S = s^H T + dH \quad (20)$$

$$B = dT + \mu^T H \quad (21)$$

where:

- $S$  is the strain
- $s^H$  is the material compliance (constant magnetic field)
- $T$  is the stress
- $d$  is the "d" constant that relates the applied magnetic field to induced strain
- $H$  is the applied magnetic field
- $B$  is the flux density
- $\mu^T$  is the material permeability (constant stress)

After substitution, the first constitutive equation becomes:

$$\bar{S}(l_T) = \bar{s}^H \left[ -\frac{[Z_H][A \sin(\kappa_T l_T)]}{A_T} j\omega \right] + dH \quad (22)$$

Another expression including the A constant is obtained by finding the rod strain directly from the displacement relationship Eq. (4):

$$\bar{S}(y) = \frac{d\bar{v}_T(y)}{dy} = A\kappa_T \cos(\kappa_T y) \quad (23)$$

The strain at  $y = l_T$  is:

$$\bar{S}(l_T) = A\kappa_T \cos(\kappa_T l_T) \quad (24)$$

Setting the two strain relationships Eqs. (22),(24) together yields:

$$A\kappa_T \cos(\kappa_T l_T) = -\bar{s}^H \left[ \frac{[Z_H][A \sin(\kappa_T l_T)]}{A_T} j\omega \right] + dH$$

Combining terms and solving for A yields:

$$A = \frac{dH}{\kappa_T \cos(\kappa_T l_T) + j\omega \left[ \frac{\bar{s}^H}{A_T} \right] [Z_H][\sin(\kappa_T l_T)]} \quad (25)$$

Rearrangement of the Terfenol-D static stiffness Eq. (13) gives:

$$\frac{1}{K_T l_T} = \frac{\bar{s}^H}{A_T} \quad (26)$$

Substitution of Eq. (26) into Eq. (25) and simplification yields:

$$A = \frac{\frac{dH}{\kappa_T \cos(\kappa_T l_T)}}{1 + [Z_H] \left[ \frac{j\omega}{K_T} \right] \left[ \frac{\tan(\kappa_T l_T)}{\kappa_T l_T} \right]} \quad (27)$$

Notice in the denominator of Eq. (27) the inverse of the Terfenol impedance:

$$\frac{1}{Z_T} = \left[ \frac{j\omega}{K_T} \right] \left[ \frac{\tan(\kappa_T l_T)}{\kappa_T l_T} \right]$$

The A constant then simplifies to:

$$A = \frac{dHZ_T}{\kappa_T \cos(\kappa_T l_T) [Z_T + Z_H]} \quad (28)$$

The equation of motion along the rod comes from plugging into the displacement equation Eq. (4) yielding:

$$\bar{v}(y) = \frac{dH}{\kappa_T} \left[ \frac{Z_T}{Z_T + Z_H} \right] \left[ \frac{\sin(\kappa_T y)}{\cos(\kappa_T l_T)} \right] \quad (29)$$

The displacement at the rod end is:

$$\bar{x}_1 = \bar{v}(l_T) = dHl_T \left[ \frac{Z_T}{Z_T + Z_H} \right] \left[ \frac{\tan(\kappa_T l_T)}{\kappa_T l_T} \right] \quad (30)$$

The velocity at the rod end is:

$$\bar{\dot{x}}_1 = j\omega dHl_T \left[ \frac{Z_T}{Z_T + Z_H} \right] \left[ \frac{\tan(\kappa_T l_T)}{\kappa_T l_T} \right] \quad (31)$$

The strain along the rod length is found to be:

$$\bar{S}(y) = dH \left[ \frac{Z_T}{Z_T + Z_H} \right] \left[ \frac{\cos(\kappa_T y)}{\cos(\kappa_T l_T)} \right] \quad (32)$$

The strain at  $y = l_T$  is:

$$\bar{S}(l_T) = dH \left[ \frac{Z_T}{Z_T + Z_H} \right] \quad (33)$$

The stress along the rod length can be found by substituting into the first constitutive equation for Terfenol-D Eq. (20). Solving for T gives:

$$\bar{T}(y) = \bar{Y}^H dH \left\{ \left[ \frac{Z_T}{Z_T + Z_H} \right] \left[ \frac{\cos(\kappa_T y)}{\cos(\kappa_T l_T)} \right] - 1 \right\} \quad (34)$$

The stress at  $y = l_T$  is:

$$\bar{T}(l_T) = \bar{Y}^H dH \left\{ \left[ \frac{Z_T}{Z_T + Z_H} \right] - 1 \right\} \quad (35)$$

The stress expression Eq. (34) will yield the force at the end of the Terfenol-D rod ( $y = l_T$ ) as:

$$\bar{F}_1 = \bar{F}(l_T) = -A_T \bar{Y}^H dH \left[ \frac{Z_H}{Z_T + Z_H} \right] \quad (36)$$

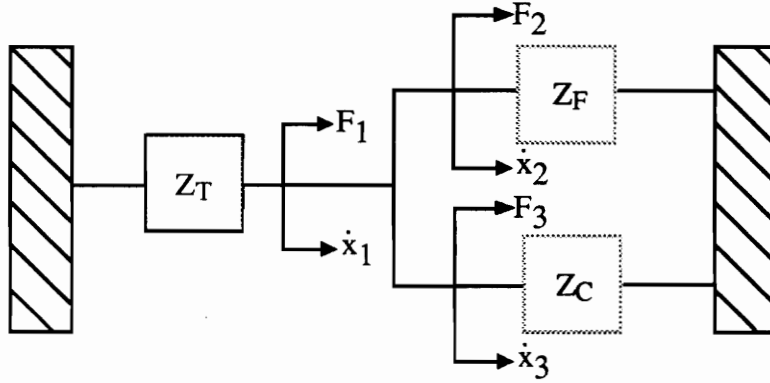


Fig. 2.11: Actuator Impedance Configuration With Lumped Rod and External Impedances

This force output Eq. (36) and the displacement Eq. (30) at the end of the Terfenol-D rod is then passed on to the other components in the system. Analysis of this force and displacement translation will yield the output force and stroke of the actuator. Figure 2.11 shows the actuator system with the series combination impedance  $Z_C$  Eq. (16). Note that in Fig. 2.11,  $\bar{x}_3 = \bar{x}_2 = \bar{x}_1$ . The force  $\bar{F}_3$  can be found from:

$$\bar{F}_3 = Z_C \bar{\dot{x}}_3 = Z_C \bar{\dot{x}}_1 \quad (37)$$

Once the force applied to  $Z_C$  is found, the next step is to find the displacement loss across the rod impedance  $Z_R$ . To do this the actuator impedance representation should again be broken down as was shown in Fig. 2.10. This complete actuator representation is shown again in Fig. 2.12.

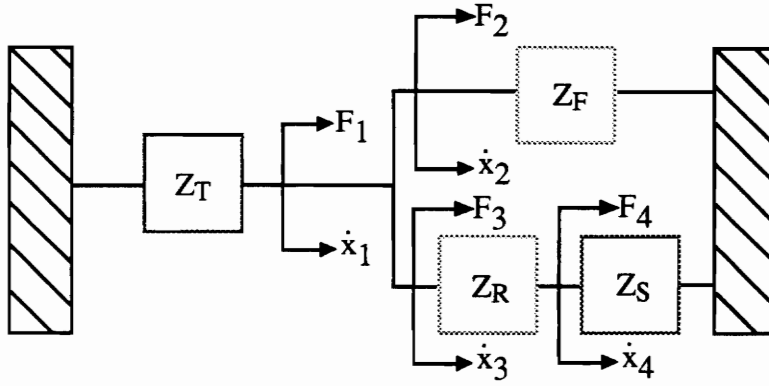


Figure 2.12: Impedance Model of the Terfenol-D Actuator

If the rod impedance  $Z_R$  is a lumped element, the displacement loss across that impedance is found to be:

$$\bar{x}_3 - \bar{x}_4 = \frac{\bar{F}_3}{Z_R} \quad (38)$$

However, the rod is a continuous element and Eq. (38) cannot be used to accurately describe the displacement loss or force transfer of the rod. First, consider the actuator in a blocked configuration where the rod or actuator output shaft has a force applied to one



end and is fixed at the other as seen in Fig. 2.13. These boundary conditions are identical to those applied to the Terfenol-D rod inside the actuator. The development of the rod impedance  $Z_R$  is similar to that of the Terfenol-D rod. The solution to the equation of motion for the continuous rod is:

$$v_R(y) = (A \sin \kappa_R y + B \cos \kappa_R y) e^{j\omega t} \quad (39)$$

where:  $\kappa_R$  is the rod wave number defined as  $\omega/C_R$

The rod strain  $S_R$  as a function of rod position is:

$$S_R(y) = \frac{dv_R(y)}{dy} = (\kappa_R A \cos \kappa_R y - \kappa_R B \sin \kappa_R y) e^{j\omega t} \quad (40)$$

The force  $F_R$  in the rod as a function of rod position is found from the rod stress  $T_R$  as:

$$F_R(y) = A_R T_R(y) = A_R \bar{Y}_R S_R(y) \quad (41)$$

where:  $A_R$  is the rod cross-sectional area

Substituting Eq. (40) into Eq. (41) yields:

$$F_R(y) = [A_R \bar{Y}_R \kappa_R (A \cos \kappa_R y - B \sin \kappa_R y)] e^{j\omega t} \quad (42)$$

The force at  $y = 0$  is defined as:

$$F_R(0) = -Z_R \dot{v}_R \Big|_{y=0} = -Z_R j\omega v_R(0) \quad (43)$$

The rod impedance  $Z_R$  is thus defined as:

$$Z_R = \frac{-F_R(0)}{j\omega v_R(0)} \quad (44)$$

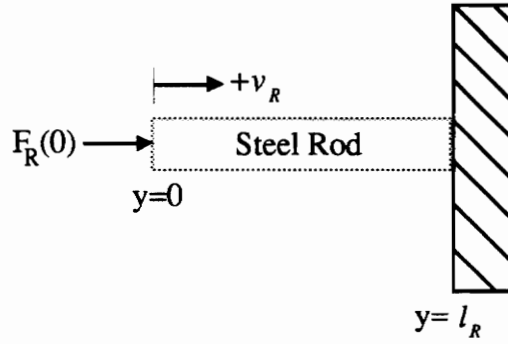


Figure 2.13: Actuator Output Rod With Fixed Boundary Condition

The force and displacement at  $y = 0$  are found to be:

$$F_R(0) = (A_R \bar{Y}_R \kappa_R A) e^{j\omega x} \quad (45)$$

$$v_R(0) = B e^{j\omega x} \quad (46)$$

The constant B in Eq. (46) can be found by applying the fixed position boundary condition at  $y = l_R$ .

$$v_R(l_R) = 0 = (A \sin \kappa_R l_R + B \cos \kappa_R l_R) e^{j\omega x} \quad (47)$$

Rearrangement of Eq. (47) gives:

$$B = -A \tan \kappa_R l_R \quad (48)$$

Plugging Eqs. (45),(46) and (48) into the rod impedance expression Eq. (44) and some manipulation yields:

$$Z_R = \frac{A_R \bar{Y}_R \kappa_R}{j\omega \tan \kappa_R l_R} = \frac{1}{j\omega} \left[ \frac{A_R \bar{Y}_R}{l_R} \right] \left[ \frac{\kappa_R l_R}{\tan \kappa_R l_R} \right] \quad (49)$$

The rod stiffness is defined as:

$$K_R = \frac{A_R \bar{Y}_R}{l_R} \quad (50)$$

where:  $\bar{Y}_R = Y_R (1 + \eta j)$

$K_R$  is the rod static stiffness

$l_R$  is the rod length

Substituting Eq. (50) into Eq. (49) yields the rod impedance expression for the actuator in the blocked configuration as:

$$Z_R|_{blocked} = \frac{K_R}{j\omega} \left[ \frac{\kappa_R}{\tan \kappa_R l_R} \right] \quad (51)$$

The other extreme boundary condition is for the free actuator where  $Z_s = 0$ . Figure 2.14

shows the blocked and free actuator configurations and the flow of force from the end of the Terfenol-D rod at point A along paths B and C. Notice that when  $Z_s = 0$  in the free case, path C is no longer complete and the force applied at point A flows only along path B with the excess used to accelerate the rod mass.

With  $Z_s = 0$  the series combination  $Z_c$  becomes:

$$Z_c \Big|_{free} = Z_{RM} \quad (52)$$

where:  $Z_{RM}$  is the rod impedance assuming the rod behaves as a mass.

$$Z_{RM} = j\omega m_{rod}$$

$m_{rod}$  is the mass of the rod

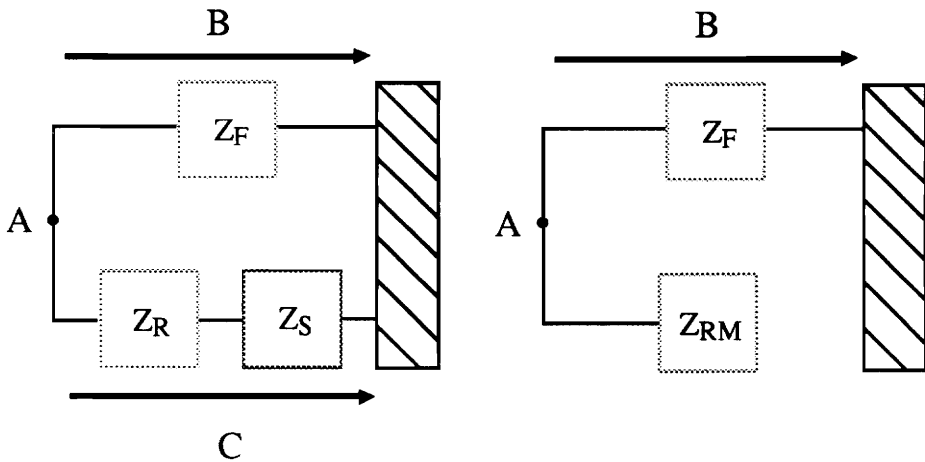


Figure 2.14: Blocked and Free Actuator End Configurations

Plugging  $Z_c \Big|_{free}$  Eq. (52) into the equivalent external impedance  $Z_H$  Eq. (17) yields:

$$Z_H|_{free} = Z_F + Z_{RM} \quad (53)$$

Because  $\bar{x}_3 = \bar{x}_2 = \bar{x}_1$ , the actuator output free velocity  $\bar{\dot{x}}_3$  is found from plugging Eq. (53) into Eq. (31) yielding:

$$\bar{\dot{x}}_3|_{free} = j\omega d H l_T \left[ \frac{Z_T}{Z_T + Z_F + Z_{RM}} \right] \left[ \frac{\tan(\kappa_T l_T)}{\kappa_T l_T} \right] \quad (54)$$

The output force with free actuator boundary conditions is zero as expected.

An impedance expression for the rod has been developed for both the free and blocked actuator boundary conditions. However, neither of these expressions is completely valid for external impedances in between those extremes in boundary conditions. Therefore, a continuous rod impedance using transmission line methods (Snowdon, 1968; Harris, 1988) is developed and is valid for any actuator boundary condition.

The transmission line methods are based on an analogy to the electrical impedance of infinitely long transmission lines (Snowdon, 1968). The assumption of infinite length initially allows for disregard to changes in driving point impedance as a result of reflections that occur at some distance down the line. The transmission line impedance expression is based on the complete solution to the progressive wave solution which accounts for left and right traveling waves and the phase difference between corresponding waves as a function of time. The complete progressive wave solution is:

$$v_R = v_{R_o} \left[ e^{-j\kappa_* x} + (\text{Re } j\phi_*) e^{j\kappa_* x} \right] e^{j\omega x}$$

where:  $v_{R_0}$  is the wave amplitude  
 $\kappa_R$  is the wave number  
 $x$  is the position along the rod

The magnitude and phase of the reflected or left traveling wave are represented by  $R$  and  $\phi_R$ . The values of  $R$ ,  $\phi_R$ , and  $v_{R_0}$  are determined from the boundary conditions of the system and the type of system impedance change which causes a reflection.

The driving point rod impedance without any reflections is known as the characteristic impedance and is given as:

$$Z_O = A_R \sqrt{Y_R \rho_R}$$

where:  $A_R$  is the rod cross-sectional area  
 $Y_R$  is the rod Youngs Modulus  
 $\rho_R$  is the rod density

The rod impedance expression including a reflection is found from substituting the progressive wave solution and force at  $x = 0$  (input force) into the general impedance expression Eq. (1). The input force is equal to the Youngs Modulus multiplied by the strain at  $x = 0$ . This is the same as was done in Eq. (6). The resulting impedance expression is:

$$Z_R = Z_O \left[ \frac{1 - \text{Re}^{-j2\kappa_R l}}{1 + \text{Re}^{-j2\kappa_R l}} \right] \quad (55)$$

where:  $l$  is the distance between the driving point and the reflection

The driving point impedance at the reflecting device where  $l = 0$ , is the external impedance  $Z_s$  shown in Fig. 2.11.

$$Z_s = Z_o \left[ \frac{1 - R}{1 + R} \right] \quad (56)$$

From Eq. (56), R is found to be:

$$R = - \left[ \frac{Z_s - Z_o}{Z_s + Z_o} \right] \quad (57)$$

Plugging R Eq. (57) into the rod impedance expression Eq. (55) yields:

$$Z_R = Z_o \left[ \frac{1 + \left( \frac{Z_s - Z_o}{Z_s + Z_o} \right) e^{-j2\kappa_R l}}{1 - \left( \frac{Z_s - Z_o}{Z_s + Z_o} \right) e^{-j2\kappa_R l}} \right]$$

Further simplification yields:

$$Z_R = Z_o \left[ \frac{Z_s (1 + e^{-j2\kappa_R l}) + Z_o (1 - e^{-j2\kappa_R l})}{Z_s (1 - e^{-j2\kappa_R l}) + Z_o (1 + e^{-j2\kappa_R l})} \right] \quad (58)$$

Dividing the numerator and denominator of Eq. (58) by  $(1 + e^{-j2\kappa_R l})$  yields:

$$Z_R = Z_O \left[ \frac{Z_S + Z_O \left( \frac{1 - e^{-j2\kappa_R l}}{1 + e^{-j2\kappa_R l}} \right)}{Z_O + Z_S \left( \frac{1 - e^{-j2\kappa_R l}}{1 + e^{-j2\kappa_R l}} \right)} \right] \quad (59)$$

Further simplification of Eq. (59) can be performed using the natural log exponential expressions for sine and cosine:

$$\sin(\kappa_R l) = \frac{e^{j\kappa_R l} - e^{-j\kappa_R l}}{2j} \quad \cos(\kappa_R l) = \frac{e^{j\kappa_R l} + e^{-j\kappa_R l}}{2} \quad (60)$$

Combining the two expressions in Eq. (60) yields:

$$j \tan(\kappa_R l) = \frac{e^{j\kappa_R l} - e^{-j\kappa_R l}}{e^{j\kappa_R l} + e^{-j\kappa_R l}} = \frac{1 - e^{-j2\kappa_R l}}{1 + e^{-j2\kappa_R l}} \quad (61)$$

Substituting Eq. (61) into the rod impedance expression Eq. (59) yields:

$$Z_R = Z_O \left[ \frac{Z_S + jZ_O \tan(\kappa_R l)}{Z_O + jZ_S \tan(\kappa_R l)} \right] \quad (62)$$

This developed continuous rod impedance expression Eq. (62) is presented by Snowdon (1968) and Harris (1988). Further characterization of the force transfer and displacement loss across the rod (Harris, 1988) gives:



$$\dot{\bar{x}}_4 = \frac{Z_O \dot{\bar{x}}_1}{Z_O \cos(\kappa_R l_R) + jZ_S \sin(\kappa_R l_R)} \quad (63)$$

$$\bar{F}_4 = \frac{Z_O Z_S \dot{\bar{x}}_1}{Z_O \cos(\kappa_R l_R) + jZ_S \sin(\kappa_R l_R)} \quad (64)$$

- where:
- $\dot{\bar{x}}_1$  is the rod velocity at  $l = 0$
  - $\dot{\bar{x}}_4$  is the rod velocity at the end of the rod (at the boundary condition)
  - $\bar{F}_3$  is the input (applied) force at  $l = 0$
  - $\bar{F}_4$  is the output force of the rod and of the actuator
  - $Z_S$  is the external impedance
  - $Z_O$  is the output rod characteristic impedance

The output displacement of the rod can be simply found by dividing both sides of Eq. (63) by a heviside operator. Note that  $\bar{F}_4$  and  $\dot{\bar{x}}_4$  are graphically identified in the actuator impedance diagram shown previously in Fig. 2.12.

The above expressions define the dynamic relationships associated with the continuous actuator output shaft. This development shows that the rod impedance is coupled with the boundary conditions and cannot be separated if a continuous impedance expression is used. The developed driving point impedance completely characterizes the impedance of the rod and the attached external structure designated as  $Z_S$ .

For a fixed boundary condition where  $Z_S = \infty$ , the actuator blocking force becomes:

$$\bar{F}_4|_{\text{blocked}} = \frac{\bar{F}_3}{\cos(\kappa_R l)} \quad (65)$$

As expected, by plugging  $Z_s = \infty$  into Eq. (63), the output velocity vanishes:

$$\dot{\bar{x}}_4 = 0$$

For a free boundary condition, by plugging  $Z_s = 0$  into Eq. (64), the output force vanishes:

$$\bar{F}_4 = 0$$

The free stroke velocity becomes:

$$\dot{\bar{x}}_4 = \frac{\dot{\bar{x}}_3}{\cos(\kappa_R l)}$$

More importantly, the free stroke rod impedance becomes:

$$Z_R = jZ_O \tan(\kappa_R l) \quad (66)$$

The free stroke rod impedance Eq. (66) is numerically equivalent to assuming the rod impedance as a lumped mass (Harris, 1988) as was previously discussed.

Also, the continuous rod impedance expression Eq. (51) previously developed specifically for a blocked actuator boundary condition is mathematically identical to the general rod

impedance expression Eq. (62) developed using transmission line methods with the rod boundary condition set to  $Z_s = \infty$ .

## 2.5 Electrical Aspects

When a current  $I$  is passed through the turns of an empty coil or solenoid, the effective magnetic flux passes through the coil ends (Halliday and Resnick, 1988) as is shown in Fig. 2.15. Insertion of any ferromagnetic material such as Terfenol-D into the coil alters the resulting magnetic flux density and flux when a current is passed through the coil windings. The flux density  $B$  of the coil and Terfenol-D combination is simply that of the Terfenol-D and is described by the second constitutive equation Eq. (21).

$$B = dT + \mu^T H$$

The total flux  $\Phi$  is defined as:

$$\Phi = \int B dA$$

Therefore, the area through which the flux flows is the cross-sectional area of the Terfenol rod assuming that the wires of the coil themselves contribute insignificantly to that area. The total flux is:

$$\Phi = BA_T \tag{67}$$

Plugging the stress  $T(y)$  Eq. (34) into the second constitutive equation Eq. (21) yields:

$$B = \bar{Y}^H dH \left\{ \left[ \frac{Z_T}{Z_T + Z_H} \right] \left[ \frac{\cos(\kappa_T y)}{\cos(\kappa_T l_T)} \right] - 1 \right\} d + \mu^T H$$

Further simplification yields:

$$B = \left\{ d^2 \bar{Y}^H \left[ \frac{Z_T}{Z_T + Z_H} \right] \left[ \frac{\cos(\kappa_T y)}{\cos(\kappa_T l_T)} \right] - d^2 \bar{Y}^H + \mu^T \right\} H \quad (68)$$

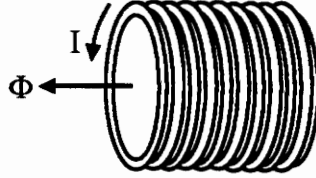


Figure 2.15: The Magnetic Flux Created By a Current Passing Through a Coil

In Eq. (68) the term in brackets is seen as the effective permeability. All the terms inside the bracket except for the free permeability ( $\mu^T$ ) are a result of the mechanical interaction.

Plugging Eq. (68) into Eq. (67) yields:

$$\Phi(y) = \left\{ d^2 \bar{Y}^H \left[ \frac{Z_T}{Z_T + Z_H} \right] \left[ \frac{\cos(\kappa_T y)}{\cos(\kappa_T l_T)} \right] - d^2 \bar{Y}^H + \mu^T \right\} A_T H \quad (69)$$

If the coil is assumed to act only as an inductor then the inductance L (Halliday and Resnick, 1988) is defined as:

$$L = \frac{N\Phi}{I} \quad (70)$$

where: L is the inductance  
N is the total number of terms in the coil  
I is the current flowing through the coil

For an inductor, the voltage drop across the element is defined as the inductance times the time derivative of the current. Using a heviside operator and Eq. (70) the voltage across the inductor is defined as:

$$V(\omega) = Ll j\omega = N\Phi j\omega \quad (71)$$

Because terms in Eq. (71) are functions of rod position, the total voltage drop across the coils is found by integration. The number of turns in an incremental length dy is given as:

$$dN = \frac{N}{l_T} dy \quad (72)$$

Substituting Eqs. (69),(72) into Eq. (71) and manipulation of leading constants yields:

$$V_{tot} = \frac{j\omega N}{l_T} \int_0^{l_T} A_T H \left\{ d^2 \bar{Y}^H \left[ \frac{Z_T}{Z_T + Z_H} \right] \left[ \frac{\cos(\kappa_T y)}{\cos(\kappa_T l_T)} \right] - d^2 \bar{Y}^H + \mu^T \right\} dy \quad (73)$$

Integration, substitution of limits and simplification yields:

$$V_{\text{tot}} = j\omega N A_T H \left\{ d^2 \bar{Y}^H \left[ \frac{Z_T}{Z_T + Z_H} \right] \left[ \frac{\tan(\kappa_T l_T)}{\kappa_T l_T} \right] + (\mu^T - d^2 \bar{Y}^H) \right\} \quad (74)$$

The relationship between the applied magnetic field H and current I (Butler, 1988) is:

$$H = nI = \frac{NI}{l_T} \quad (75)$$

where:  $n = \frac{N}{l_T}$

$n$  is a number of turns per unit coil length ratio

Substituting Eq. (75) into Eq. (74) and some rearrangement provides the electrical impedance of the coil with the mechanical interaction included as:

$$Z_E = \frac{V_{\text{tot}}}{I} = \frac{j\omega N^2 A_T}{l_T} \left\{ d^2 \bar{Y}^H \left[ \frac{Z_T}{Z_T + Z_H} \right] \left[ \frac{\tan(\kappa_T l_T)}{\kappa_T l_T} \right] + (\mu^T - d^2 \bar{Y}^H) \right\} \quad (76)$$

## 2.6 Electro-magneto-mechanical Interaction

The development presented in the two previous subsections details the mechanical and electrical behaviors of the actuator system. Also presented is the actuator electro-magneto-mechanical interaction as a mathematical result of the constitutive relationships for Terfenol-D.

The mechanical behavior of the Terfenol-D rod is coupled to the electrical behavior as seen in the output stroke Eq. (31) and output force Eq. (36) shown again below.

$$\bar{x}_1 = j\omega d H l_T \left[ \frac{Z_T}{Z_T + Z_H} \right] \left[ \frac{\tan(\kappa_T l_T)}{\kappa_T l_T} \right] \quad (31)$$

$$\bar{F}_1 = \bar{F}(l_T) = -A_T \bar{Y}^H dH \left[ \frac{Z_H}{Z_T + Z_H} \right] \quad (36)$$

The output stroke and force each contain mechanical impedance expressions and a physical Terfenol-D dimension (area corresponding to force and length to displacement). However, each of the mechanical behavior expressions also contains a  $dH$  term which is a scale of the coil input current  $I$  from Eq. (75).

$$H = \frac{N}{l_T} I \quad (75)$$

Thus, the mechanical behavior is coupled to the electrical behavior. However, the coil input current  $I$  also has dynamics. The electrical resonance of the actual coil occurs at a frequency much greater than the frequency range of interest and is therefore not discussed. In general, the current in the actuator coil is a function of the applied voltage and electrical impedance as:

$$I = \frac{V}{Z_E}$$

The electrical impedance  $Z_E$  Eq. (76) is coupled to the mechanical behavior shown as:

$$Z_E = \frac{V}{I} = \frac{j\omega N^2 A_T}{l_T} \left\{ d^2 \bar{Y}^H \left[ \frac{Z_T}{Z_T + Z_H} \right] \left[ \frac{\tan(\kappa_T l_T)}{\kappa_T l_T} \right] + (\mu^T - d^2 \bar{Y}^H) \right\} \quad (76)$$

The mechanical interaction present in the electrical impedance expression Eq. (76) is a result of the mechanical impedance terms for the Terfenol-D rod and external impedances and from the Terfenol-D Youngs Modulus and the "d" constant which relates the Terfenol-D induced strain S to applied magnetic field H. Without the mechanical interaction terms, the electrical impedance expression reduces to that of only an inductor as expected and shown below:

$$Z_E = \frac{j\omega N^2 \mu^T A_T}{l_T}$$

The origination of the mechanical interaction stems from substitution into the second constitutive equation Eq. (21) for Terfenol-D.

$$B = dT + \mu^T H \quad (21)$$

Without the mechanical stress term T, the above relationship reduces to the simple magnetic relationship between flux density and applied field:

$$B = \mu H$$



The coil input current  $I$  is affected by the mechanical interaction terms in the electrical impedance  $Z_E$  as shown above. Because the mechanical behaviors of the Terfenol-D rod and the actuator include the coil current, the mechanical interaction terms in the electrical impedance also affect the mechanical behavior of the actuator. Further discussion of this coupled behavior is presented in a following section on transfer function representations.

## 2.7 Development of a Transduction Expression

Now that all input and output parameters of the magnetostrictive actuator have been defined and developed, these quantities will be used to form a transduction representation. One form of the transduction equations, known as the Mechanical Dual Form (Kinsler et al., 1982) are:

$$V = IZ_{EF} + \phi F \quad (77)$$

$$u = I\phi + \frac{F}{Z_{MO}} \quad (78)$$

where:

- $V$  is the voltage across the electrical leads of the actuator coil
- $I$  is the current in the actuator coil
- $Z_{EF}$  is the free electrical impedance
- $\phi$  is the transduction coefficient
- $F$  is the applied force
- $u$  is the free stroke velocity
- $Z_{MO}$  is the actuator mechanical impedance (open circuit,  $I = 0$ )

The free electrical impedance  $Z_{EF}$  is obtained by substituting  $Z_H|_{free} = Z_F + Z_{RM}$  into

the electrical impedance relationship Eq. (76).

The open circuit mechanical impedance  $Z_{MO}$  is found from the general impedance definition Eq. (1) as:

$$F = Z_{MO} \dot{x} \quad (79)$$

where:  $F$  is the external force applied to the actuator output rod  
 $\dot{x}$  is the resulting velocity

Therefore,  $Z_{MO}$  is simply the equivalent impedance of the mechanical system shown in Fig. 2.16.

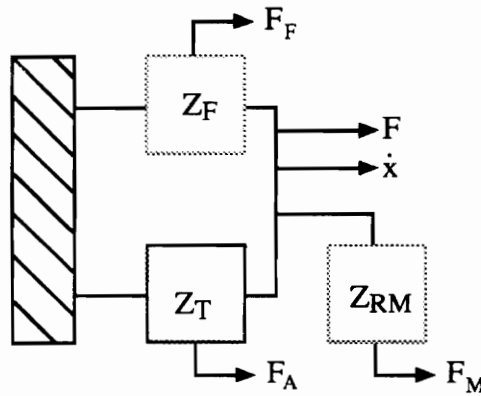


Fig. 2.16: Mechanical Impedance Configuration

The fixture impedance  $Z_F$ , Terfenol impedance  $Z_T$ , and rod impedance  $Z_{RM}$  are in parallel as seen in Fig. 2.16 and can be combined as:

$$Z_{MO} = Z_F + Z_T + Z_{RM} \quad (80)$$

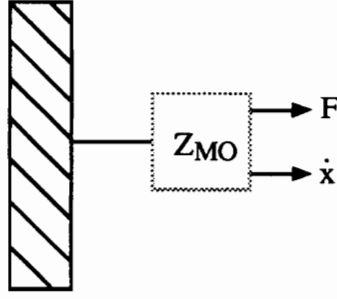


Fig. 2.17: Collapsed Mechanical Impedance Configuration

The force  $F_A$  acting on the Terfenol rod as a result of applying a force  $F$  to the actuator output rod is found as:

$$F_A = Z_T \dot{x} \quad (81)$$

The actuator velocity  $\dot{x}$ , caused by the applied force  $F$ , is found from Eq. (79) as:

$$\dot{x} = \frac{F}{Z_{MO}} \quad (82)$$

Plugging Eqs. (82),(80) into Eq. (81) yields the force seen by the Terfenol-D rod from the external application of force to the actuator as:

$$F_A = \left[ \frac{Z_T}{Z_F + Z_T + Z_{RM}} \right] F \quad (83)$$

The transduction coefficient  $\phi$  that is in each of the transduction equations Eqs. (77),(78)

is the only value needed to complete the actuator input/output relationships. Theoretically, the transduction coefficients should be equal or opposite in sign.

The transduction coefficient in the second equation Eq. (78) can be easily found by letting the applied force  $F$  equal zero which gives the actuator a free boundary condition.

$$u = \bar{x}_4|_{free} = j\omega d H l_T \left[ \frac{Z_T}{Z_T + Z_F + Z_{RM}} \right] \left[ \frac{\tan(\kappa_T l_T)}{\kappa_T l_T} \right]$$

Substituting for the magnetic field  $H$  Eq. (75) and rearrangement gives:

$$\bar{x}_4|_{free} = \left\{ j\omega d N \left[ \frac{Z_T}{Z_T + Z_F + Z_{RM}} \right] \left[ \frac{\tan(\kappa_T l_T)}{\kappa_T l_T} \right] \right\} I \quad (84)$$

From Eq. (84) the transduction coefficient  $\phi$  is found to be:

$$\phi = j\omega d N \left[ \frac{Z_T}{Z_T + Z_F + Z_{RM}} \right] \left[ \frac{\tan(\kappa_T l_T)}{\kappa_T l_T} \right] \quad (85)$$

The transduction coefficient expression Eq. (85) is developed by applying a free-actuator boundary condition to the second transduction equation Eq. (78). The impedance expressions in the denominator of the transduction expression are  $Z_T + Z_H$ . When using the transduction equations for actuator behavior analysis with other boundary conditions, exchange the free  $Z_H$  for the general expression Eq. (17) which includes the continuous rod impedance  $Z_R$  and the external impedance  $Z_S$ .

The next logical step is to verify the value of  $\phi$  in Eq. (85) by deriving the same value from the first transduction equation Eq. (77). This is done by assuming that there is no applied magnetic field  $H$  and no applied current in the windings of the actuator coil. The first transduction equation is then reduced to:

$$V|_{INDUCED} = \phi F \quad (86)$$

$V|_{INDUCED}$  is the voltage that develops across the open-circuit actuator coil leads when an external force  $F$  is applied to the actuator output rod. In this case ( $H = 0$ ) the Terfenol-D constitutive equations Eq. (20),(21) are also changed to:

$$S = s^H T \quad (87)$$

$$B = dT \quad (88)$$

The first step in verifying  $\phi$  is determining the variation of stress  $T$  in the Terfenol rod in terms of the external force  $F$ . The Terfenol rod spatial relationships for position  $\bar{v}_T$ , strain  $\bar{S}_T$ , stress  $\bar{T}_T$ , and force  $\bar{F}_T(y)$  with a fixed boundary condition at  $y = 0$  are shown again as:

$$\bar{v}_T(y) = A \sin(\kappa_T y)$$

$$\bar{S}_T(y) = \frac{d\bar{v}_T(y)}{dy} = A \kappa_T \cos(\kappa_T y)$$

$$\bar{T}_T(y) = \frac{S(y)}{\bar{s}^H} = S(y)\bar{Y}^H = A\bar{Y}^H \kappa_T \cos(\kappa_T y) \quad (89)$$

$$\bar{F}_T(y) = A\bar{Y}^H \kappa_T A_T \cos(\kappa_T y) \quad (90)$$

The force on the Terfenol-D rod at  $y = l_T$  was previously shown as  $F_A$  Eq. (83). Substituting this boundary condition into Eq. (90) and rearrangement yields the value for the constant A as:

$$A = \frac{F_A}{\bar{Y}^H \kappa_T A_T \cos(\kappa_T l_T)} \quad (91)$$

Plugging A Eq. (91) into the stress distribution Eq. (89) yields:

$$\bar{T}_T(y) = \frac{F_A}{A_T \cos(\kappa_T l_T)} \cos(\kappa_T y) \quad (92)$$

Substituting Eq. (91) into the modified version of the second transduction equation Eq. (88) gives the induced flux B as:

$$B_{INDUCED}(y) = \frac{dF_A}{A_T \cos(\kappa_T l_T)} \cos(\kappa_T y) \quad (93)$$

The flux density  $\Phi$  is found by plugging Eq. (93) into Eq. (67) yielding:

$$\Phi_{INDUCED}(y) = B_{INDUCED}(y)A_T$$

and:

$$\Phi_{INDUCED}(y) = \frac{dF_A}{\cos(\kappa_T l_T)} \cos(\kappa_T y) \quad (94)$$

The total voltage drop induced across the actuator coil leads is found in the same way as is shown in the development shown in Eqs. (71),(72), and (73).

$$V_{INDUCED} = \int_0^{l_T} j\omega N \Phi_{INDUCED}(y) dy \quad (95)$$

Plugging Eq. (94) into Eq. (95) yields:

$$V_{INDUCED} = \int_0^{l_T} j\omega \left[ \frac{N}{l_T} \right] \frac{dF_A}{\cos(\kappa_T l_T)} \cos(\kappa_T y) dy$$

Further rearrangement, integration, and substitution of integration limits yields:

$$V_{INDUCED} = \left[ \frac{j\omega dNF_A}{l_T \cos(\kappa_T l_T)} \right] \left[ \frac{\sin(\kappa_T l_T)}{\kappa_T} \right]$$

and:

$$V_{INDUCED} = j\omega dN \left[ \frac{\tan(\kappa_T l_T)}{\kappa_T l_T} \right] F_A \quad (96)$$

Plugging in  $F_A$  Eq. (83) in terms of the applied external force  $F$  yields:

$$V_{INDUCED} = j\omega dN \left[ \frac{Z_T}{Z_T + Z_F + Z_R} \right] \left[ \frac{\tan(\kappa_T l_T)}{\kappa_T l_T} \right] F \quad (97)$$

From the second transduction equation,  $\phi$  was previously developed as:

$$\phi = j\omega dN \left[ \frac{Z_T}{Z_T + Z_F + Z_R} \right] \left[ \frac{\tan(\kappa_T l_T)}{\kappa_T l_T} \right] \quad (85)$$

Factoring Eq. (97) shows that:

$$V_{INDUCED} = \phi F$$

Therefore,  $\phi$  has been verified for both equations and the transduction representation is complete.

The final transduction equations including all derived quantities are shown on the following page with the original Terfenol-D constitutive equations in order to illustrate the electro-magneto-mechanical interaction and dynamic complexity in the modeled device.



The Original Terfenol-D Constitutive Equations

$$S = s^H T + dH$$

$$B = dT + \mu^T H$$

The Finalized Transduction Equations

$$u = j\omega dN \left[ \frac{Z_T}{Z_T + Z_H} \right] \left[ \frac{\tan(\kappa_T l_T)}{\kappa_T l_T} \right] I + \frac{F}{Z_T + Z_H}$$

$$V = \frac{j\omega N^2 A_T}{l_T} \left\{ d^2 \bar{Y}^H \left[ \frac{Z_T}{Z_T + Z_H} \right] \left[ \frac{\tan(\kappa_T l_T)}{\kappa_T l_T} \right] + (\mu^T - d^2 \bar{Y}^H) \right\} I + j\omega dN \left[ \frac{Z_T}{Z_T + Z_H} \right] \left[ \frac{\tan(\kappa_T l_T)}{\kappa_T l_T} \right] F$$

## 2.8 Analysis of the Terfenol-D Transducer

The general description of transducers presented in the Transduction Literature Review section presented two coupling coefficients. The first coupling coefficient  $k$ , based solely on material properties is shown again as:

$$k^2 = \frac{d^2}{s^H \mu^T}$$

The second coupling coefficient  $k$ , based on the transduction coefficient and electrical/mechanical system impedances, is derived from the canonical transduction expressions as:

$$k^2 = \frac{\phi_M^2}{Z_{EB} Z_{MO}}$$

- where:
- $\phi_M$  is the canonical transduction coefficient
  - $\phi$  is the mechanical dual form transduction coefficient Eq. (85)
  - $\phi = \phi_M / Z_{mo}$
  - $Z_{EB}$  is the blocked electrical impedance Eq. (76)
  - $Z_{MO}$  is the open-circuit mechanical impedance Eq. (80)

Also note that the measure of transducer efficiency, energy ratio or  $k^2$ , is the square of the coupling coefficient and is also shown above. The coupling coefficient derived from the two-port network analysis must be based on the canonical equations as shown above and presented in the Transducer Literature Review section of Chapter 1.

The dissipative power of an electrical circuit is defined as the amount of energy in the circuit which is converted from an electrical form to a non-electrical form (Nilsson, 1990). A simple example of this electrical power dissipation occurs with the conversion of electrical energy to thermal energy in a purely resistive circuit. The reactive power of a circuit is defined as the electrical energy which is passed between the inductance and capacitance elements and thus remains in the electrical circuit. The dissipative and reactive powers of the actuator are found using the electrical admittance shown below.

The electrical admittance  $Y_E$  of the actuator is defined as:

$$Y_E = \frac{1}{Z_E} \quad (98)$$

where:  $Z_E$  is the electrical impedance of the actuator

The dissipative power consumption of the actuator is:

$$P_D = \frac{V^2}{2} \operatorname{Re}(Y_E) \quad (99)$$

The reactive power of the actuator is:

$$P_R = \frac{V^2}{2} \operatorname{Im}(Y_E) \quad (100)$$

where:  $V$  is the input voltage

## 2.9 Creating Transfer Function Representations

The two transfer functions that will be measured experimentally are free-stroke to current and free-stroke to voltage ratios. Both of these transfer functions are derived from the free-stroke velocity expression given as:

$$\bar{\dot{x}}_3|_{free} = j\omega d H l_T \left[ \frac{Z_T}{Z_T + Z_F + Z_{RM}} \right] \left[ \frac{\tan(\kappa_T l_T)}{\kappa_T l_T} \right] \quad (54)$$

Multiplication of both sides of Eq. (54) by a Heaviside operator and separation of the electrical and mechanical terms yields the free stroke displacement as:

$$\bar{x}_3 = \left\{ d l_T \left[ \frac{Z_T}{Z_T + Z_F + Z_{RM}} \right] \left[ \frac{\tan(\kappa_T l_T)}{\kappa_T l_T} \right] \right\} H \quad (101)$$

The applied magnetic field is related to coil input current by Eq. (75):

$$H = \frac{N}{l_T} I \quad (75)$$

Therefore, the free-stroke to current transfer function becomes:

$$\frac{\bar{x}_3}{I} = d N \left[ \frac{Z_T}{Z_T + Z_F + Z_{RM}} \right] \left[ \frac{\tan(\kappa_T l_T)}{\kappa_T l_T} \right] \quad (102)$$

The free-stroke to voltage transfer function is produced in a similar manner to what is shown above. Plugging Eq. (75) into Eq. (101) produces:

$$\bar{x}_3 = \left\{ dl_T \left[ \frac{Z_T}{Z_T + Z_F + Z_{RM}} \right] \left[ \frac{\tan(\kappa_T l_T)}{\kappa_T l_T} \right] \right\} \frac{N}{l_T} I \quad (103)$$

The coil input current  $I$  is related to the electrical impedance  $Z_E$  and input voltage  $V$  by:

$$I = \frac{V}{Z_E} \quad (104)$$

Plugging Eq. (104) into Eq. (103) and manipulation yields the free-stroke to applied voltage transfer function shown as:

$$\frac{\bar{x}_3}{V} = \frac{dN}{Z_E} \left[ \frac{Z_T}{Z_T + Z_F + Z_{RM}} \right] \left[ \frac{\tan(\kappa_T l_T)}{\kappa_T l_T} \right] \quad (105)$$

Previously mentioned in the subsection description of the electro-magneto-mechanical interaction was the complexity of the above relationship Eq. (105). The electrical impedance  $Z_E$  Eq. (76) including the mechanical interaction terms is:

$$Z_E = \frac{j\omega N^2 A_T}{l_T} \left\{ d^2 \bar{Y}^H \left[ \frac{Z_T}{Z_T + Z_F + Z_{RM}} \right] \left[ \frac{\tan(\kappa_T l_T)}{\kappa_T l_T} \right] + (\mu^T - d^2 \bar{Y}^H) \right\} \quad (76)$$

The free-stroke to applied voltage transfer function thus contains the mechanical impedance terms a second time as a result of the device electro-magneto-mechanical

interaction.

## 2.10 Determination of Actuator Mechanical and Electrical Properties

The modeled Terfenol-D actuator was supplied by Intelligent Automation, Inc. (IAI) in Rockville, Maryland. The actuator system parameters identified by (IAI) are shown in Table 2.1.

Property	Symbol	Value	Units
Number of coil turns	N	2000	
Magnetic bias	$H_o$	500	Oe
Prestress	$\sigma_p$	2000	lb/in <sup>2</sup>

Table 2.1: Actuator System Parameters

The schematic of the actuator shown again in Fig. 2.18 does not include several actuator mechanical parameters including the prestress spring stiffness or the dimensions or specific material type of the output rod. These values could have been obtained with disassembly of the actuator. However, IAI requested that the actuator not be taken apart because of difficulties involved in correct reassembly. Therefore, the needed mechanical properties have been determined from measured actuator dynamic characteristics.

The actuator casing stiffness, prestress spring stiffness, spring mass, rod mass, and damping need to be determined. The actuator casing stiffness is determined from the following:

$$k_c = \frac{AY}{l}$$

where:  $A$  is the cross-sectional area for a hollow cylinder

$$A = \frac{\pi}{4} (d_o^2 - d_i^2)$$

$Y$  is the Youngs Modulus for steel

$l$  is the length of the casing

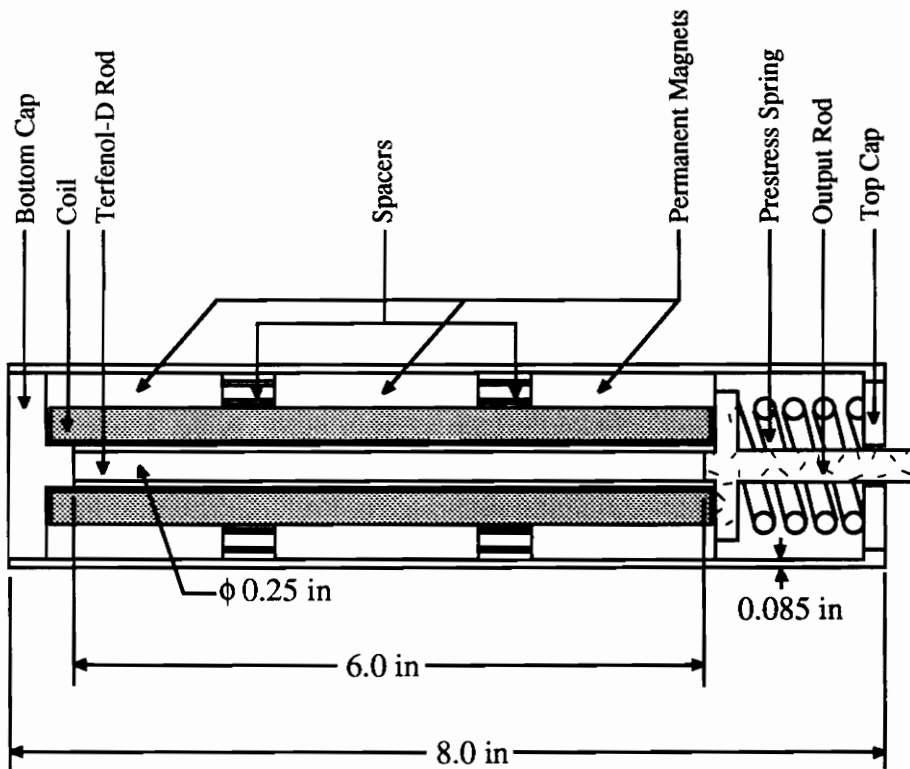


Figure 2.18: Schematic of the Terfenol-D Actuator (Haynes, Geng, and Teter, 1993)

Table 2.2 shows the casing dimensions, material properties, and calculated stiffness.

Property	Symbol	Value	Units
Outside diameter	$d_o$	5.08 e-2	$m$
Inside diameter	$d_i$	4.64 e-2	$m$
Cross-sectional area	$A$	3.29 e-4	$m^2$
Youngs Modulus	$Y$	207 e+9	$N/m^2$
Length	$l$	2.032 e-1	$m$
Calculated stiffness	$k_c$	3.36 e+8	$N/m$

Table 2.2: Actuator Casing Properties

The lender of the actuator was able to narrow down the spring stiffness  $k_s$  to a group of five possibilities that ranged from 1260  $lb/in$  to 5160  $lb/in$ . The value of 2000  $lb/in$  ( $3.50 \text{ e}+5 \text{ N/m}$ ) is chosen for use in initial investigations. The choice of spring mass  $m_s$  as 1 g or 0.001 kg is reasonable for the approximate size of the spring.

The output rod mass was obtained by approximating the dimensions of the rod from the provided schematic shown in Fig. 2.18. The chosen rod dimensions are shown in Fig. 2.19.

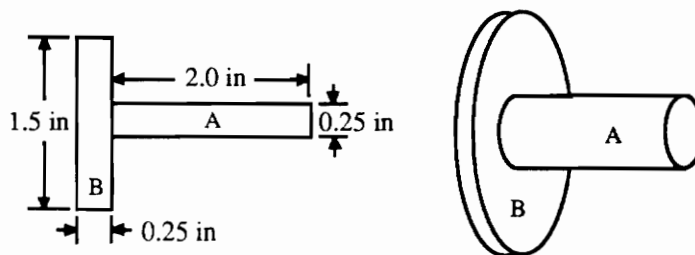


Figure 2.19: Dimensions of Actuator Output Rod



The mass of the rod was determined from:

$$m_R = \rho V = \rho(V_A + V_B)$$

where:  $m$  is the rod mass  
 $\rho$  is the rod density (steel)  
 $V$  is the total volume

$$V_A = \frac{\pi}{4} d_A^2 h_A$$

$$V_B = \frac{\pi}{4} d_B^2 h_B$$

The rod dimensions, material properties, calculated volumes, and calculated mass are found in Table 2.3.

Property	Symbol	Value	Units
Diameter A	$d_A$	3.81 e-2	$m$
Height A	$h_A$	6.35 e-3	$m$
Volume A	$V_A$	7.24 e-6	$m^3$
Diameter B	$d_B$	6.35 e-3	$m$
Height B	$h_B$	5.08 e-2	$m$
Volume B	$V_B$	1.61 e-6	$m^3$
Total Volume	$V$	8.85 e-6	$m^3$
Density	$\rho$	7.80 e+3	$kg/m^3$
Rod mass	$m_R$	6.90 e-2	$kg$

Table 2.3: Actuator Output Rod Properties

The internal damping loss factor for the casing is initially chosen as 0.001. The loss factor for the visco-elastic spring was chosen as 0.10. These values are later adjusted within an appropriate range in order to achieve improved theoretical to experimental correlation.

The dimensions of the Terfenol-D rod are obtained from the schematic in Fig. 2.18. The Youngs Modulus of the Terfenol-D is determined using the provided prestress and magnetic bias information and plots of strain vs. stress and strain vs. Youngs Modulus in Butler (1988). The Terfenol-D speed of sound can then be calculated using the representative Terfenol-D density given in Table 1.1.

The electrical properties of the Terfenol-D, specifically the permeability  $\mu$  and the "d" constant are also provided in Table 1.1 as representative or reasonable values. The permeability is baseline adjusted by using electrical impedance data taken from just the actuator coil itself. This separate coil was also provided by IAI for this purpose.

The theoretical electrical impedance of a coil inductor with a loss factor is defined as:

$$Z_{INDUCTOR} = j\omega L(1 - \eta_e j) = j\omega L + \eta_e \omega L$$

where:  $\eta_e$  is the inductive loss factor

$L$  is the coil inductance

$$L = \frac{\mu_0 N^2 A}{l}$$

$A$  is the cross-sectional area of the coil

$N$  is the number of coil turns

$l$  is the coil length  
 $\mu_o$  is the free permeability

By using the slopes of the real and imaginary portions of the coil electrical impedance, the actual free permeability of the coil and the loss factor can be found. However, these slopes are not linear because of coil electrical non-linearity. Therefore, linear approximations are made.

## 2.11 Determining the Lumped Fixture Impedance

The actuator fixturing consists of the exterior casing and prestress spring. The casing and spring constants are in series as shown in Fig. 2.20.

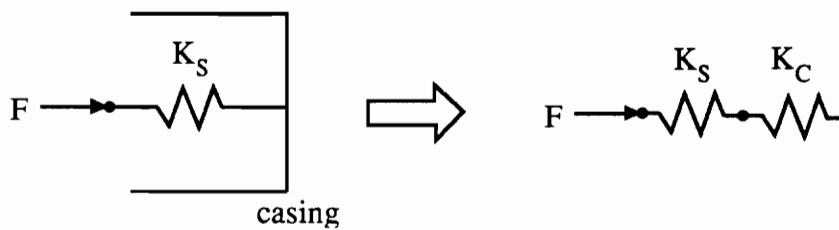


Figure 2.20: Fixturing Stiffness Configuration

An equivalent fixture stiffness  $k_{eq}$  is found from:

$$k_{eq} = \frac{k_s k_c}{k_s + k_c}$$

The equivalent spring stiffness is in parallel with the spring mass as shown in Fig. 2.21

below:

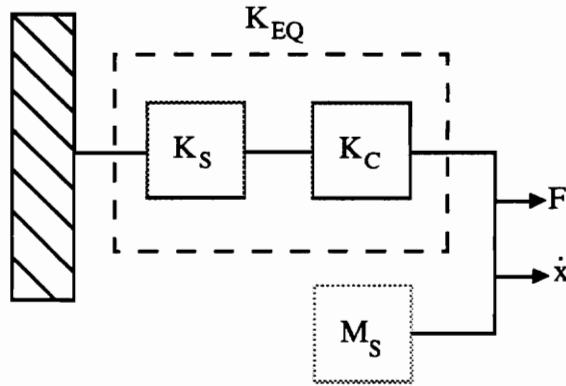


Figure 2.21: Complete Fixture Impedance Configuration

Recalling the mechanical impedance expressions for a lumped mass and stiffness in parallel, the total impedance of the actuator fixturing is:

$$Z_F = \left[ \omega m_s - \frac{k_{eq}}{\omega} \right] j$$

## 2.12 Concluding Remarks

This section details the complete theoretical development of a transduction representation for a Terfenol-D actuator. This task is accomplished through the application of an electro-magneto-mechanical impedance modeling approach which allows for a full investigation of the coupled behavior of the system.

The Terfenol-D rod is shown to have non-uniform strain behavior as a function of length, electrically-coupled stroke and force output, and mechanically-coupled electrical

impedance. The mechanically-coupled electric power consumption or dissipative power is also shown.

The development of a set of transduction or input/output expressions in terms of measurable quantities provides a useful tool for analysis of actuator behavior and efficiency. The particular transduction form chosen, known as the mechanical dual form, also contributes to the development of a collocated actuator/sensor using the Terfenol-D device.

Once the models of actuator electric and mechanical behaviors are modeled and the system coupling defined, the actual mechanical and electrical properties of the actuator are determined in preparation for experimental verification described in Chapter 3 of this thesis. The electrical portion of the actuator is also baseline adjusted in an attempt to minimize the effect of unmodeled electric non-linearity on the behavior models.

# Chapter 3

## Experimental Analysis

The experimental analysis of the Terfenol-D actuator serves several purposes. The first is to verify the electro-magneto-mechanical behavior models developed in Chapter 2. This is performed by taking transfer function data with a data acquisition system combined with an integrated signal processor. Electrical impedance data is obtained using an impedance gain/phase analyzer.

Experimental analysis also allows for investigation into the degree of non-linearity in actuator behavior which is most prevalent at low frequencies.

### 3.1 Experimental Setup

The collection of transfer function data is performed with a WCA or World Class Analyzer (Zonic) signal analyzer/data acquisition system. The WCA system shown in Fig. 3.1 is controlled through a Macintosh Quadra 950 system with 32 Mb of RAM and all data is displayed on a high-resolution, 13-inch color monitor. The Zonic Input Channel Module houses the analog-to-digital converters for 8 input channels with 16 bit accuracy. The real time sampling rate of the system is 40 kHz and the input amplitude can vary between  $\pm 0.01$  volts to 40 volts in the frequency range of dc to 40 kHz.

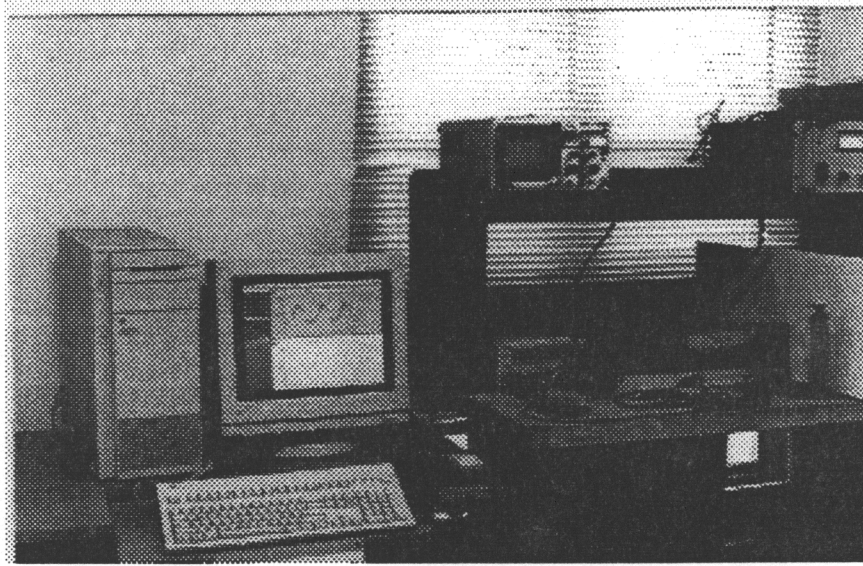


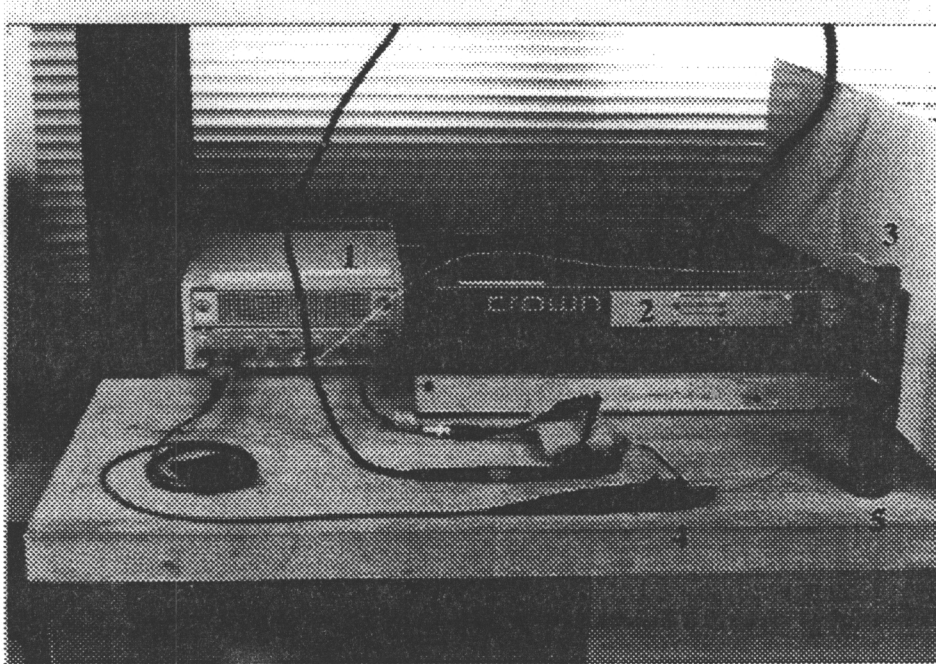
Figure 3.1: Macintosh Quadra 950 and WCA Zonic Experimental Setup Used for Data Acquisition and Signal Processing

The source of the actuator coil input is the signal function generator in the WCA. The various inputs used for signal analysis included electrical coil input in amplified form, coil current, the voltage drop across the coil, and the acceleration of the actuator output shaft.

The setup shown in Fig. 3.2 is used for measuring the free-stroke output to current transfer function. The function generator signal is amplified with a Crown Com-Tech 400 amplifier. The current in the actuator coil is obtained from a Tektronix P6021 current probe with a 2 mA/mV signal resolution. The actuator output acceleration is obtained from a Piezoelectronics (PCB) SN 8549 accelerometer. A JDR Instruments 2000 Oscilloscope is used to make sure the amplified function generator input is safely within the voltage limits of the WCA Zonic.

The WCA setup is modified slightly for obtaining the free-stroke to voltage transfer function. The voltage drop across the actuator coil is substituted for the signal provided

by the Tektronix current probe to produce the second transfer function.



Number	Item
1	Zonic Input Module
2	Crown Com-Tech 400 Amplifier
3	Piezoelectronics (PCB) SN 8549 Accelerometer
4	Tektronix P6021 Current Probe
5	Terfenol-D Actuator

Figure 3.2: Experimental WCA Setup for Obtaining the Stroke to Current Transfer Function

The electrical impedance of the actuator and of an actuator coil are obtained from an HP 4194A Impedance/Gain-Phase Analyzer. This meter is capable of taking impedance and gain/phase measurements and displaying the data on a color CRT. This HP analyzer is



capable of measurements in the 100 to 40 MHz frequency range, can display two separate sets of data simultaneously, and can perform various analysis on collected data.

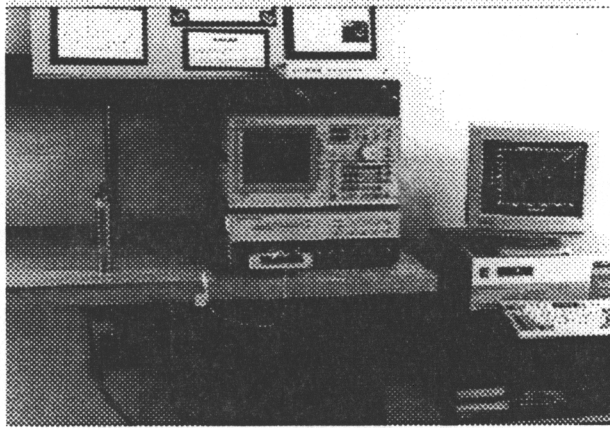


Figure 3.3: HP 4194A Impedance Analyzer Using a 486 Computer for Actuator Electrical Impedance Data Acquisition

The electrical impedance data acquisition setup is completed with AD/DA boards and a 486 computer. Fig. 3.3 shows the system taking the electrical impedance data of the entire actuator while Fig. 3.4 shows the same for only the actuator coil.

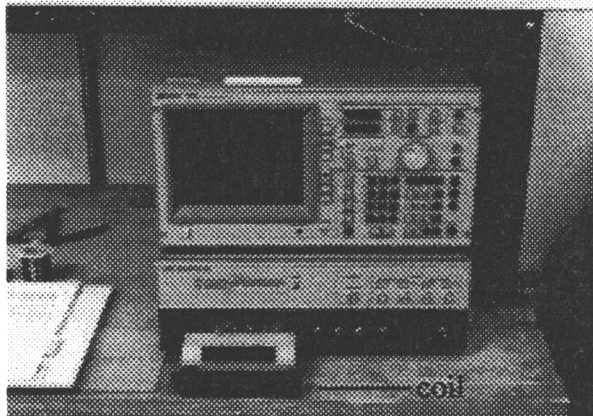


Figure 3.4: HP 4194A Impedance Analyzer Used for Coil Electrical Impedance Data Acquisition

### 3.2 Model Evaluation

The two transfer functions obtained experimentally are free-stroke to current and free-stroke to voltage at an approximate driving voltage of 10 volts pp. Changing the driving field level caused only a slight frequency shift of the first resonant frequency of the transfer function. The data taken via the WCA is in the form of acceleration and therefore had to be integrated twice to obtain the correct values. This operation is an available signal processing function performed in the WCA software. Fig. 3.5 shows the experimental free-stroke to current transfer function.

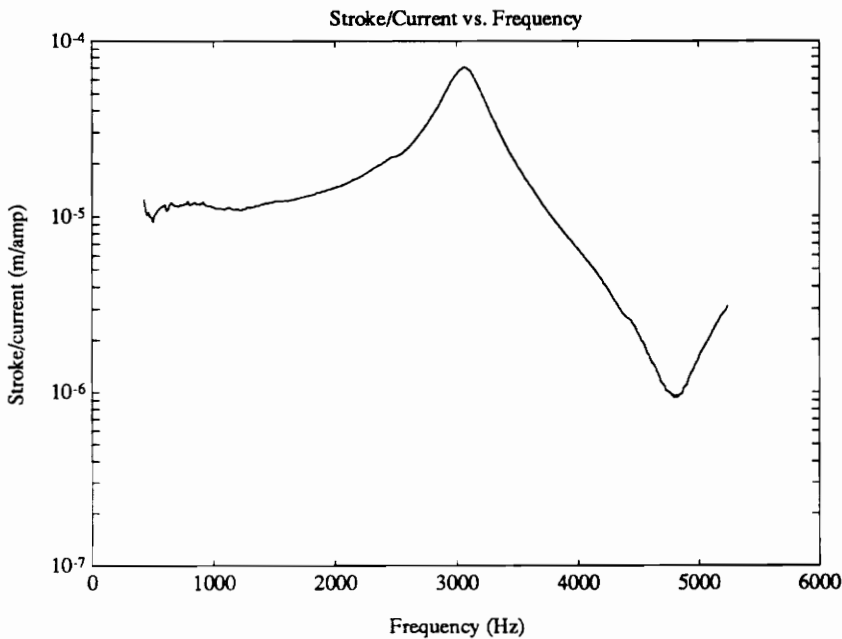


Figure 3.5: Free-stroke to Current Experimental Transfer Function  
Taken From the WCA

Because of uncertainty in the stated actuator fixture stiffness, prestress spring mass, and the output rod mass, a system identification technique is employed to determine what equivalent

mass and stiffness values are required to make the behavior model have resonance behavior matching experimental data. Also, the experimental transfer function data shown in Fig. 3.5 indicates that the actual stiffness of the fixture is much greater than modeled because the first resonance of the actuator is higher than expected. Possible sources of additional system stiffness are due to contact problems and misalignment between internal components and binding of the output rod at the top cap (Haynes, Geng, and Teter, 1993).

The goal of the system identification technique is to develop a transcendental or frequency equation for the actuator system in terms of the equivalent fixture mass and stiffness. The frequency equation is developed from the free-stroke output to current transfer function Eq. (102) shown as:

$$\frac{\bar{x}_3}{I} = dNZ_T \left[ \frac{1}{Z_T + Z_H} \right] \left[ \frac{\tan(\kappa_T l_T)}{\kappa_T l_T} \right] \quad (102)$$

The Terfenol-D rod impedance  $Z_T$  is:

$$Z_T = \frac{K_T}{j\omega} \left[ \frac{\kappa_T l_T}{\tan(\kappa_T l_T)} \right] \quad (15)$$

Substituting Eq. (15) into Eq. (102) and simplification yields:

$$\frac{\bar{x}}{I} = \frac{dNK_T}{j\omega} \left[ \frac{1}{Z_T + Z_H} \right] \quad (106)$$

The resonance of Eq. (106) is determined by the behavior of the denominator because there are no frequency dependent terms in the numerator. Therefore, the frequency equation is:

$$j\omega[Z_T + Z_H] = 0 \quad (107)$$

The lumped impedance  $Z_H$  for the free actuator Eq. (53) is the combination of fixture impedance and free rod impedance (mass) shown as:

$$Z_H = Z_F + Z_{RM} \quad (53)$$

The above expression Eq. (53) contains impedance terms for the equivalent fixture stiffness, spring mass, and rod mass. These lumped impedance terms are all in parallel and are thus combined into two terms describing a total equivalent stiffness and mass:

$$Z_H = Z_{KEQ} + Z_{MEQ} \quad (108)$$

Recalling the definitions for lumped stiffness and mass impedances, Eq. (108) becomes:

$$Z_H = j\omega m_{eq} - j \frac{K_{eq}}{\omega} \quad (109)$$

where:  $m_{eq}$  is the equivalent mass or sum of the spring and rod masses  
 $K_{eq}$  is the equivalent fixture stiffness

Plugging Eq. (109) and Eq. (15) into the frequency equation Eq. (107) and simplification produces:

$$K_T \left[ \frac{\kappa_T l_T}{\tan(\kappa_T l_T)} \right] - \omega^2 m_{eq} + K_{eq} = 0 \quad (110)$$

Recall that  $K_T$  is the static stiffness and  $\kappa_T$  is the wave number of the Terfenol-D rod.

$$K_T = \frac{A_T \bar{Y}^H}{l_T} \quad \text{and} \quad \kappa_T = \frac{\omega}{c_T} \quad (111)$$

Plugging Eq. (111) into Eq. (110) and simplification yields:

$$A_T \bar{Y}^H \left[ \frac{\kappa_T}{\tan(\kappa_T l_T)} \right] = \omega^2 m_{eq} - K_{eq} \quad (112)$$

Rearrangement of Eq. (112) for convenience produces:

$$\frac{1}{A_T \bar{Y}^H} \left[ \frac{\tan(\kappa_T l_T)}{\kappa_T} \right] = \left[ \frac{1}{\omega^2 m_{eq} - K_{eq}} \right] \quad (113)$$

The above expression (113) is the final transcendental equation. The left-hand-side represents the resonance behavior of the Terfenol-D rod while the right-hand-side represents the resonance behavior of the equivalent actuator fixturing. A system resonance occurs when the two sides are equal or more precisely when the imaginary portions of each are opposite in sign. The manner in which the system damping was represented with material properties and stiffness with complex loss factors also affects the location of the impedance match and system resonance.

The Terfenol-D portion has resonance when  $\tan(\kappa_T l_T) = \infty$ . This occurs when:

$$\kappa_T l_T = n \frac{\pi}{2} \quad n = 1, 2, \dots$$

Therefore, the first Terfenol-D resonance occurs at:

$$\omega_1 = \frac{\pi C^H}{2l_T}$$

The fixture portion has resonance when the denominator is equal to zero and  $\omega^2 m_{eq} = K_{eq}$ .

Therefore, the first fixture resonance occurs, as expected, at:

$$\omega_1 = \sqrt{\frac{K_{eq}}{m_{eq}}}$$

An alternate development of this same transcendental equation is found in Kinsler, et al. (1982).

The mass of the spring and rod are known to a good degree of accuracy. The actual stiffness of the system, however, is not. Therefore, a solution of the transcendental equation Eq. (113) at the first experimental system resonance will yield the actual fixture stiffness. This first resonance is found from Fig. 3.5 to occur approximately at 3100 Hz. The system identification development is based on the free-stroke to current transfer function shown in experimental form in Fig. 3.5 because of the simplicity of the associated theoretical

expression. The theoretical free-stroke to voltage transfer function shown in experimental form in Fig. 3.6 produces a frequency equation that is difficult to manipulate and therefore is not used. This difficulty results from the presence of the actuator electrical impedance in the denominator of the expression. Despite the complexity of the second transfer function, there exists only a slight variation in the location of the first natural frequency in each of the transfer function behaviors.

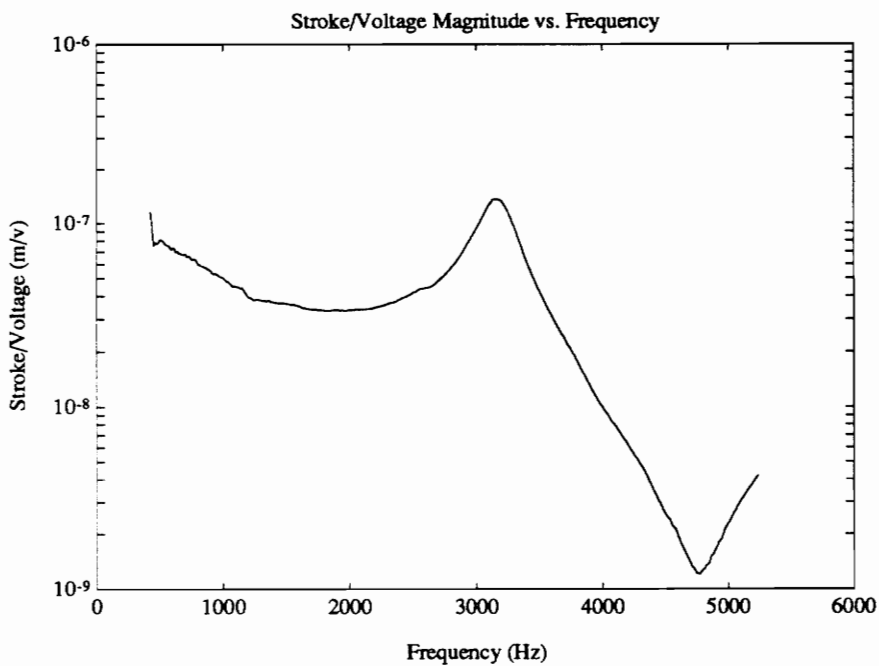


Figure 3.6: Free-stroke to Voltage Experimental Transfer Function  
Taken From the WCA

The fixture stiffness identification is performed by the Mathematica program found in Appendix B. As expected, the equivalent system stiffness is much larger. In fact, the identification technique determined that the equivalent stiffness has to be 88 times that of the modeled stiffness in order for the first resonance of the system to occur at such a high

frequency. The Terfenol-D rod alone has a first natural frequency at 2400 Hz. The modeled fixture has a first resonance at 355 Hz. The combination of these two subsystems would produce a fundamental system frequency in the range between the values of 355 and 2400 Hz. However, the experimental data shows a fundamental frequency around 3100 Hz. Therefore, the actual stiffness of the fixturing has to be much larger than the modeled approximation.

Using the adjusted equivalent fixture stiffness, the experimental and theoretical free-stroke to voltage transfer functions are correlated as shown in Fig. 3.7. All final actuator parameters are shown in Tables 3.1 and 3.2.

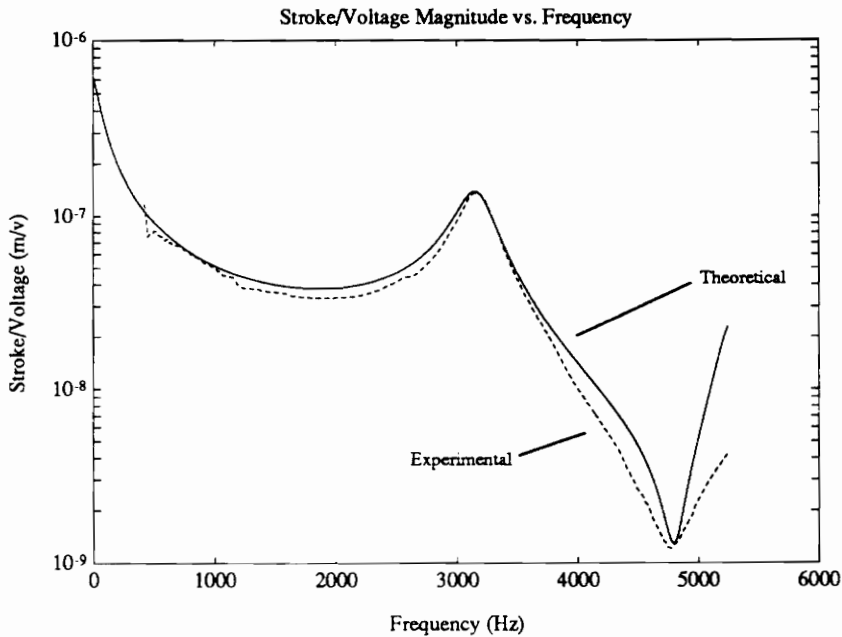


Figure 3.7: Correlated Free-Stroke to Voltage Transfer Function for the Terfenol-D Actuator



Shown in Tables 3.1 and 3.2 are the final mechanical and electrical parameters used to produce the theoretical to experimental correlation shown in Fig. 3.7.

<u>Term</u>	<u>Symbol</u>	<u>Value</u>	<u>Units</u>
<u>Fixture</u>			
spring stiffness	$K_S$	3.5 e+5	N/m
spring damping		10.0	%
casing stiffness	$K_C$	3.36 e+8	N/m
casing damping		0.5	%
spring mass	$m_S$	0.001	kg
stiffness scaling		88	
total stiffness	$K_{EQ}$	3.08 e+7	N/m
<u>Terfenol-D Rod</u>			
length	$l_T$	0.1524	m
cross-sectional area	$A_T$	3.1669 e-5	m <sup>2</sup>
density	$\rho$	9.25 e+3	kg/m <sup>3</sup>
Youngs Modulus	$\bar{Y}^H$	1.99 e+9	N/m <sup>2</sup>
damping	$\eta$	3.0	%
stiffness	$K_T$	4.11 e+5	N/m
speed of sound (H = 0)	$C^H$	1467	m/sec

Table 3.1: Actuator Parameters Used for Theoretical to Experimental Correlation

<b><u>Term</u></b>	<b><u>Symbol</u></b>	<b><u>Value</u></b>	<b><u>Units</u></b>
<b><u>Rod</u></b>			
damping		0.1	%
cross-sectional area	$A_R$	3.1669 e-5	$m^2$
length	$l_R$	0.05715	$m$
Youngs Modulus	$Y_R$	207 e+9	$N/m^2$
density	$\rho_R$	7801.35	$kg/m^3$
mass	$m_R$	0.069	$kg$
stiffness	$K_R$	1.14 e+8	$N/m$
speed of sound	$C_R$	5151	$m/sec$
<b><u>Electrical</u></b>			
"d" constant	$d$	1.5 e-8	$m/A$
permeability	$\mu$	1.8 e-5	$Tm/A$
inductive loss factor	$\eta_E$	0.33	
number of coil turns	$N$	2000	
dc coil resistance		6.0	$\Omega$

Table 3.2: Actuator Parameters Used for Theoretical to Experimental Correlation

Figs. 3.8 and 3.9 show the real and imaginary portions of the coil electrical impedance respectively. These plots are used to approximate the effective free-permeability of the actuator coil and the inductive loss factor as shown in section 2.10. This provides insight into the non-linear electrical coil behavior without the presence of the ferromagnetic Terfenol-D material and allows for baseline adjustment of the electrical portion of the actuator model. With this adjustment the theoretical and experimental electrical impedances have improved correlation and the effects of the electro-magneto-mechanical interaction can be better seen. All of the actuator mechanical and electrical properties and simulation codes are found in the computer code section found in Appendix B.

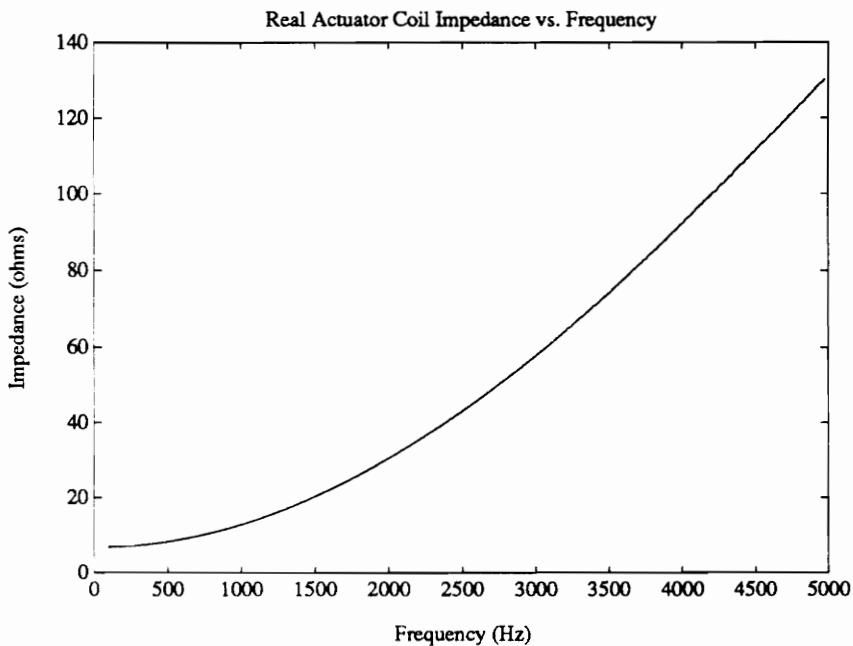


Figure 3.8: The Experimental Real Electrical Impedance of the Actuator Coil Taken With the HP 4194A Analyzer

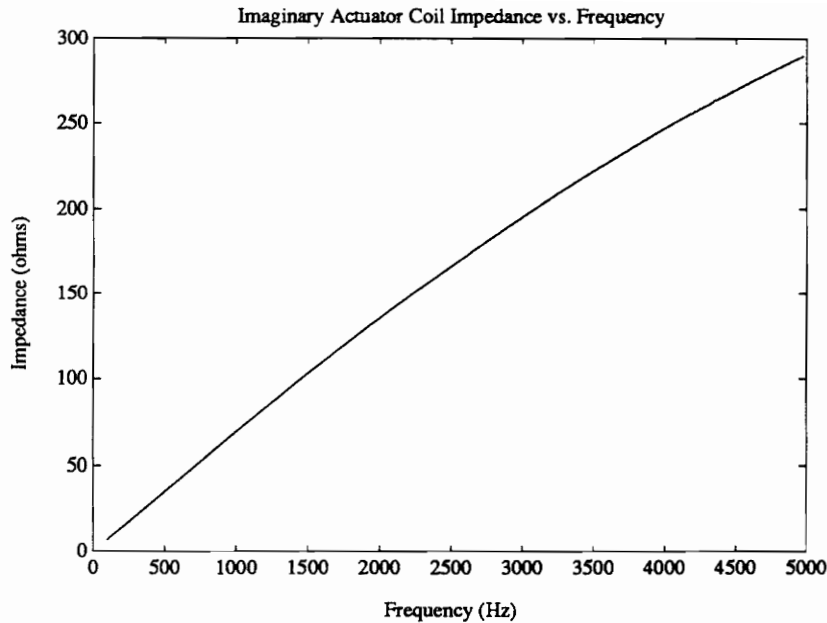


Figure 3.9: The Experimental Imaginary Electrical Impedance of the Actuator Coil Taken With the HP 4194A Analyzer

The real and imaginary portions of the actuator electrical impedance are shown in Figs. 3.10 and 3.11. These plots display the effect of the electro-magneto-mechanical interaction in which the actuator system mechanical resonance also creates an electrical resonance. However, the magnitudes of the resonant peaks and the general shape of the real and imaginary portions of the electrical impedance do not correlate well. Also, the resonant peak displayed as a result of the electro-magneto-mechanical interaction does not occur at exactly the same frequency as the system resonance as the electrical impedance model predicted. The significance of these differences is investigated by comparing a completely theoretical free-stroke to voltage transfer function to one using the experimental electrical impedance. This comparison, seen in Fig. 3.12, shows that the uncorrelated electrical behavior causes a slight difference in the off-resonance transfer function before the first resonance and very little

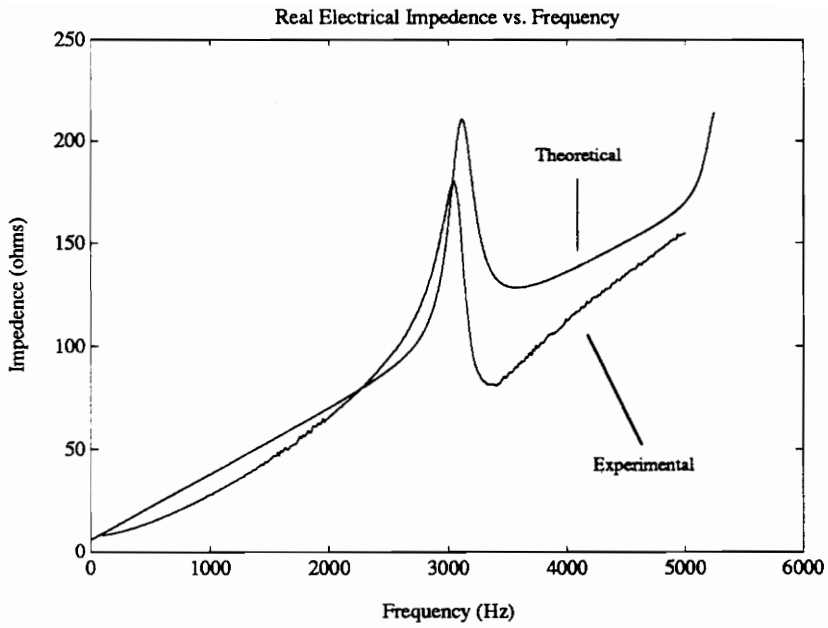


Figure 3.10: The Correlated Real Electrical Impedance of the Terfenol-D Actuator Taken With the HP 4194A Analyzer

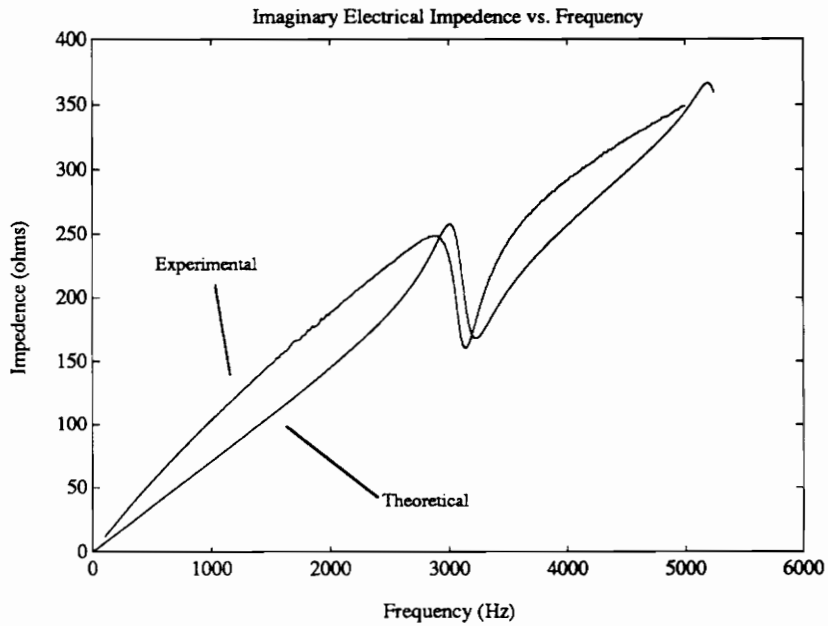


Figure 3.11: The Correlated Imaginary Electrical Impedance of the Terfenol-D Actuator Taken With the HP 4194A Analyzer

difference past the resonance. The location of the resonance in both the transfer functions is nearly the same but the peak values are not. This is related to the differences between the peak values of the real electrical impedance shown in Fig. 3.10. The peak value of the theoretical model could be better correlated to the experimental by adjusting the "d" constant. However, the stoichiometry of the Terfenol-D material in the actuator is not known by Intelligent Automation, Inc. from whom the actuator was borrowed. Therefore, no significant adjustment of this value can be justified. However, parametric studies showed that increasing the "d" constant not only improves the peak height correlation, but also brings the

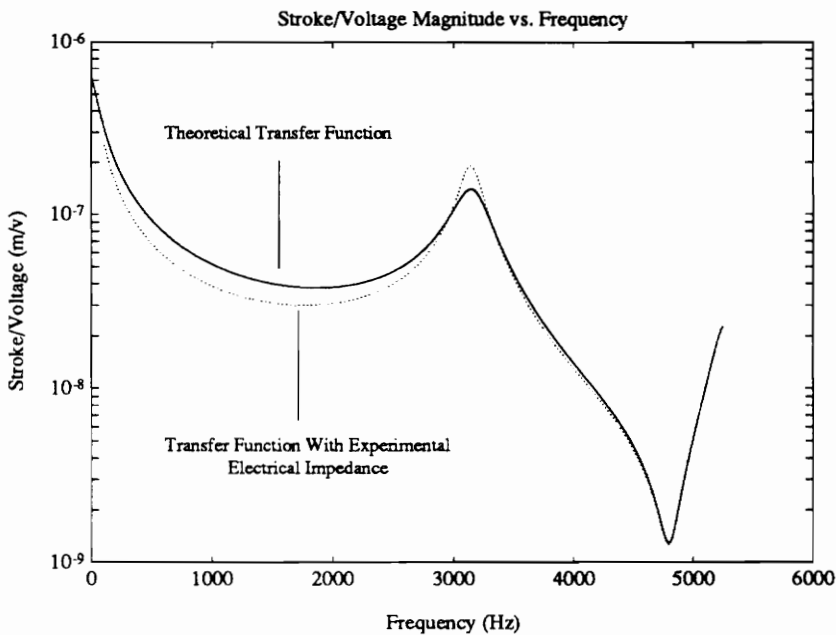


Figure 3.12: Free-stroke to Voltage Transfer Function Comparison Using Theoretical and Experimental Electrical Impedances

fundamental frequency values of the experimental and theoretical impedances closer together. This is a result of the structure of the electrical impedance expression in which

modification of the "d" constant changes the frequency spacing between the resonant peaks. Also, the slight mismatch in the resonant frequency values can be altered with small adjustments to the equivalent fixture stiffness. This, however, causes a slight misalignment in the peaks of the free-stroke to voltage transfer function. In other words, a trade-off exists. This effect could be related to the frequency dependency of the Terfenol-D Young's Modulus which affects the location and spacing of the resonances and anti-resonances. This frequency dependence is not included as a part of the behavior model. Further discussion of this is found in the conclusion section of this thesis.

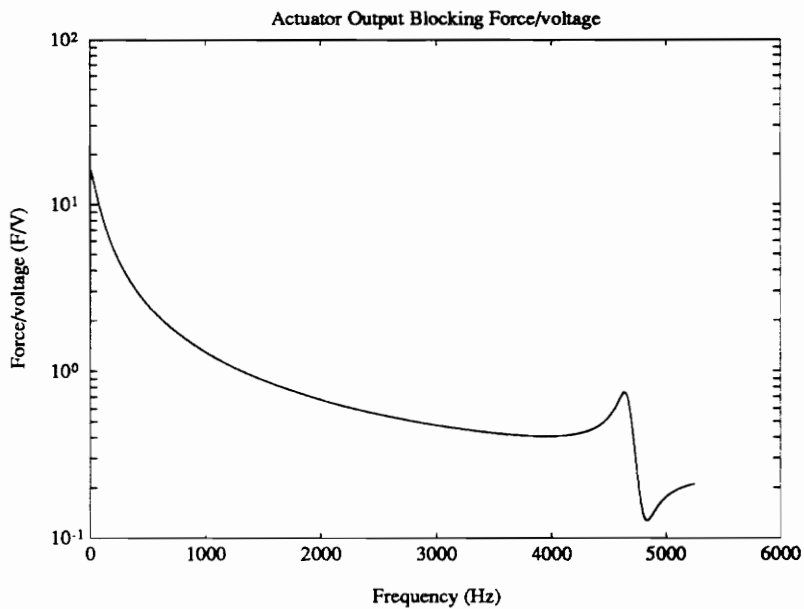


Figure 3.13: Theoretical Actuator Blocking Force to Voltage Transfer Function

The theoretical blocking force to voltage capability of the Terfenol-D actuator is shown in Fig. 3.13. No experimental verification of this result is performed because of experienced difficulties in developing adequate boundary conditions for the actuator. The Terfenol-D actuator displays unusual behavior when experiencing large externally applied impedances. This may be a result of alignment problems or spacing problems inside the actuator. More

discussion of these experimental difficulties is presented in the future work section of this thesis.

An analysis of the mechanism of force transfer inside the actuator begins with the force applied to the output shaft by the activated Terfenol-D rod. As seen in Fig. 3.14, the output force from the Terfenol-D ( $F_1$ ) is shared between the actuator fixture impedance  $Z_F$  and

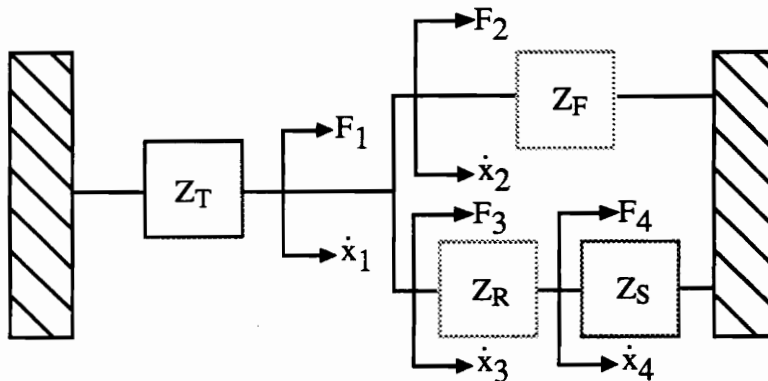


Figure 3.14: Complete Actuator Impedance Configuration

output rod impedance  $Z_R$ . The force to voltage seen by the rod impedance is designated as  $F_3$  and is shown in Fig. 3.15. The difference in magnitude between this relationship and the blocking force is a result of slight inertial losses due to rod mass. The resonant peak seen in the plots of rod input force and actuator blocking force occur at the system resonance for that configuration. At that frequency the output force is a maximum because of the dynamics associated with the large output stroke.

Another important aspect of the force transfer inside the actuator involves the dynamic stress developed in the Terfenol-D rod. The level of developed stress is significant in two respects. The first involves the stress dependency of many material properties including the "d"



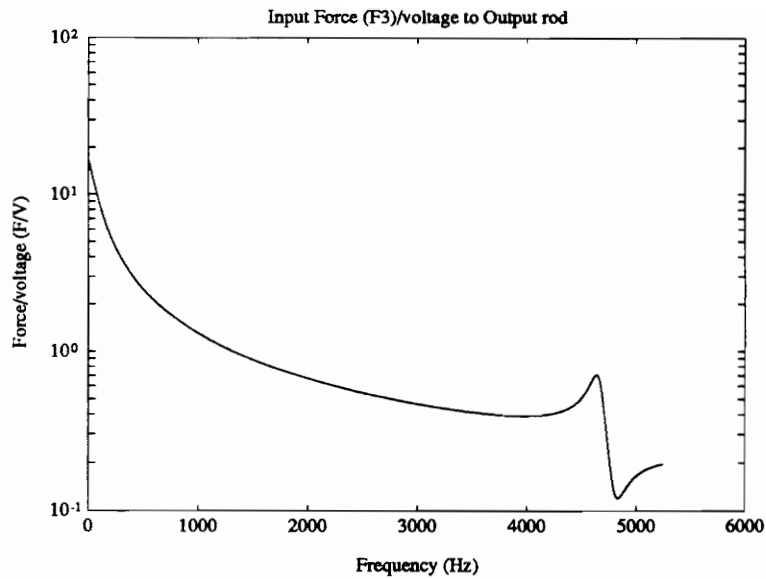


Figure 3.15: Rod Input Force (F3) to Voltage Transfer Function

constant which relates applied field to induced strain. The literature presents strain vs. field plots for constant levels of stress and uses the slope of the linear portion of these relationships as the basis for establishing a region of operation. However, if the developed dynamic stress is significant in comparison to the applied prestress, the Terfenol-D will move around in a region of strain vs. field curves.

The second important ramification of the dynamic stress analysis involves the lack of material strength in the tensile direction. Inadequate prestress could allow for dynamic operation in the tensile range which could result in material failure. Fig. 3.16 shows the magnitude of dynamic Terfenol-D stress to applied voltage for both the free and blocked actuator boundary conditions. This stress is that which develops in the material in addition to the applied prestress. Notice that for both boundary conditions the highest levels of stress occur at the Terfenol-D resonance near 2400 Hz and the lowest levels of stress at the first Terfenol-D anti-resonance. At resonance the material is both dynamically "soft" and stroking

at a maximum level which induces high stress levels. At the anti-resonance point the material is very dynamically stiff and stroking at a minimum level which results in low stress levels.

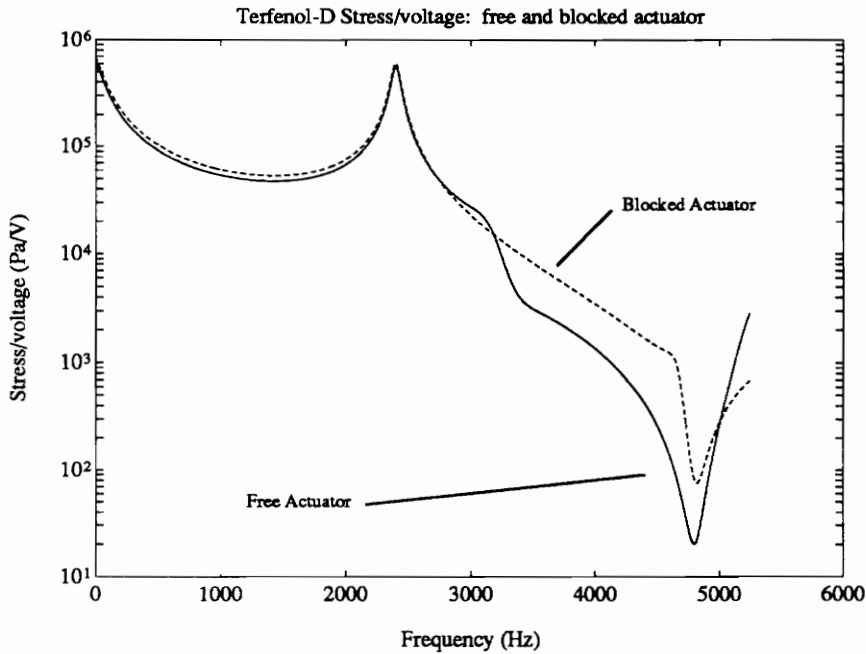


Figure 3.16: The Dynamic Stress Magnitude Developed in the Terfenol-D Rod

The stress to voltage curves for the two extreme boundary conditions have very similar values up to the system resonance near 3100 Hz. This is a result of the low stiffness of the Terfenol-D rod in comparison to the fixture stiffness. The Terfenol-D rod stiffness is calculated as  $4.16 \times 10^6$  N/m. The equivalent fixture stiffness is equal to the initial spring stiffness used multiplied by the required scaling factor of 88 which is produced by the system identification procedure as described previously in this chapter. The scaling factor is included because the fixture stiffness is a result of the casing and spring stiffness in series. Because the casing stiffness is three orders of magnitude larger than that of the spring, the equivalent stiffness seen by the Terfenol-D rod is simply that of the spring constant with the

included scaling factor. This is nearly equivalent to assuming the casing stiffness is infinite. A static analysis of the force and displacement relationship between the activated Terfenol-D rod and fixture shows that the stress to applied voltage that would develop in the material with a dc applied field and a free actuator boundary condition is:

$$\frac{T}{V} = - \frac{dN}{A_T Z_{EF}} \left[ \frac{K_T K_S}{K_T + K_S} \right]$$

where:  $d$  is the "d" constant  
 $N$  is the number of coil turns  
 $A_T$  is the cross-sectional area of the Terfenol-D rod  
 $Z_{EF}$  is the free actuator electrical impedance  
 $K_S$  is the spring stiffness  
 $K_T$  is the Terfenol-D stiffness

Substituting into this expression yields the static Terfenol-D stress to voltage level approximately as  $6.06 \times 10^5$  N/V which matches the static value shown in Fig. 3.16. In the above expression, the stiffness terms in the bracket simplify to a value near that of the Terfenol-D stiffness because the spring is much stiffer. For the blocked actuator boundary, the same situation exists except that the boundary condition instead of the spring is the member which restricts the expansion of the Terfenol-D. The low Terfenol-D stiffness value creates a situation at low frequencies where the fixture presents a boundary condition that is close to blocked. That is why the stress to voltage levels for the free and blocked actuator boundary conditions look very similar up to the system resonance. Fig. 3.16 displays the relative magnitude of stress developed in the Terfenol-D rod but provides no information concerning the relationship between the dynamic stress and compressive prestress. Shown

in Fig. 3.17 is the complete stress level in the Terfenol-D rod at a representative driving level of 15 volts pp. The negative stress signifies compression. Notice that at 2400 Hz, the first resonance of the Terfenol-D, the material is experiencing a significant decrease in the level of compressive stress. The total state of stress again approaches the prestress level at the first system resonance near 3100 Hz.

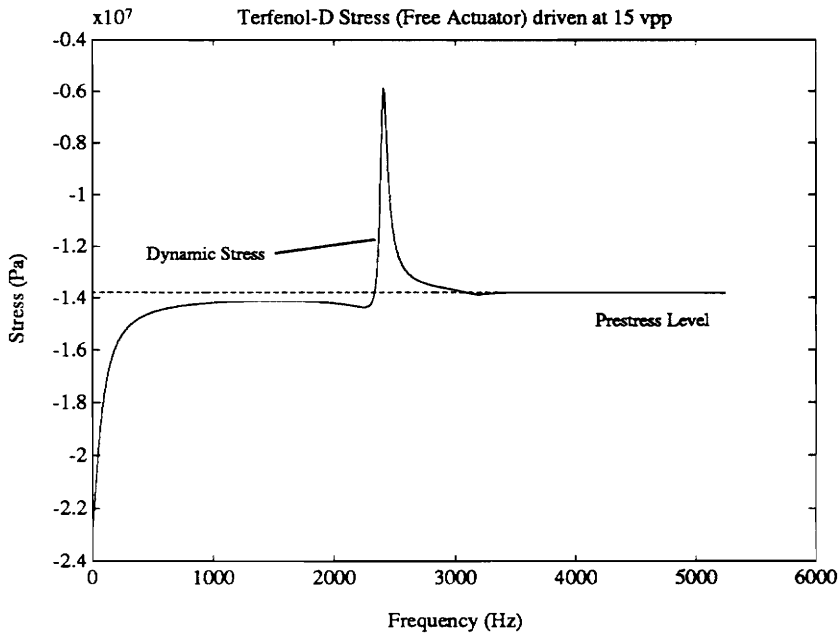


Figure 3.17: The Total State of Stress in the Terfenol-D Rod

Other important analysis of the actuator include investigation of the energy ratio of the transducer and the level of dissipative power consumption. The power consumption of the Terfenol-D actuator, as developed in Chapter 2, is calculated using the following expression:

$$P_D = \frac{V^2}{2} \text{Re}[Y_E]$$

where:  $V$  is the applied voltage

$Y_E$  is the actuator electrical admittance (inverse of impedance)

Fig. 3.18 shows the dissipative power consumption for both blocked and free actuator boundary conditions at a 15 volt pp driving voltage. The peak dissipation values of each plot correspond to the system resonances for the respective actuator boundary conditions. The resonant peak for the blocked actuator shows a significant reduction in peak magnitude in comparison to the free actuator. This is caused by a decrease in the electro-magneto-mechanical interaction of the device as a result of the decreased dynamics when the actuator output is blocked. Therefore, when the actuator is blocked the electrical impedance of the coil is nearly that of only the inductor without the presence of any mechanical interaction.

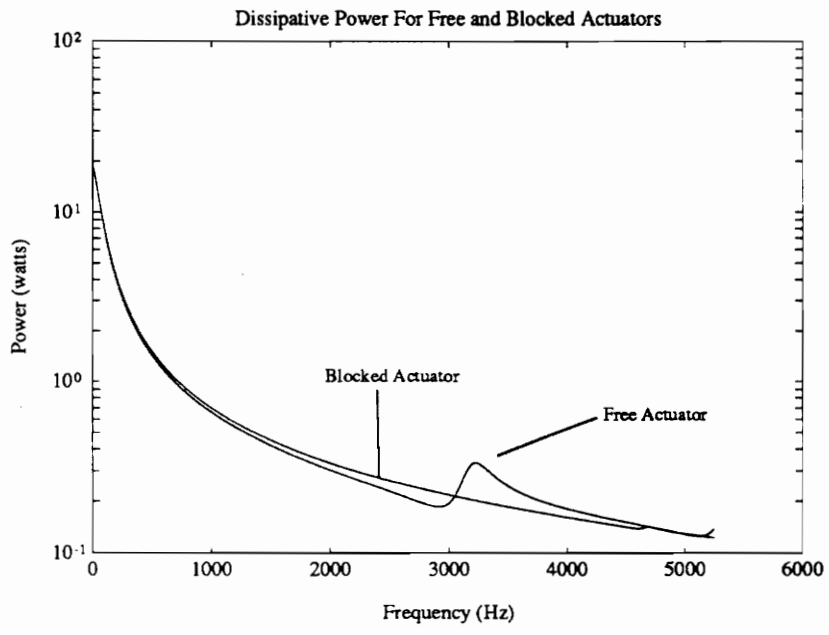


Figure 3.18: Terfenol-D Actuator Dissipative Power Consumption for Blocked and Free Boundary Conditions

The energy ratios presented in Chapter 1 are compared in Fig. 3.19 below. Notice that the energy ratio dependent only on non-varying material properties does not show the frequency dependence of transducer efficiency. However, if the variation of material properties as a result of changing stress and drive levels were included, the accuracy of this energy ratio could improve. Fig. 3.19 also shows the energy ratio for the free actuator with the maximum efficiency near the first actuator resonance. As mentioned in Chapter 2, the energy ratio given by the canonical equations applies to the mechanical dual transduction form developed in this thesis and any other arrangement of the transduction representation.

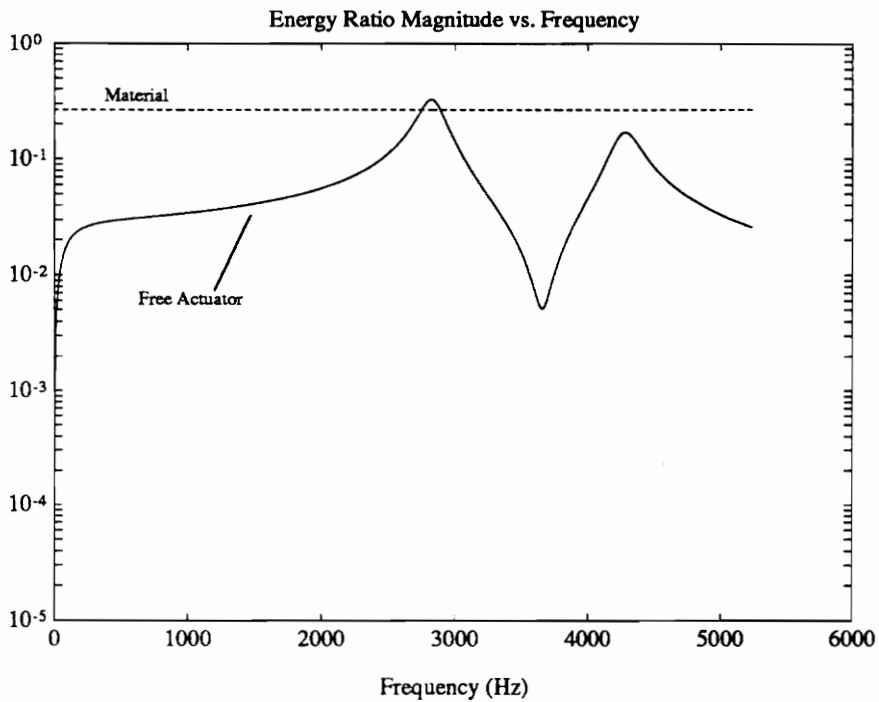


Figure 3.19: Transducer Energy Ratios as a Function of Material Properties and for the Free Terfenol-D Actuator

### 3.3 Actuator Time-Domain Behavior and Non-linearities

The experimental transfer functions shown in Figs. 3.5 and 3.6 exhibit noisy or possibly non-linear actuator behavior at low driving voltage frequencies. Investigation of this behavior is performed by gathering time domain data at low frequencies and near the first resonance using the WCA.

At low frequency driving voltages, both the actuator coil current and acceleration output are highly non-linear. As the frequency of the sinusoidal driving voltage is increased, the behavior of the actuator improves with nearly linear acceleration behavior reached near 600 Hz. A portion of this non-linear time domain behavior is presented in Figs. 3.20-3.23. Additional data and frequency spectra are found in Appendix A.

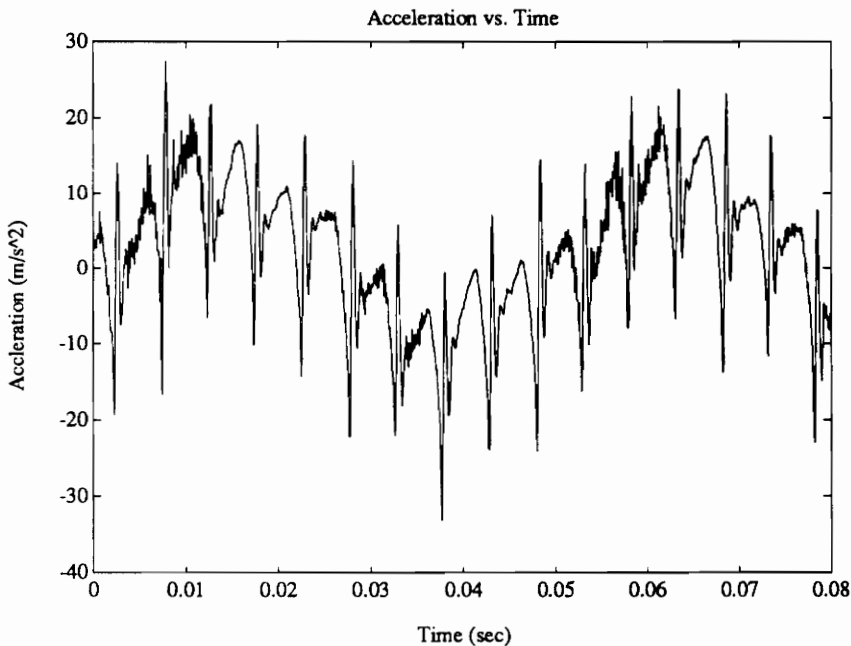


Figure 3.20: Actuator Non-linear Output Acceleration With a 20 Hz Driving Voltage

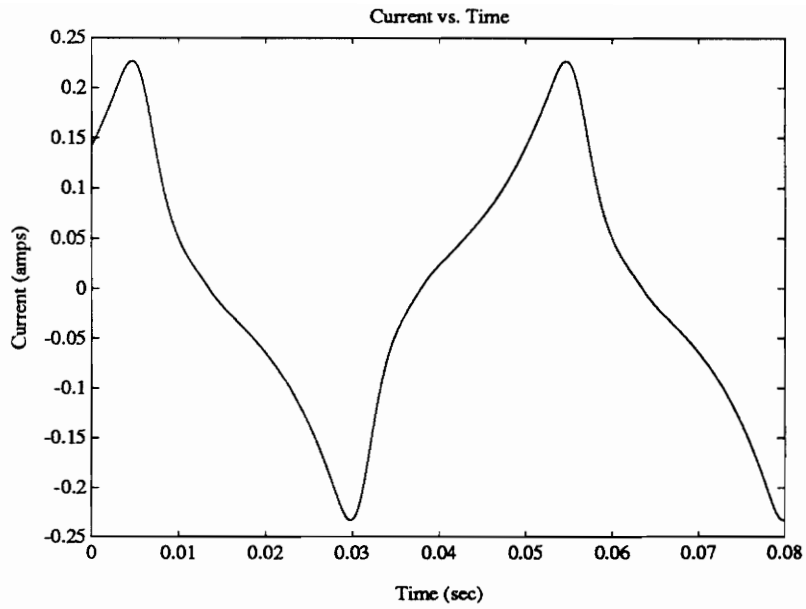


Figure 3.21: Actuator Non-linear Coil Current With a 20 Hz Driving Voltage

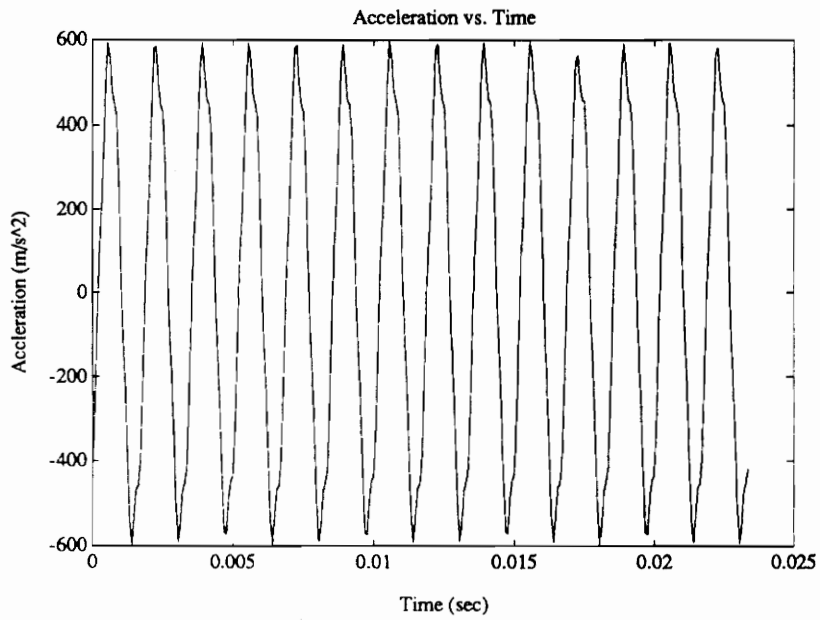


Figure 3.22: Actuator Output Acceleration With a 600 Hz Driving Voltage



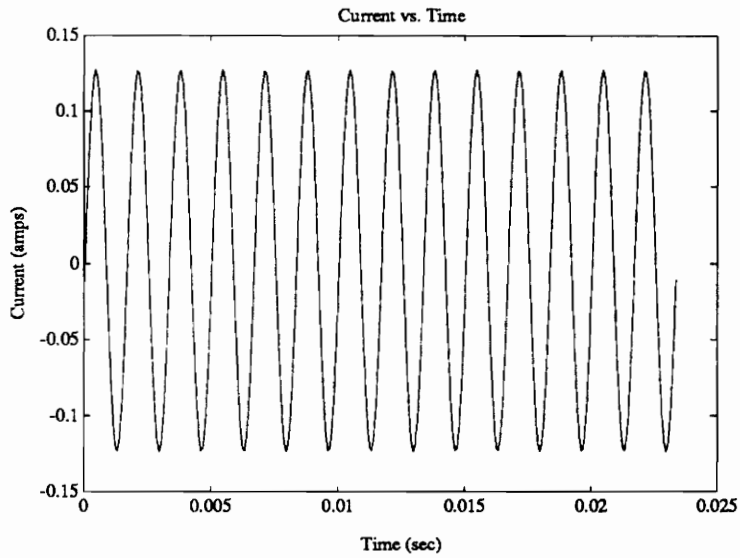


Figure 3.23: Actuator Coil Current With a 600 Hz Driving Voltage

The time domain data taken near resonance shows unusual actuator behavior in the 3000-3700 frequency range. This includes the resonant frequency at around 3100 Hz. The actuator acceleration in this band shown in Figs. 3.24-3.27 seem to develop an extra, high-frequency

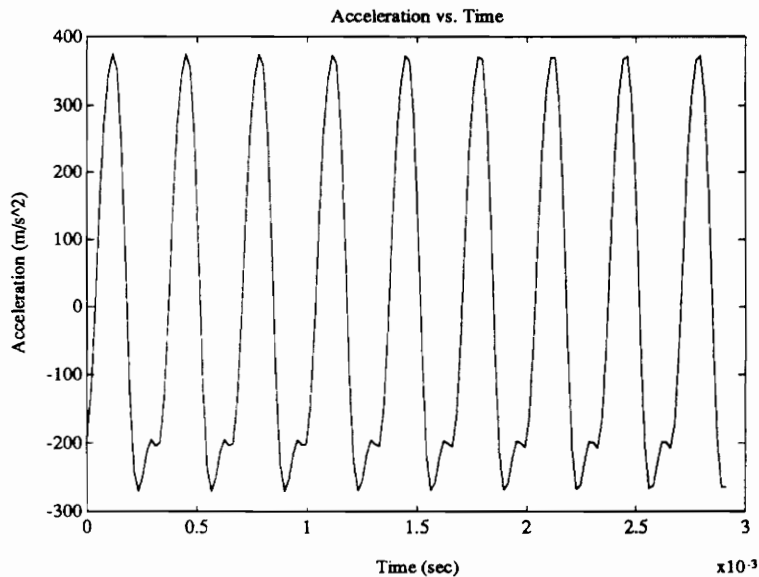


Figure 3.24: Actuator Output Acceleration With a 3000 Hz Driving Voltage

harmonic and exhibits attenuation of the portion of the signal above the time axis. Unlike at low frequencies, the current waveform remains linear throughout the frequency band near resonance.

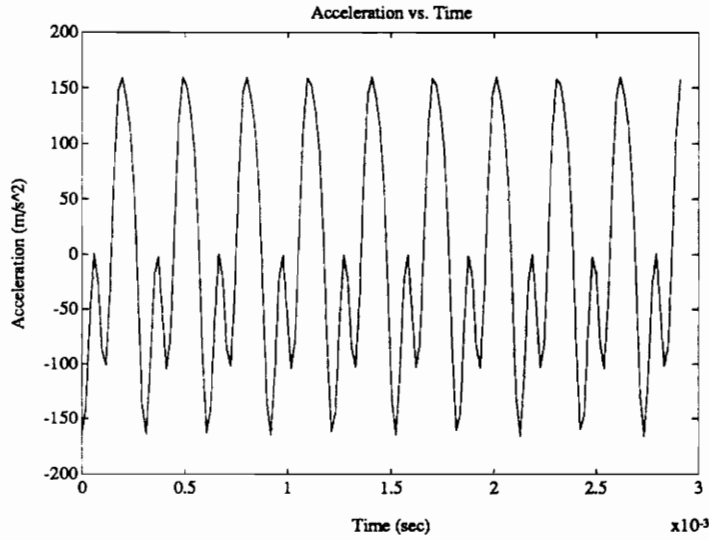


Figure 3.25: Actuator Output Acceleration With a 3300 Hz Driving Voltage

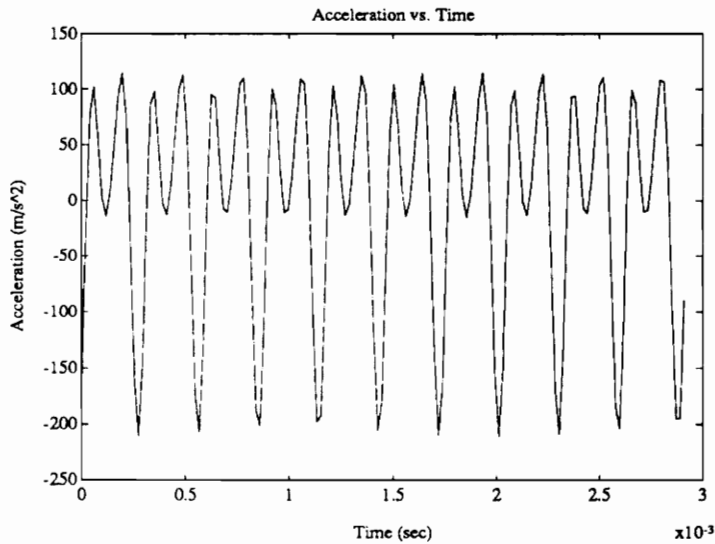


Figure 3.26: Actuator Output Acceleration With a 3450 Hz Driving Voltage

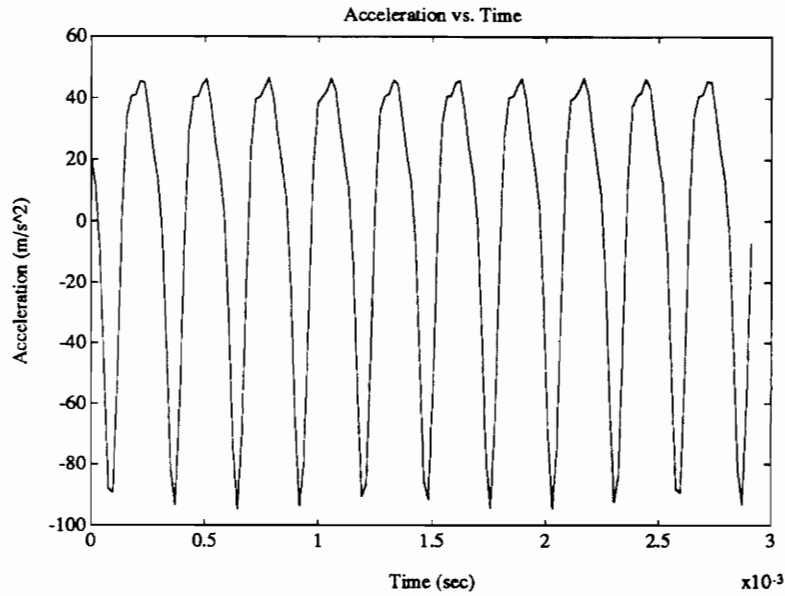


Figure 3.27: Actuator Output Acceleration With a 3600 Hz Driving Voltage

Several explanations are offered as explanations for this non-linear behavior. A common problem with Terfenol-D as a material, especially in the developmental stages (Moffett, et al., 1991; Goodfriend, Shoop, and McMasters, 1992), is the inability to obtain uniform material properties. In other words, one portion of the sample will exhibit a certain strain behavior in the presence of an applied field that is different from other regions in the sample. This creates non-uniform strain and stress distributions in the sample. Because the behavior characteristics of Terfenol-D are sensitive to stress and drive levels, this non-uniformity would cause non-linear behavior for certain levels of applied magnetic field. Another related problem encountered in experiment is the inability to apply a uniform magnetic field to the Terfenol-D sample. This also causes unusual strain and stress variations within the sample and non-linear behavior.

An additional and previously mentioned source of electrical non-linearity in the actuator

exists in the coil itself. Fig. 3.8 and Fig. 3.9 show the real and imaginary electrical impedances of the coil itself. An ideal coil would have a resistance and would produce a horizontal line in the real impedance plot and an inductance with a line having constant slope in the imaginary impedance plot. However, the real electrical impedance of the coil shows a large amount of curvature in comparison to the ideal horizontal line. This indicates a large inductive and possibility capacitive loss in the coil. The coil model is based on an ideal inductor with an added dc resistance. However, the actuator coil has multiple layers of windings where inductance and capacitance exists not only between parallel windings, but also between the layers themselves with the non-conductive wire coating serving as the dielectric material.

### **3.5 Concluding Remarks**

The experimental analysis of the modeled Terfenol-D actuator is detailed with a complete description of the equipment used, presentation of measured data, system identification, model correlation, and discussion.

The presented experimental data include free-stroke to current and free-stroke to voltage transfer functions, free electrical impedance of the actuator, electrical impedance of the actuator coil alone, and time domain acceleration and current wave forms. The first resonant peak of the free-stroke to current transfer function is used for a developed system identification process in order to determine the actual mechanical stiffness of the prestress fixture. The second transfer function, free-stroke to voltage, is not used because of the complexity of the corresponding theoretical expression as a result of electro-magneto-mechanical coupling.

The unknown electrical properties of the actuator are obtained by baseline adjusting the values of free permeability, inductive loss factor, and dc resistance in order to improve the correlation of the theoretical model of electrical impedance. To further improve the theoretical to experimental correlation, the unknown mechanical damping terms are adjusted within the reasonable range of 1-3 % for the Terfenol-D rod, 5-10 % for the viscoelastic prestress fixture spring, and 0-0.5 % for the actuator casing. All of the electrical and mechanical actuator properties are in the computer code section found in Appendix B.

With all of the actuator mechanical and electrical properties identified, the free-stroke to voltage and free electrical impedance data are correlated with theoretical expressions. The free-stroke to voltage correlation is shown again in Fig 3.28 on the following page. Excellent correlation is seen in the frequency range between 500 Hz and approximately 4800 Hz. At frequencies below 500 Hz. the actuator exhibits highly non-linear acceleration and current wave forms as displayed in subsection 3.3 of this chapter and in Appendix A.

The real and imaginary electrical impedance plots do not show the same quality of correlation as the previously mentioned transfer function shows. The first resonance in the electrical impedance, caused by mechanical interaction, does not match the frequency predicted by the model by approximately 50 Hz. The causes of this mismatch are related to lack of knowledge of the actuator "d" constant, the frequency dependence of the Youngs Modulus of Terfenol-D, and coil electric non-linearity. Further investigation into the degree in which this mismatch in resonant behavior and curve alignment affects the free-stroke to voltage transfer function shows that a slight variation occurs off resonance and at the peak value of the first fundamental frequency. At frequencies great than resonance the difference between theoretical and experimental electrical impedances does not alter the transfer function behavior as seen in Fig. 3.12.

The theoretical frequency dependent blocking force is also presented but not verified because of experienced difficulties in creating adequate boundary conditions and non-linear actuator behavior when experiencing large external impedances. The blocking force to voltage transfer function has a maximum value at the system resonance.

The level of dynamic stress in the Terfenol-D is shown to vary significantly from the applied prestress at the Terfenol-D rod resonance. The stress developed in the Terfenol-D rod is also shown for blocked and free actuator configurations where little difference exists as a result of the low Terfenol-D stiffness in comparison to the prestress spring for the free actuator and the fixed boundary for the blocked actuator. In both cases the activated material sees a nearly blocked boundary condition because of the significant difference in material stiffness in comparison with boundary conditions.

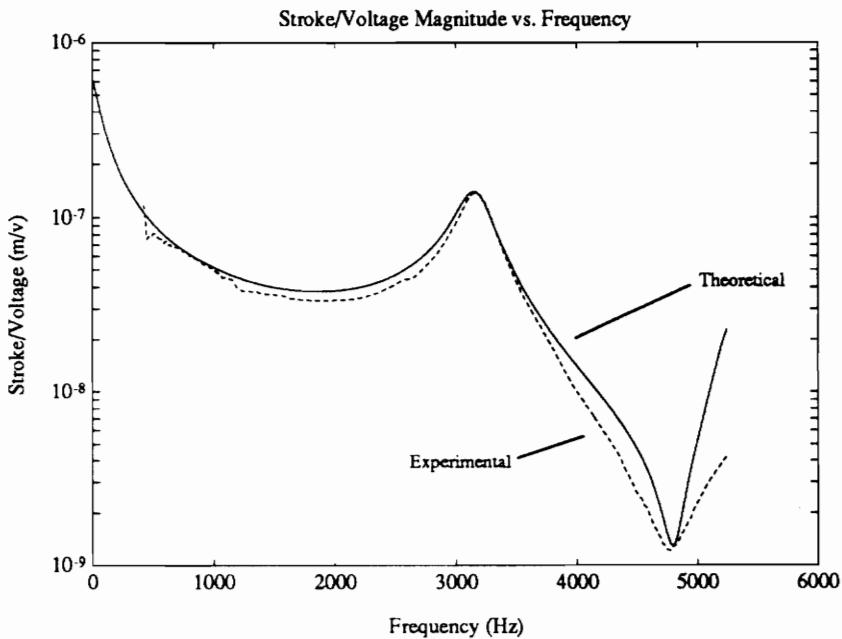


Figure 3.28: Correlated Free-Stroke to Voltage Transfer Function for the Terfenol-D Actuator

The dissipative power consumption of the actuator is also presented for blocked and free configurations. The power consumption for the free actuator has a peak value at the system resonance as expected. The same relationship for the blocked actuator shows a significantly smaller peak at the system resonance for the blocked boundary condition. This magnitude difference is attributed to the decrease in mechanical interaction as a result of significantly reduced internal actuator displacements and corresponding dynamics.

The energy ratio of the Terfenol-D transducer is presented for the free actuator and as a function of the Terfenol-D material properties. The boundary condition dependent ratio is derived from a two-port network configuration and canonical transduction equations as is described in Chapter 1. The comparison of the two energy ratios shows both the effects of operating conditions on transducer efficiency and the inadequacy of the material based expression.

The non-linear acceleration and current behaviors are documented for the free actuator. The actuator wave forms show significant distortion at frequencies below 250 Hz. Also, the actuator acceleration is non-linear in the 3000 to 3700 Hz frequency range.

# Chapter 4

## Hybrid Actuator/Structure Design Strategy

The modeled Terfenol-D actuator is used to drive a single degree of freedom spring-mass-damper (SMD) system in order to illustrate the basic principles involved in customizing or optimizing the performance of the entire system. This analysis includes a general study to better identify behavior trends as a function of actuator system parameters. Fig. 4.1 shows the entire system including the actuator and SMD system.

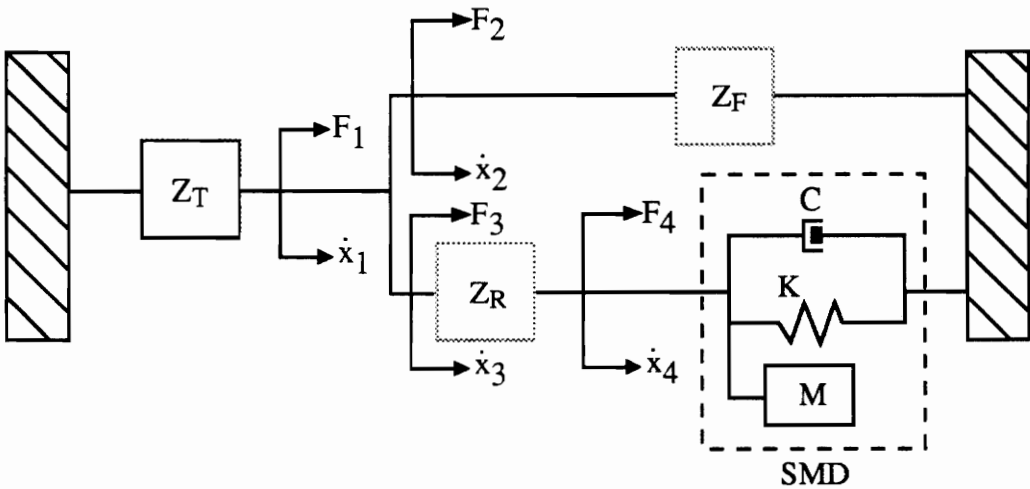


Figure 4.1: The Terfenol-D Actuator Connected With a Spring-Mass-Damper (SMD) System



The SMD system is chosen to have a natural frequency of 500 Hz with the following system values:

$$M = 2 \text{ kg}$$

$$K = 1.974 \text{ e}+7 \text{ N/m}$$

$$C = 125.66 \text{ N/m sec}^{-1}$$

The damping value is found assuming a damping ratio of  $\zeta = 0.01$  and  $C = 2\zeta m\omega_N$ .

The impedance magnitudes of the actuator and external SMD are shown in Fig. 4.2. At approximately 810 Hz the two impedance plots intersect indicating an impedance match between the actuator and driven SMD. At this frequency the entire system is at resonance and the maximum power transfer is obtained. Figure 4.3 shows the displacement of the mass

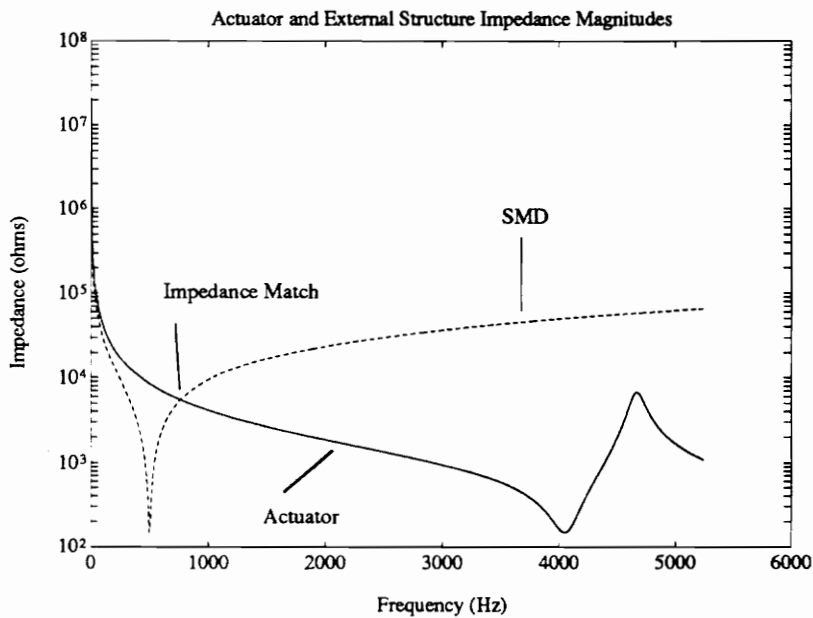


Figure 4.2: The Actuator and SMD Impedance Magnitudes Showing the Location of Impedance Match and System Resonance

with a representative driving value of 15 volts pp. Connecting the SMD to the actuator shifts the system resonance to the left in comparison with the free-stroke actuator dynamics shown in Chapter 3. This is a result of the addition of the large SMD mass impedance. The SMD stiffness is small in comparison and in parallel with the actuator stiffnesses and does not significantly affect the placement of the system resonance. In general, any increase to the total equivalent stiffness of the system increases the value of the system resonance and the addition of mass decreases the resonance value from the relationship:

$$\omega_N = \sqrt{\frac{K}{m}}$$

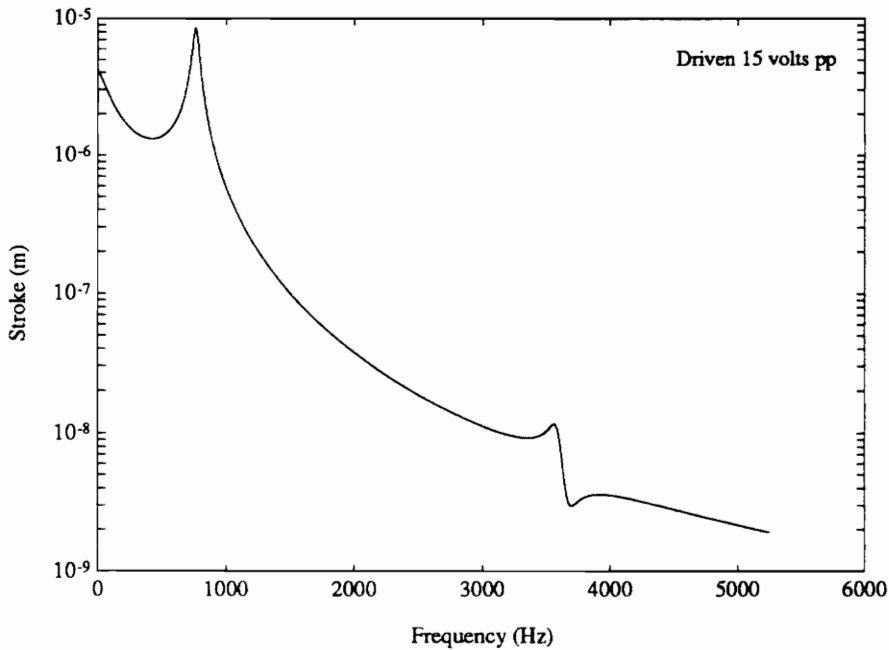


Figure 4.3: The Displacement of the Mass

The actuator/SMD interaction force is shown in Fig. 4.4. The interaction force decreases significantly at 500 Hz because little force is required to drive the SMD at resonance.

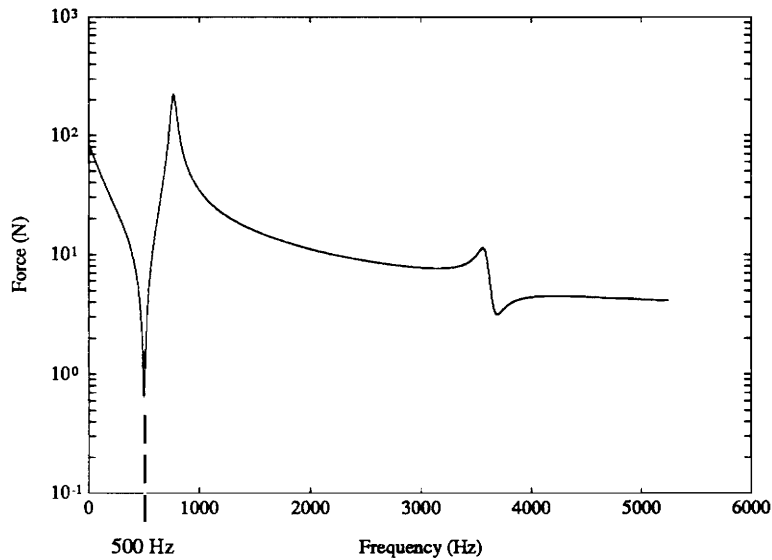


Figure 4.4: The Interaction Force Between the Actuator and SMD System

If the real system that is to be driven cannot be easily described by a single degree of freedom system like the SMD, then substitution of experimental mechanical impedance data in place of the SMD allows for simulation of the entire system and provides the means with which the basic dynamic aspects of the actuator can be tailored to provide the desired output characteristics.

An example of this process is presented as follows. For the maximum mass displacement and interaction force, the Terfenol-D actuator needs to be driven at a frequency that is close to a natural frequency of the entire system. For the actuator/SMD combination, the first resonance occurs at approximately 810 Hz as seen in Fig. 4.3. The parametric study of actuator performance presented here is performed at that resonant frequency. However, this

analysis can be performed at different frequencies if a trade-off exists between power consumption issues and maximum output capabilities. The material properties of the Terfenol-D rod, the dimensions and material type of the actuator output shaft, and the uncoupled electrical impedance (from the actuator coil alone) are assumed to remain unchanged from the actuator design modeled in this thesis. However, the dimensions of the Terfenol-D rod and the actuator fixture are altered in order to better understand how each of these parameters affects the output performance of the actuator. One important note involves the unmodeled effects of significant changes in the fixture spring. Changing the stiffness of this spring could alter the prestress level in the Terfenol-D material and thus change the "d" constant relating induced strain and applied magnetic field. Only small changes in this fixture spring stiffness are presented in this parametric study assuming that the resulting variation in "d" would be negligible and adjustment to initial spring deflection will provide no significant change in prestress levels. However, in a more detailed design analysis, the effects of this changing prestress is needed in order to accurately predict the behavior of the actuator. Also, too large of a prestress will significantly hamper the output capabilities of the material. Fig. 4.5 shows the actuator stroke capability as a function of Terfenol-D rod length. The three curves (A, B, and C) correspond to varying Terfenol-D rod cross-sectional areas:

Curve A:  $3.4 \text{ e-}6 \text{ m}^2$

Curve B:  $3.2 \text{ e-}6 \text{ m}^2$

Curve C:  $3.0 \text{ e-}6 \text{ m}^2$

The curve in the center contains a point representing the dimensions of the rod inside the modeled actuator. As shown in Fig. 4.5, an increase in the cross-sectional area of the Terfenol-D rod corresponds with increases in rod and system stiffness and the system

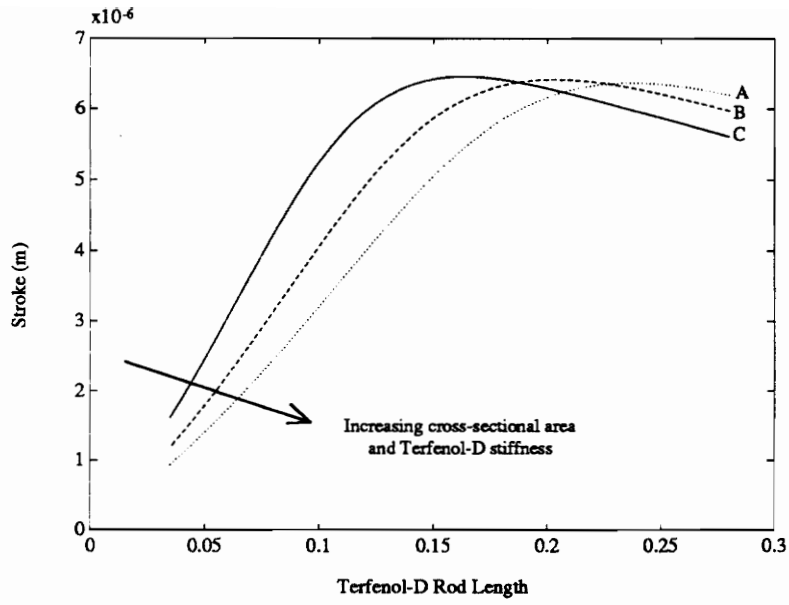


Figure 4.5: Mass Displacement as a Function of Terfenol-D Rod Length and Cross-Section

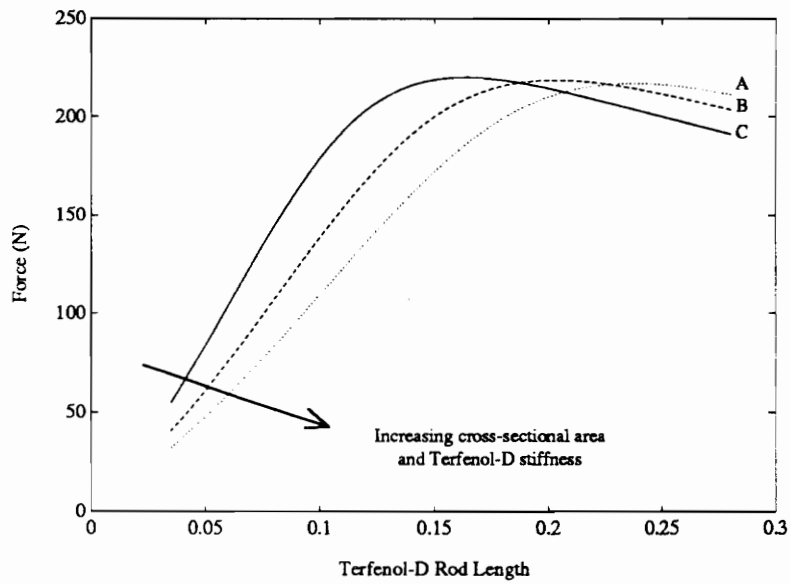


Figure 4.6: Actuator/SMD Interaction Force as a Function of Terfenol-D Rod Length and Cross-Section

resonance identified by these curves shifts to the right. This is the same trend as mentioned previously in this section. An increase in the system stiffness pushes the system resonance to a higher frequency. However, an increase in Terfenol-D rod length decreases this system stiffness and pushes the resonance to a lower frequency.

The interaction force as a function of Terfenol-D rod length is shown in Fig. 4.6 with three curves corresponding to the same cross-sectional areas as are displayed in the stroke output plot shown in Fig. 4.5. These curves allow for selection of a pair of rod dimensions that will determine the feasibility of a combined mass displacement and interaction force requirement. When designing an actuator, these output characteristics plotted as functions of the Terfenol-D dimensions should include a wide range of possible values. For this exercise and for simplicity only three cross-sections are chosen.

As an example, a mass displacement of at least  $4.0 \text{ e-}6 \text{ m}$  is desired from the design. From Fig. 4.5, an acceptable set of dimensions are: length =  $0.1 \text{ m}$ , cross-section =  $3.2 \text{ e-}6 \text{ m}^2$  (from Curve B). Moving to Fig. 4.6 shows that this choice for rod dimensions will yield approximately 138 Newtons of force for the driving voltage level of 15 volts pp at 810 Hz. If this force output is too small, then dimensions from Curve A or C could be chosen. However, any set of dimensions chosen to produce the required displacement will also provide the same 138 Newton force. Thus, the displacement and force are coupled as expected. Two solutions which will provide more force in this situation are an increase in driving field and modification of the Terfenol-D stoichiometry. However, gains made from increasing field levels are limited by saturation and gains from stoichiometry by the abilities of the material.

Another interesting aspect of this parametric study involves the effect of modifying the

fixture impedance on actuator output. The mass displacement and interaction force are shown in Fig. 4.7 and Fig. 4.8 respectively as functions of spring mass and stiffness for the driving voltage of 15 volts pp. The actuator casing is significantly stiffer than the spring and is therefore excluded from this study. The casing acts basically as a fixed boundary condition and the spring is the stiffness seen by the activated Terfenol-D rod. The three curves shown in each plot correspond to different levels of spring stiffness with the scaling factor introduced in Chapter 3 included. Both figures indicate that the output characteristics are nearly independent of the spring mass for this frequency. The same is found to be true for both a wider frequency range and for a larger range of mass values than is shown.

The top curve in both the displacement and interaction force plots contains the point representing the design of the modeled actuator. The other two curves represent output characteristics of systems with larger and smaller prestress spring stiffnesses. The ordering of these curves indicates that the only spring stiffness capable of producing a resonance at that

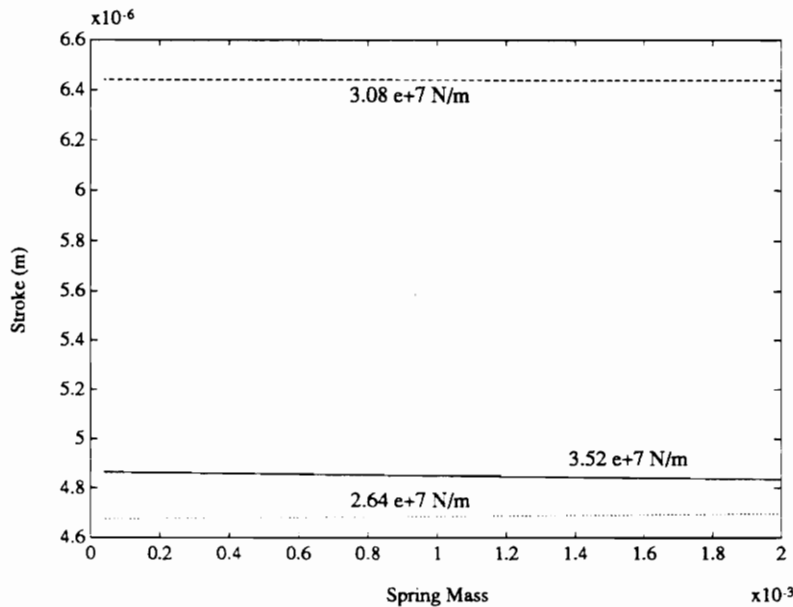


Figure 4.7: Mass Displacement as a Function of Fixture Spring Mass and Stiffness

particular frequency is that which corresponds to the top curve. This value is determined from the system identification technique described in Chapters 2 and 3. Increasing or decreasing this stiffness shifts the resonance point left or right and decreases the output value at that particular frequency as a result of being away from resonance.

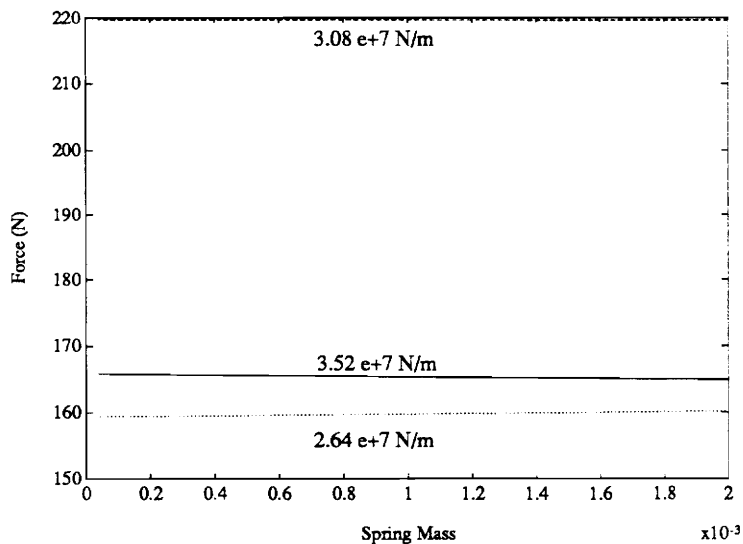


Figure 4.8: Interaction Force as a Function of Fixture Spring Mass and Stiffness

The coupled output characteristics of the Terfenol-D device are dependent on the nature of the impedance being driven (SMD in this example), the actuator dynamics, and the driving frequency. The general rules presented in literature state that increasing cross-sectional area increases force output and increasing rod length increases output displacement. Exceptions for these rules are found in the presented example in two locations. The mass displacement decreases with increasing rod length after the system resonance as a result of moving away from that maximum value. This effect is shown in Fig. 4.9 at a driving frequency of 1200 Hz for varying Terfenol-D rod lengths and cross-sections. The three curves in Fig. 4.9 correspond to the same cross-sectional areas shown previously in this



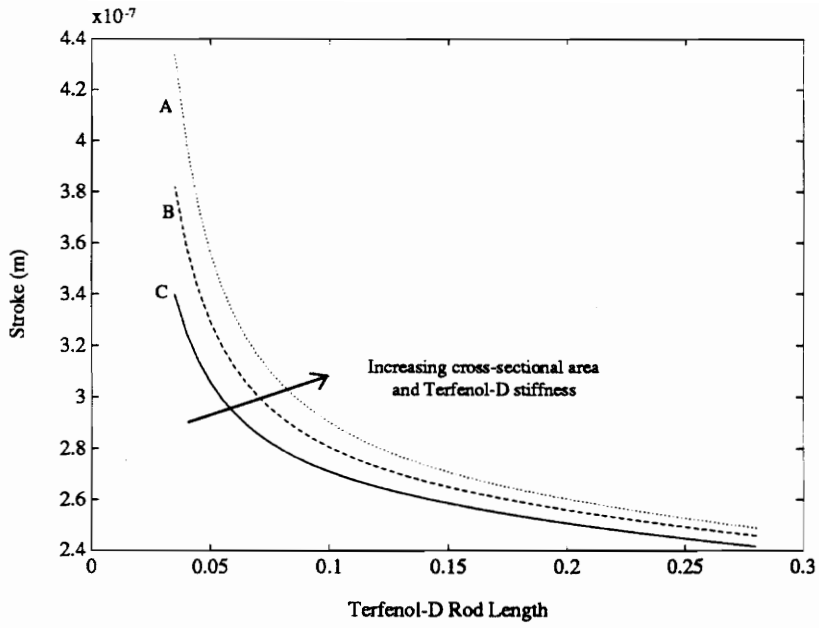


Figure 4.9: Example of Decreased Mass Displacement With Increased Terfenol-D Rod Length at 1200 Hz

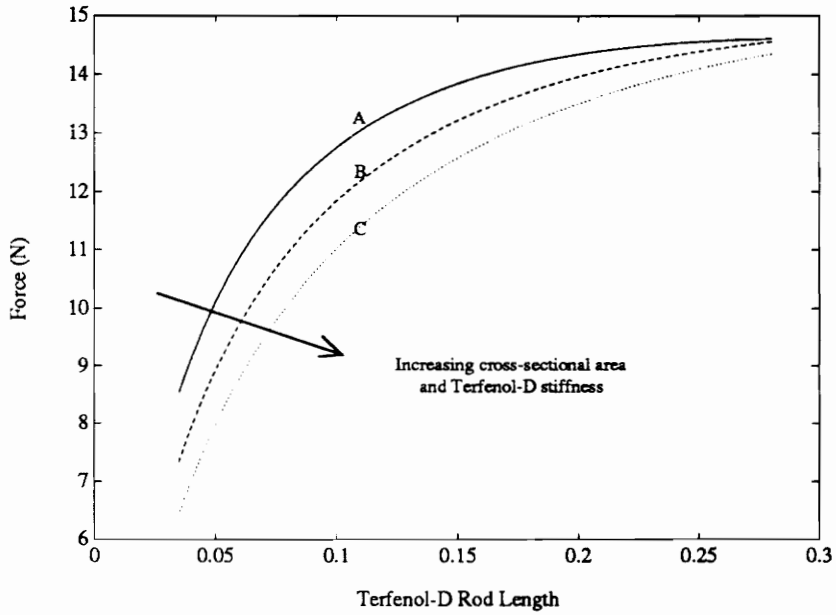


Figure 4.10: Example of Decreased Actuator/SMD Interaction Force With Increased Terfenol-D Rod Cross-section at 600 Hz

parametric study. Also, the actuator/SMD interaction force decreases with increasing rod cross-section and stiffness for the frequency range between 500 Hz (SMD resonance) and 810 Hz (system resonance). This is shown in Fig. 4.10 at a driving frequency of 600 Hz.

The transducer energy ratio for the Terfenol-D actuator and SMD combination is shown in Fig. 4.11 with maximum and minimum efficiencies at the system resonance and anti-resonance respectively.

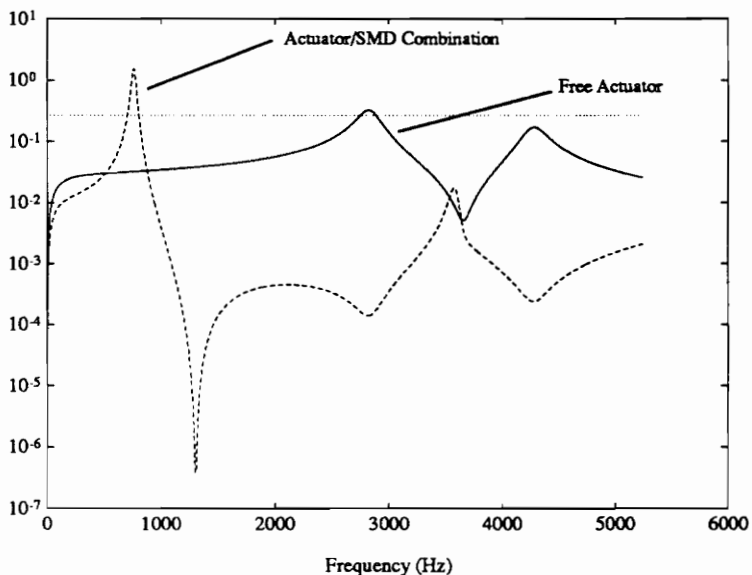


Figure 4.11: Energy Ratios For the Terfenol-D Actuator/SMD Combination and For the Free Actuator Showing Maximum Transducer Efficiencies

For any efficient actuator design, the impedance characteristics of the driven system need to be found experimentally or theoretically. Also, the output characteristics of the actuator and the driven structure need to be determined from the system dynamics and not by general rules as the literature suggests. Performing a simple parametric study like the one presented here will improve the capabilities of the actuator and eliminate design guesswork.

# Chapter 5

## Conclusions and Future Work

This work concentrates on developing a transduction representation for the Terfenol-D actuator. This characterization is made possible through application of an electro-magneto-mechanical impedance modeling approach which allows for a thorough investigation of the coupled behavior of the device. The Terfenol-D behavior is also presented from literature in order to better illustrate the existing complexities in actuator behavior and the need for development of improved models.

### 5.1 Summary of the Thesis

A description of the manner in which magnetostriction occurs and the non-linearity of Terfenol-D behavior is presented along with a summary of previous actuator modeling efforts as motivation for work aimed at improving the behavior characterization of the device.

Previous modeling work centered on static electro-magneto-mechanical relationships or controls-derived block diagram realizations as a means to simulate and approximate the behavior of Terfenol-D actuators. This work proved inadequate in predicting the dynamic behavior and the effects of the dynamic coupling present.

An electro-magneto-mechanical impedance modeling approach, combined with the constitutive equations for Terfenol-D, allows for simultaneous investigation of the mechanical and electrical behaviors of the actuator and the degree of coupling present. This leads to the development of a set of transduction expressions which describe the input/output characteristics of the actuator in measurable mechanical and electrical properties. These transduction expressions are based on coupled mechanical and electrical impedance models. A complete mechanical impedance model of the actuator system is developed using lumped approximations for masses and stiffnesses and continuous expressions for the Terfenol-D rod and actuator output rod. This analysis provides force and displacement relationships for all of the actuator components in terms of electrical, material, and physical system parameters. The electrical impedance model identifies the effects of the mechanical interaction and provides insight into the dissipative power consumption of the device. The transduction expressions also allow for investigation of the efficiency of the actuator as a transducer.

Modeling of the actuator, supplied by Intelligent Automation, Inc. (IAI), proved to be difficult as a result of the inability to disassemble the device per request of the manufacturer and the unavailability of certain material constants and physical dimensions. Use of representative values presented in the literature combined with known information and approximation of the rod dimensions and internal prestress spring mass allows for the implementation of a system identification technique to determine the equivalent fixture stiffness.

Experimental data provides the necessary resonant frequency information to identify the stiffness of the actuator fixture. This data also allows for correlation between theoretical

and electrical free-stroke to voltage transfer functions and real and imaginary electrical impedances. The correlation quality is excellent for the transfer function and reasonable for the electrical impedance. The electrical non-linearity of the coil combined with an inadequate knowledge of the frequency dependence of properties relating induced strain to applied field causes this deficiency in the model. Exchanging the experimental electrical impedance data for the theoretical expression in the previously mentioned transfer function produces some variation in behavior before the first resonance and alters the height of the resonant peak. The resonant frequency is, however, correctly identified. Experimental analysis of a separate actuator coil, also provided by IAI, allowed for adjustment of the effective coil permeability, addition of a dc resistance to the model, and approximation of the inductive loss factor.

Experimental verification of the developed model also allows for a complete analysis of internal and external force transfer and provides knowledge of the stress levels experienced by the Terfenol-D. These stress levels are shown to vary significantly from the applied prestress levels at the resonant frequency of the Terfenol-D rod. This variation in the total state of stress in the material alters the stress dependent strain vs. applied field "d" constant. Analysis also shows that the Terfenol-D rod in this actuator configuration experiences very similar stress levels from dc activation to the first actuator resonance at 3100 Hz for both free and blocked actuator conditions. This is attributed to the low stiffness of the material in comparison to the prestress spring or blocked boundary condition. At low frequency values where the actuator structure is very rigid, the Terfenol-D rod attempts to expand against a much larger external impedance. Near the system resonance for the free boundary condition, the actuator fixture becomes dynamically "soft" and the Terfenol-D is better able to accelerate those portions of the

actuator system. The stress inside the Terfenol-D decreases as the material dynamic stiffness increases in comparison to the rest of the system.

Further experimental investigation displays the observed non-linear acceleration and current wave forms at low excitation frequencies. The non-linear time-domain acceleration behavior in the region near resonance is shown for the free actuator.

Dissipative power consumption is also shown with the blocked electrical impedance having only a small amount of mechanical interaction as a result of decreased motion and dynamics with that boundary condition. This reduced interaction for the blocked actuator then shows the free actuator having the maximum power consumption at system resonance. Knowledge of this power dissipation allows for predictability of actuator behavior modification as a result of the conversion of electrical energy to thermal energy. The transducer energy ratio is presented as a material-based quantity and as a frequency dependent expression developed from a two-port network description shown in Chapter 1. This energy ratio, which is a measure of efficiency, is shown to be dependent on not only the excitation frequency of the system, but also the boundary conditions of the actuator.

## **5.2 Contributions**

The contribution of this work is the development of a set of transduction expressions that define the complete behavior of the system in terms of measurable electrical and mechanical properties. The complexity of the electro-magneto-mechanical interaction in the device can be seen when comparing the developed expression to the constitutive

equations for Terfenol-D as displayed on the following page.

The developed transduction model includes the mechanical dynamics and system coupling where previous research efforts have failed to do so. The investigation of this complex electro-magneto-mechanical behavior provides a powerful tool which serves as the basis of more complete device characterization. The material properties used in this work for an initial and mostly successful model correlation are constants. However, more comprehensive expressions for these material properties that vary with applied stress and driving field levels can be substituted into the transduction equations thus allowing for further improvement of the model. The transduction model also serves as a design and analysis tool with which any aspect of actuator behavior can be identified as a function of the parameters of the entire system. Output stroke and force, power consumption, and efficiency as a transducer are examples of the frequency and boundary condition dependent behaviors that the transduction expressions can identify.

The model also benefits application in the controls community by providing an increased knowledge of the coupling in the device and explicit expressions governing behavior. This understanding eliminates the need for using adaptive or ANN controllers in conjunction with Terfenol-D actuators because of the modeling inadequacies of the past. The realization of a collocated actuator/sensor is also made possible with use of the developed model.

The general approach utilized in this thesis can also be applied to similar actuator designs that use different induced strain materials such as piezoelectric or PMN stack actuators.

The Original Terfenol-D Constitutive Equations

$$S = s^H T + dH$$

$$B = dT + \mu^T H$$

The Finalized Transduction Equations

$$u = j\omega dN \left[ \frac{Z_T}{Z_T + Z_H} \right] \left[ \frac{\tan(\kappa_T l_T)}{\kappa_T l_T} \right] I + \frac{F}{Z_T + Z_H}$$

$$V = \frac{j\omega N^2 A_T}{l_T} \left\{ d^2 \bar{Y}^H \left[ \frac{Z_T}{Z_T + Z_H} \right] \left[ \frac{\tan(\kappa_T l_T)}{\kappa_T l_T} \right] + (\mu^T - d^2 \bar{Y}^H) \right\} I + j\omega dN \left[ \frac{Z_T}{Z_T + Z_H} \right] \left[ \frac{\tan(\kappa_T l_T)}{\kappa_T l_T} \right] F$$



The correlation quality of the initial theoretical actuator transfer functions and free electrical impedance expressions validate the efforts to date. The developed model shows promise as a basis for more complete device characterization.

### **5.3 Future Work**

The most important first step in any future work is the testing of other "identical" actuators in order to determine both the accuracy of the developed model and measure the reproducibility of this Terfenol-D actuator design. The inability of manufacturers to produce a certain actuator design in numbers with a good degree of consistency will hamper any modeling efforts including the work done in this thesis.

The suggestions for future investigations involving the Terfenol-D actuator consist of two main categories: model improvement and device improvement. The objective of the work presented in this thesis is to develop closed-form, dynamic expressions for all aspects of the actuator behavior and investigate the electro-magneto-mechanical coupling in the device. With this goal met, knowledge of the contribution of every variable or material property to actuator behavior can be evaluated and improved. The most prevalent example of this needed model improvement involves the degree of Terfenol-D material non-linearity. As shown in Chapter 1, Terfenol-D exhibits a typical magnetic hysteresis loop between induced flux density and applied magnetic field. This, in turn, greatly complicates the induced strain behavior of the material. Besides the mentioned hysteresis, Terfenol-D also exhibits regions where a non-linear relationship exists between induced strain and applied field. This combined effect creates a magnetic to mechanical interaction that is complex. Ramifications of this complexity are shown by

Butler (1988) and presented in Chapter 1 as a field and strain dependent Young's Modulus. Therefore, when the Terfenol-D material is being excited, the Young's Modulus becomes a function of both frequency and an electrical drive level (current or voltage). This varying modulus affects the wave number of the Terfenol-D and distorts the frequency characteristic of this induced strain material and of the actuator as a whole. Another complexity associated with the actuator design is the effect the dynamically induced stress has on the strain output characteristics of the material. The concept of a linear actuator operation range is presented in Chapter 1. This range consists of a bias point in the center of a linear region of a strain vs. applied field relationship. Increasing and decreasing the applied field then theoretically makes the Terfenol-D expand and contract along that line with the slope of that movement being the "d" constant. The problem with this assumption is that each strain vs. applied field curve is shown in the literature to correspond to a certain level of applied prestress. These curves were obtained experimentally by maintaining a constant level of stress on a Terfenol-D sample while a dc applied field is increased. In a dynamic situation, like that which exists inside the actuator, the levels of stress can vary significantly as is shown in Chapter 3. Thus, as the stress inside the Terfenol-D changes during dynamic operation, the effective "d" constant also changes and the material operates not on a line, but in a region as shown in Fig. 5.1. Until the significance of these effects are better understood, the theoretical success in predicting actuator behavior without previous experimentation will vary from design to design. Development of some type of fixture which could produce adequate blocking boundary conditions would also facilitate verification of the actuator behavior in that configuration. The difficulty involved in performing experimental verification of blocked boundary conditions exists in the need to apply a constant external impedance that is both constant and large enough to overcome any actuator dynamics that would act

to relieve stress in the system.

On the electrical side of the actuator, the model of the input coil requires improvement. The coil inside the borrowed actuator experimentally shows a significant inductive and possibly capacitive loss factor. The model developed in Chapter 2 assumes the coil behaves as an inductor. This model is improved by baseline adjusting the free permeability, adding a dc resistance, and approximating the non-linear loss factor.

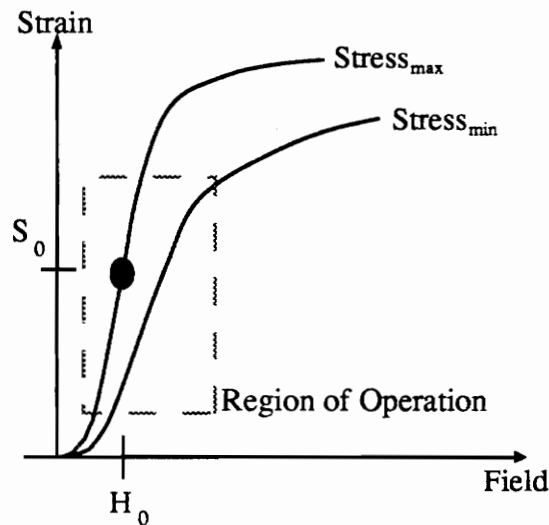


Figure 5.1: The Region of Operation for a Terfenol-D Actuator Between Two Curves Representing Minimum and Maximum Stress Levels

However, none of this model adjustment is possible without preliminary experimentation. Therefore, the future work needed in this area is two-fold. The first is simply to construct a more comprehensive model of this non-linear electrical behavior in an attempt to identify such as a function of the physical properties and dimensions of the coil. This

modeling work should accompany design improvement with the goal of identifying and minimizing the sources of electrical non-linearity that the coil introduces into the actuator behavior.

Another actuator design area that requires work is improvement of low-frequency characteristics. Magnetostrictive actuators are realistically limited in frequency range because of eddy currents that develop in the coil which produce distortions in the magnetic field, reverse magnetostriction effects, and heat.

More complete characterization of Terfenol-D actuators and consistent manufacturing will allow for use of the device as a collocated actuator/sensor. The developed transduction equations, presented in Chapter 2, show that with two easily measured electrical quantities (voltage and current), the Terfenol-D actuator can perform the tasks of sensing and actuating simultaneously. However, the accuracy of this function will be determined by the quality of actuator behavior characterization.

## References

- Anjanappa, M. A. and J. Bi. 1993. "Modeling, Design and Control of Embedded Terfenol-D Actuators", Proceedings of SPIE Smart Structures and Materials 1993, Albuquerque, New Mexico, 1-4 February.
- Bryant, M. D., Fernandez, B., Wang, N., Murty, V. V., Vadlamani, V. and T. S. West. 1992a. "Active Vibration Control in Structures Using Magnetostrictive Terfenol With Feedback and/or Neural Network Controllers", Proceedings of the Conference on Recent Advances in Adaptive and Sensory Materials and Their Applications, 27-29 April, 465-479.
- Bryant, M. D., N. Wang. 1992b. "Audio Range Dynamic Models and Controllability of Linear Motion Terfenol Actuators", Proceedings of the Conference on Recent Advances in Adaptive and Sensory Materials and Their Applications, 27-29 April, 398-408.
- Butler, J. L. 1988. "Application Manual For the Design of Etrema™ Terfenol-D Magnetostrictive Transducers", Edge Technologies, Inc., Etrema™ Division, Ames, Iowa.
- Clark, A. E. 1992. "High Power Rare Earth Magnetostrictive Materials", Proceedings of the Conference on Recent Advances in Adaptive and Sensory Materials and Their Applications, 27-29 April, 387-397.

- Dyberg, J. 1986. "Magnetostrictive Rods in Mechanical Applications", First International Conference on Giant Magnetostrictive Alloys and Their Impact on Actuator and Sensor Technology, Marbella, Spain, 7-9 March.
- Fenn, R. C., Bushko, D. A. and M. J. Gerver. 1993. "Magnetostrictive Structural Elements Fabricated From Metallic Glass", Proceedings of SPIE Smart Structures and Materials 1993, Albuquerque, New Mexico, 1-4 February.
- Flatau, A. B., Hall, D. L. and J. M. Schlesselman. 1992. "Magnetostrictive Active Vibration Control Systems (A Preliminary Investigation)", Proceedings of the Conference on Recent Advances in Adaptive and Sensory Materials and Their Applications, 27-29 April, 419-429.
- Goodfriend, M. J., Shoop, K. M. and O. D. McMasters. 1992. "Characteristics of the Magnetostrictive Alloy Terfenol-D Produced For the Manufacture of Devices", Proceedings of the Conference on Recent Advances in Adaptive and Sensory Materials and Their Applications, 27-29 April, 448-456.
- Hall, D. L. and A. B. Flatau. 1993. "Nonlinearities, Harmonics, and Trends In Dynamic Applications of Terfenol-D", Proceedings of SPIE Smart Structures and Materials 1993, Albuquerque, New Mexico, 1-4 February.
- Halliday, D. and R. Resnick. 1988. Fundamentals of Physics, 3rd Ed., Wiley, 714-727,764-767.

- Harris, C. M. 1988. Shock and Vibration Handbook, 3rd Ed., MacGraw-Hill, 10.1-10.46.
- Haynes, L., Geng, Z. and J. Teter. 1993. "A New Terfenol-D Actuator Design With Application to Multiple DOF Active Vibration Control", Proceedings of SPIE Smart Structures and Materials 1993, Albuquerque, New Mexico, 1-4 February.
- Hiller, M. W., Bryant, M. D. and J. Umegaki. 1989. "Attenuation and Transformation of Vibration Through Active Control of Magnetostrictive Terfenol", Journal of Sound and Vibration, 134:507-519.
- Ikeda, T. 1990. Fundamentals of Piezoelectricity, Oxford Science Publications, 5-30.
- Kinsler, L. E., Frey, A. R., Coppens, A. B. and J. V. Sanders. 1982. Fundamentals of Acoustics, 3rd Ed., Wiley, 344-349.
- Moffett, M. B., Clark, A. E., Wun-Fogle, M., Lindberg, J. F., Teter, J. P. and E. A. McLaughlin. 1991. "Characterization of Terfenol-D For Magnetostrictive Transducers," Journal of the Acoustic Society of America, 89:1448-1455.
- Nilsson, J. W. 1990. Electric Circuits, Addison-Wesley, 3rd Ed., 368-371.
- Norton, H. N. 1990. Eshbach's Handbook of Engineering Fundamentals, 4th Ed., Wiley, 12.80-12.88.

Norton, H. N. 1989. Handbook of Transducers, Prentice Hall Publishing, 17-30.

Oswin, J. R., Edenborough, R. J. and K. Pitman. 1988. "Rare-Earth Magnetostriction and Low Frequency Sonar Transducers," Presented at IOP/IEEE/IEEE Seminar on Magnetic Sensors and Amorphous Materials, 20 April.

Pratt, J. and A. B. Flatau. 1993. "Development and Analysis of a Self-sensing Magnetostrictive Actuator Design," Proceedings of SPIE Smart Structures and Materials 1993, Albuquerque, New Mexico, 1-4 February.

Reed, R. S. 1988. "Model of a Magnetostrictive Actuator With Application To Simple Systems," Modeling and Simulation: Proceedings of the Annual Pittsburgh Conference, 19:2105-2109.

Smith, W. F. 1990. Principles of Materials Science and Engineering, 2nd Ed., MacGraw-Hill Publishing Co., 635-675.

Snowdon, J. C. 1968. Vibration and Shock In Damped Mechanical Systems, Wiley, 134-135.

Thomson, W. T. 1988. Theory of Vibrations, 3rd Ed., Prentice Hall Publishing, 216-218.



## Appendix A: Non-linear Time Domain/Spectra of Actuator Behavior

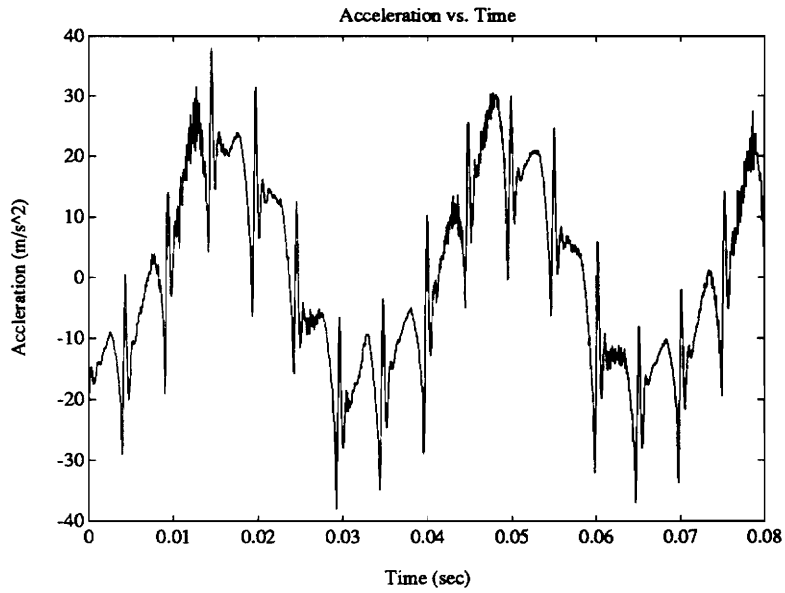


Figure A1: Actuator Non-linear Output Acceleration With a 30 Hz Driving Voltage

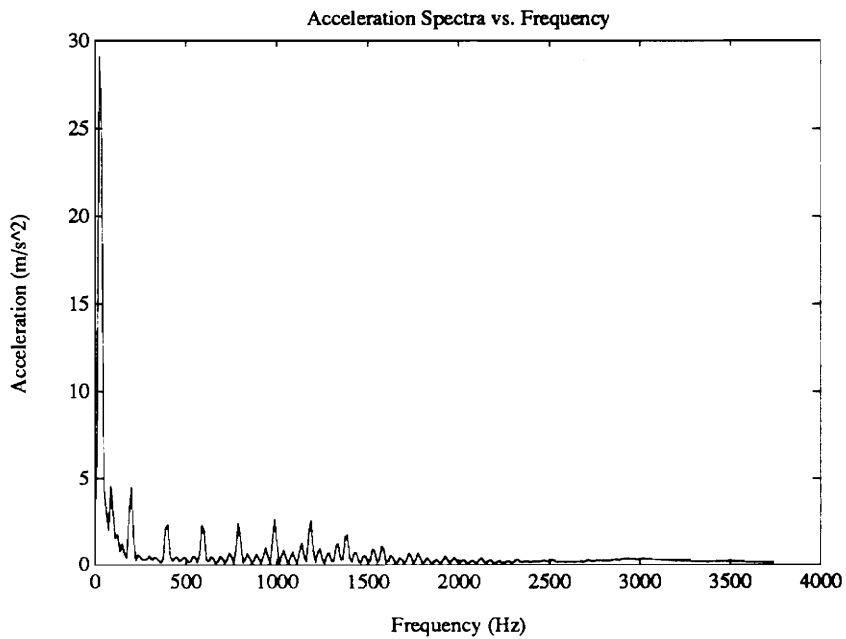


Figure A2: Actuator Non-linear Output Acceleration With a 30 Hz Driving Voltage  
(Frequency Spectra)

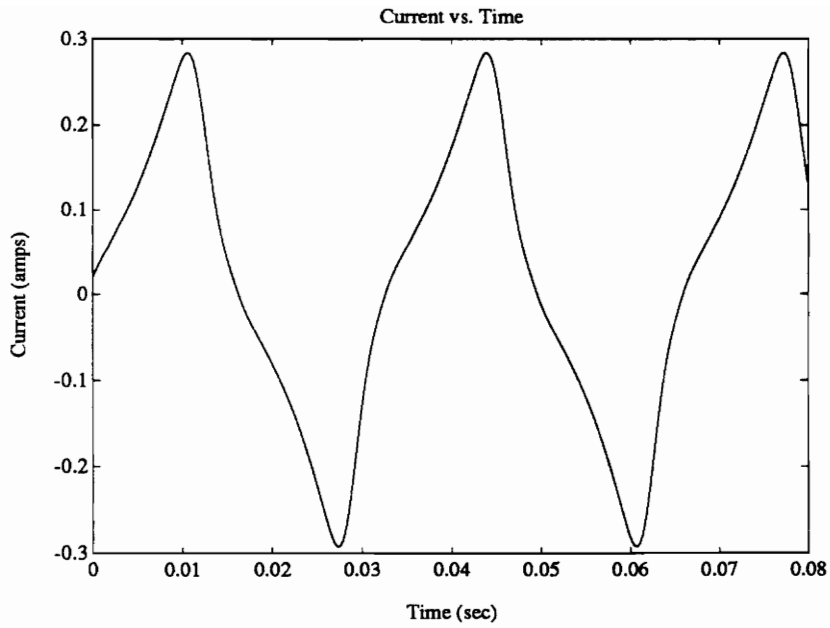


Figure A3: Actuator Non-linear Coil Current With a 30 Hz Driving Voltage

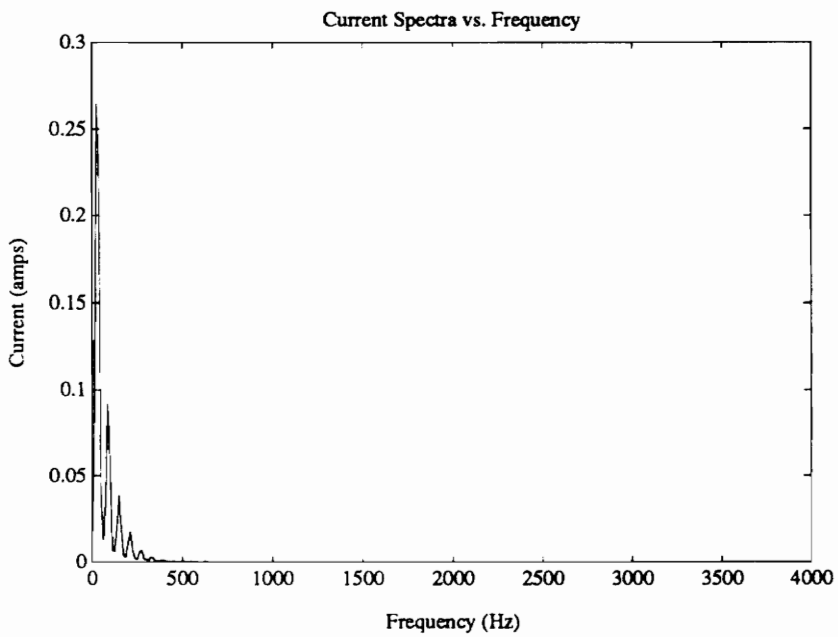


Figure A4: Actuator Non-linear Coil Current With a 30 Hz Driving Voltage  
(Frequency Spectra)

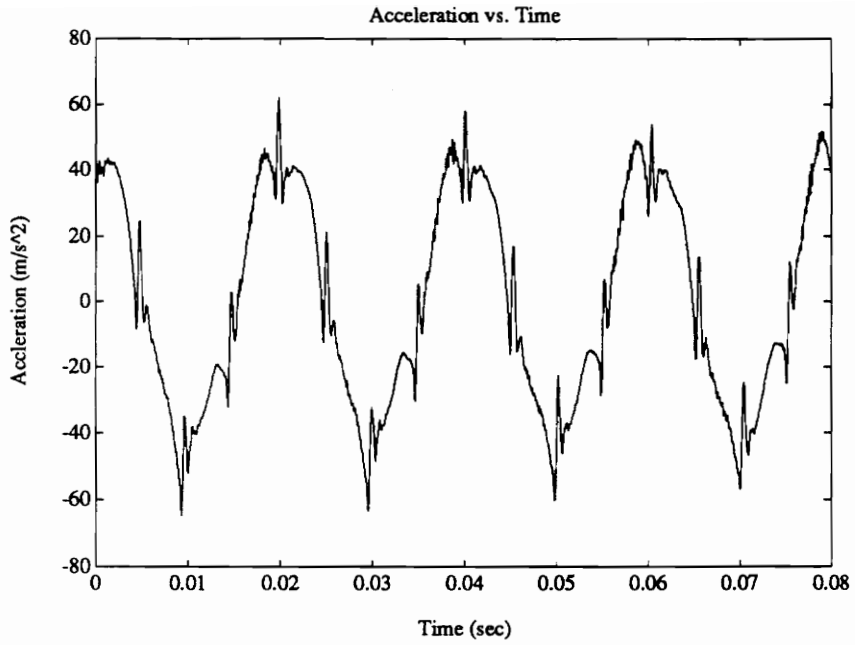


Figure A5: Actuator Non-linear Output Acceleration With a 50 Hz Driving Voltage

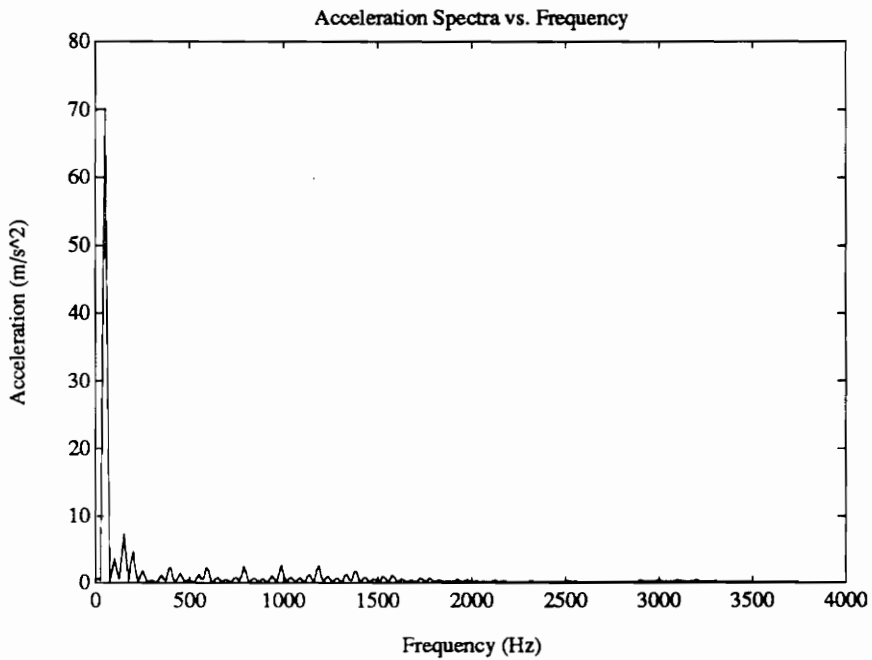


Figure A6: Actuator Non-linear Output Acceleration With a 50 Hz Driving Voltage  
(Frequency Spectra)

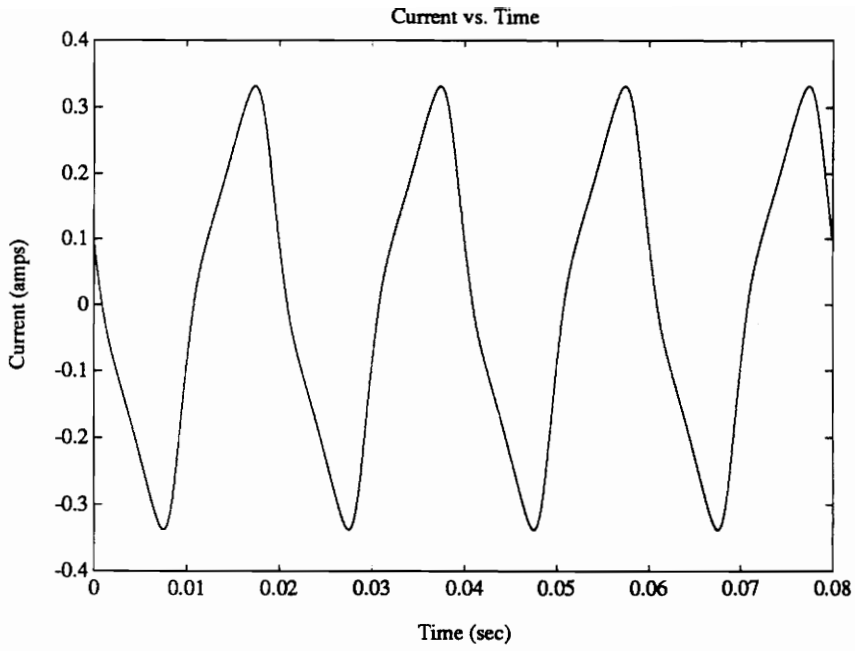


Figure A7: Actuator Non-linear Coil CurrentWith a 50 Hz Driving Voltage

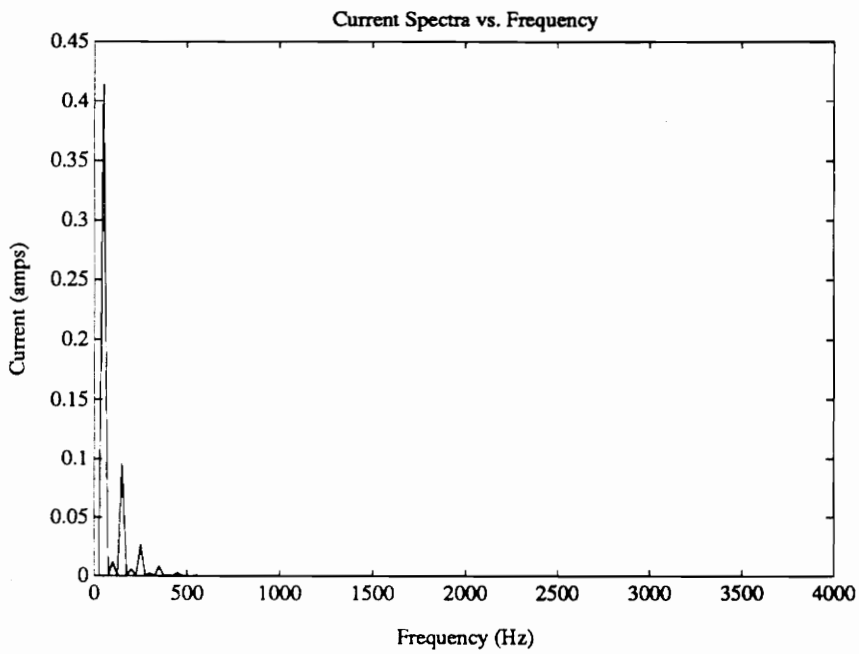


Figure A8: Actuator Non-linear Coil CurrentWith a 50 Hz Driving Voltage  
(Frequency Spectra)

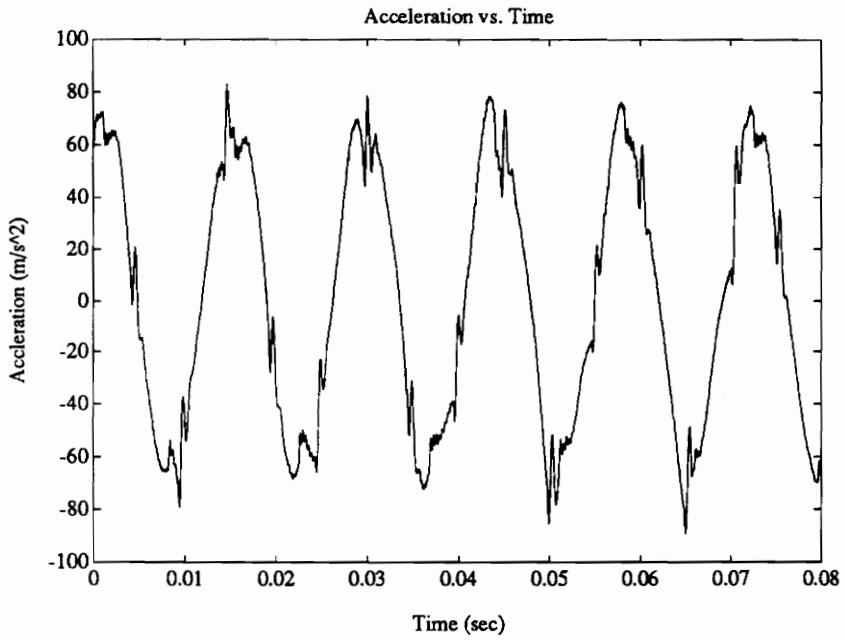


Figure A9: Actuator Non-linear Output Acceleration With a 70 Hz Driving Voltage

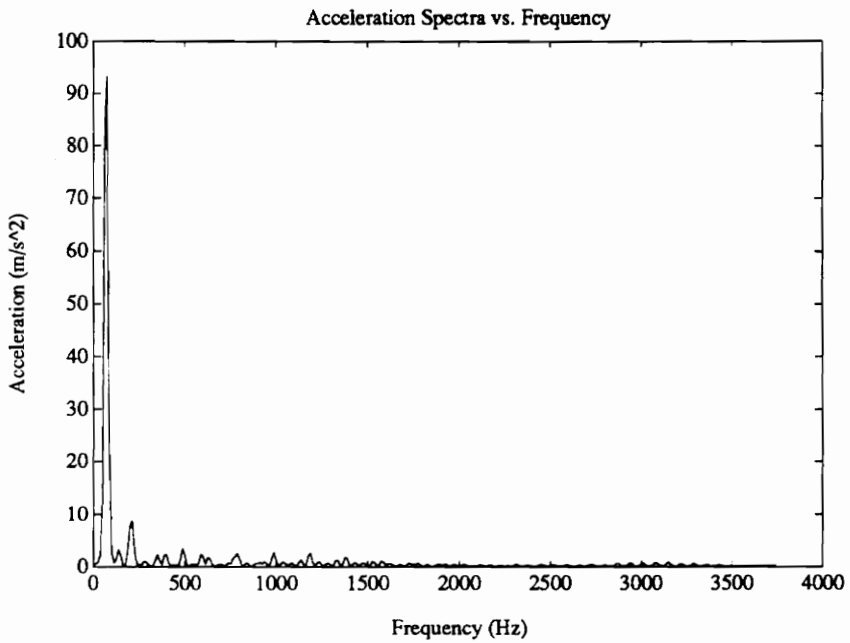


Figure A10: Actuator Non-linear Output Acceleration With a 70 Hz Driving Voltage  
(Frequency Spectra)

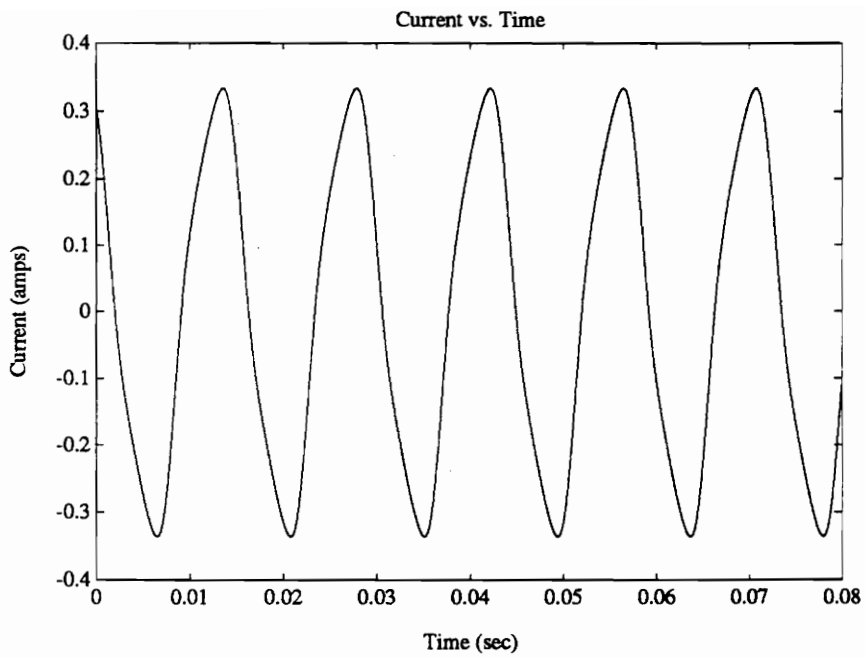


Figure A11: Actuator Non-linear Coil Current With a 70 Hz Driving Voltage

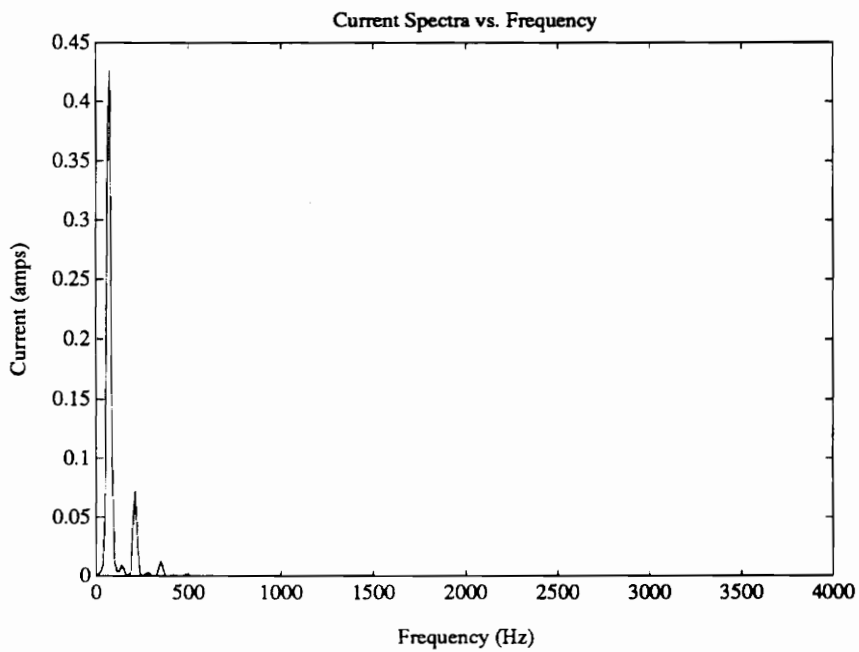


Figure A12: Actuator Non-linear Coil Current With a 70 Hz Driving Voltage  
(Frequency Spectra)

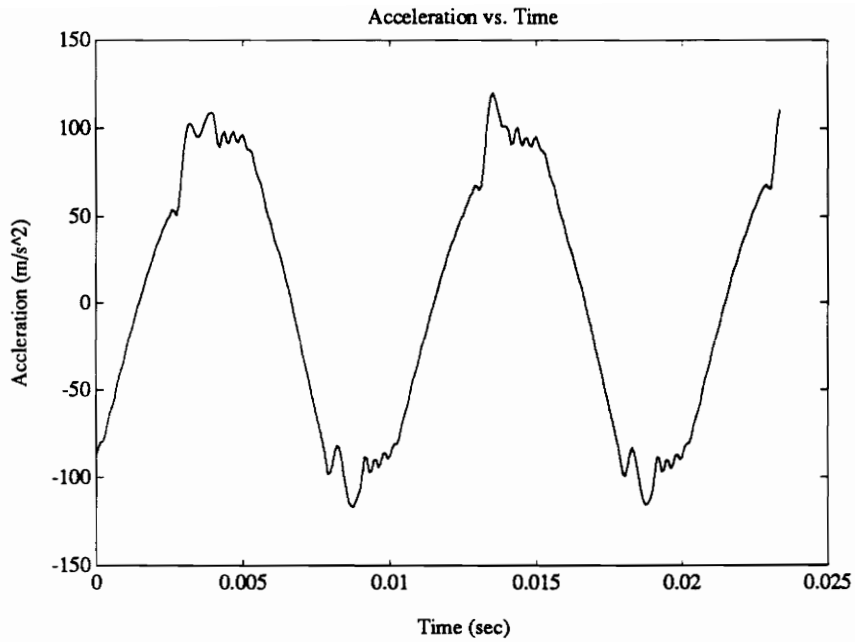


Figure A13: Actuator Non-linear Output Acceleration With a 100 Hz Driving Voltage

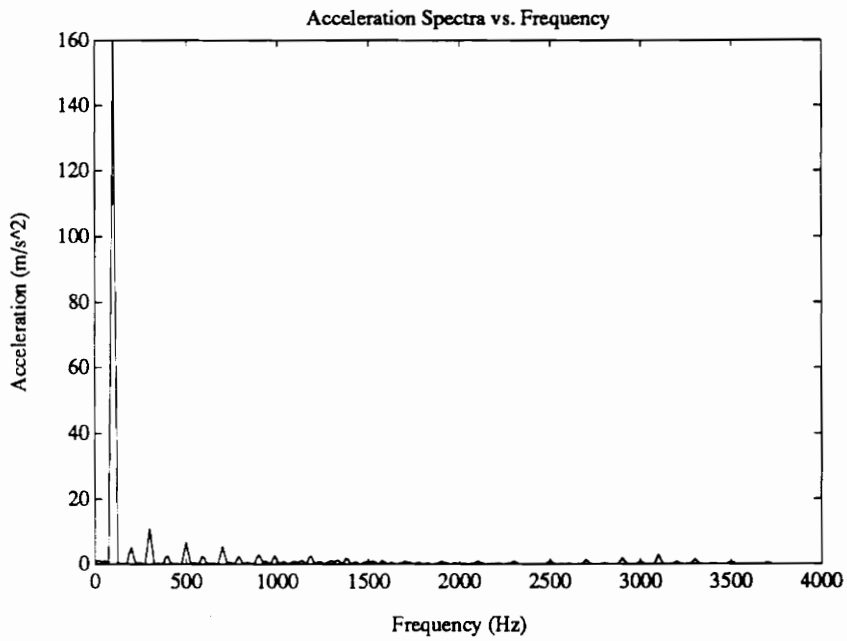


Figure A14: Actuator Non-linear Output Acceleration With a 100 Hz Driving Voltage  
(Frequency Spectra)

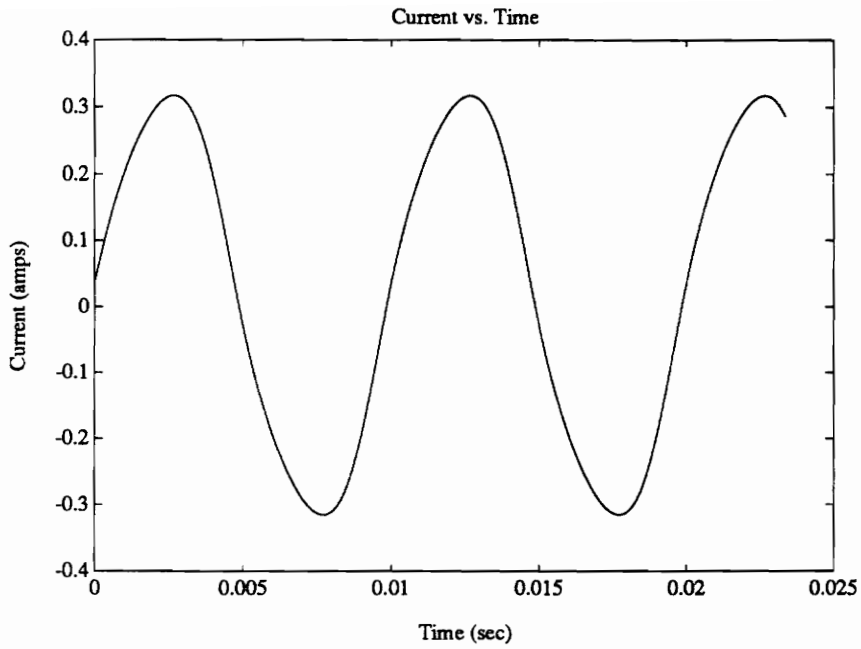


Figure A15: Actuator Non-linear Coil Current With a 100 Hz Driving Voltage

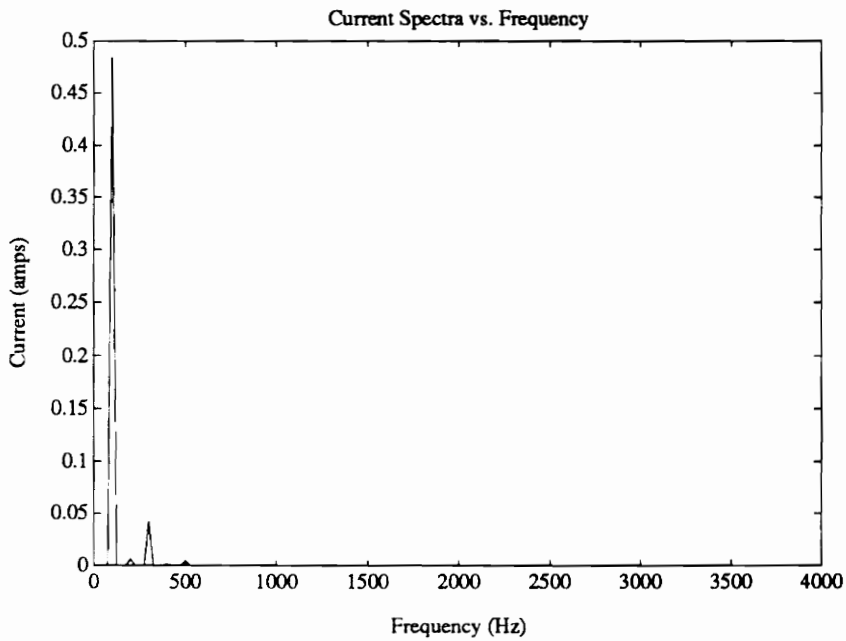


Figure A16: Actuator Non-linear Coil Current With a 100 Hz Driving Voltage  
(Frequency Spectra)



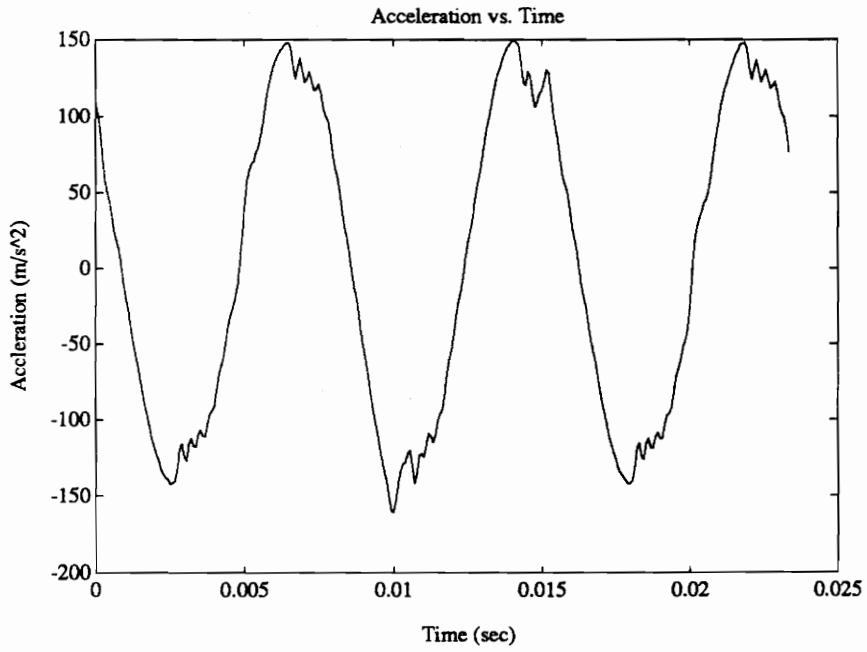


Figure A17: Actuator Non-linear Output Acceleration With a 130 Hz Driving Voltage

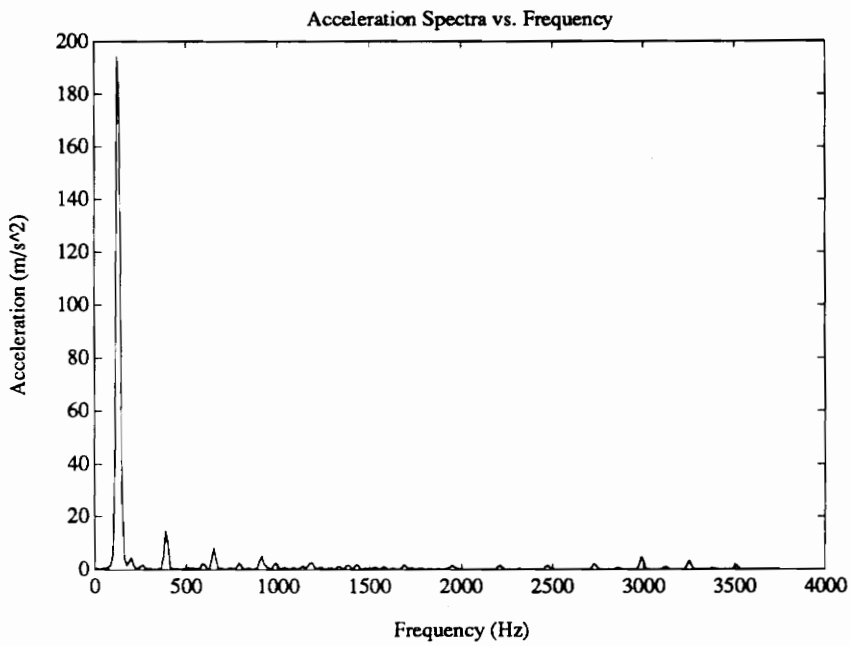


Figure A18: Actuator Non-linear Output Acceleration With a 130 Hz Driving Voltage  
(Frequency Spectra)

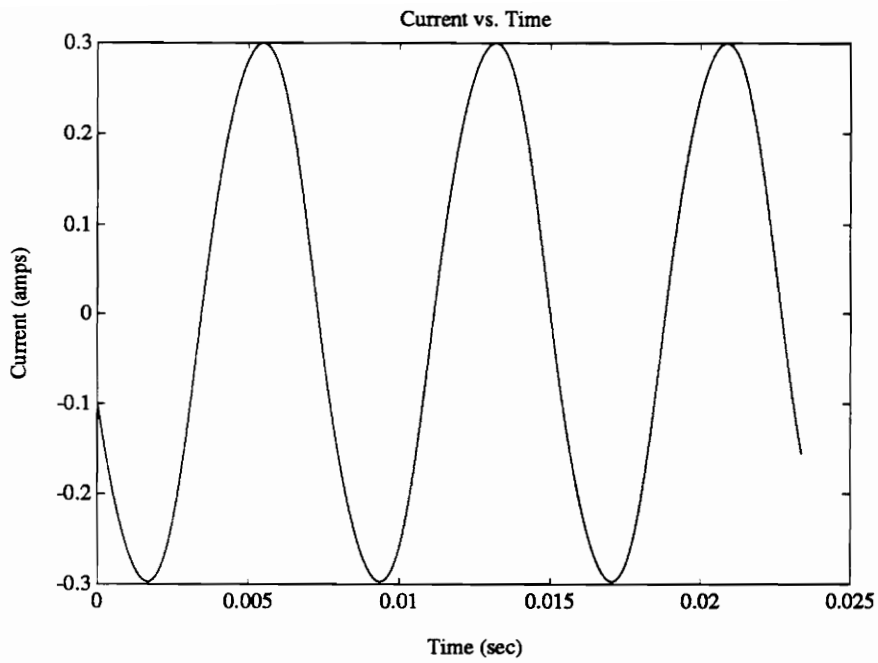


Figure A19: Actuator Non-linear Coil Current With a 130 Hz Driving Voltage

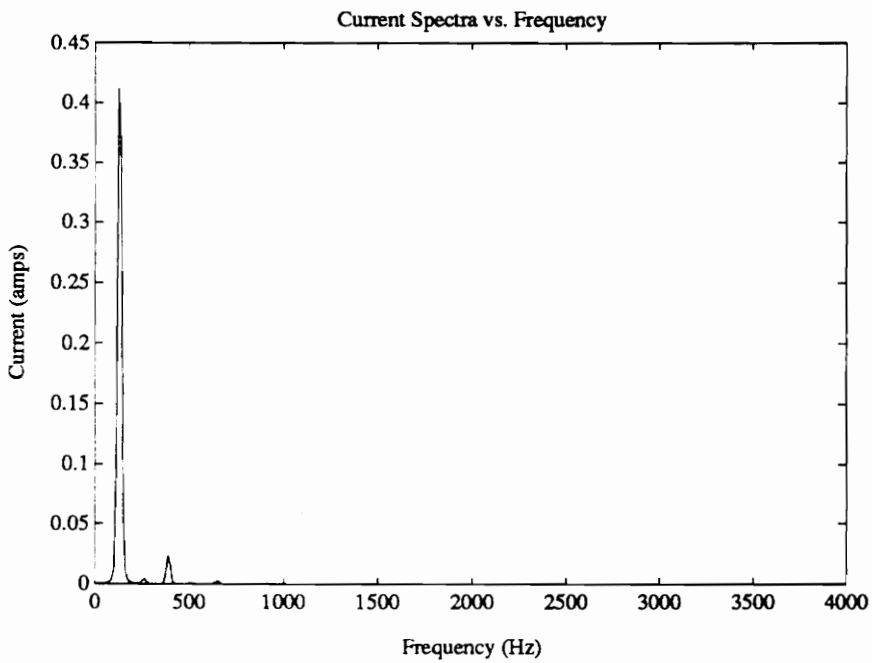


Figure A20: Actuator Non-linear Coil Current With a 130 Hz Driving Voltage  
(Frequency Spectra)

## Appendix B: Matlab and Mathematica Computer Codes

This Appendix contains all of the simulation and calculation codes used to produce plots and simulations presented in the thesis. The computer codes follow the list of contents in the order shown below.

<u>Name</u>	<u>Function Performed</u>	<u>Language</u>
BF.M	Investigation of Internal Actuator Force Transfer and Terfenol-D Stress	Matlab
DES.M	System Behavior Analysis With Attached SMD	Matlab
EIMP.M	Electrical Impedance	Matlab
ITF.M	Free-stroke To Current Transfer Function	Matlab
PARAMET.M	Loads All Actuator Mechanical and Electrical Properties	Matlab
PHI.M	Calculates the Transduction Coefficient and Energy Ratio	Matlab
POWER.M	Calculates the Dissipative Power Consumption	Matlab
SINGLELA.M	Terfenol-D Length and Cross-sectional Area Behavior Parameter Study	Matlab
SINGLEMK.M	Actuator Spring Mass and Stiffness Behavior Parameter Study	Matlab
SINGLEP.M	Fixed Parameter Set for the Actuator Performance Parameter Studies	Matlab
SYS2.M	Transcendental Equation Plotting	Matlab

<u>Name</u>	<u>Function Performed</u>	<u>Language</u>
VTF.M	Free-stroke To Voltage Transfer Function	Matlab
VTF2.M	Free-stroke To Voltage Transfer Function (With Experimental Electrical Impedance)	Matlab
SYSID	Perform System Identification	Mathematica

```

% B.F.M

% Studying force transfer inside the actuator and the blocking
% force output

% Load parameter set

paramet

% Load the blocked and free theoretical electrical impedance

load temp;

% Stress developed in the Terfenol-D rod in the free and
% blocked actuator conditions

t1v_free=-yt.*d.*N./(lt.*impth).*(zh_free)./(z_terf+zh_free).*tan(t_arg)./(t_arg);
t1v_blk=-yt.*d.*N./(lt.*impth_blk).*(zh_blk)./(z_terf+zh_blk).*tan(t_arg)./(t_arg);

% Force/voltage applied to the output rod with a
% blocked actuator condition

f3v_blk=zc_blk.*j.*w.*d.*N./(impth_blk).*z_terf./(z_terf+zh_blk).*tan(t_arg)./t_arg;

% Actuator output blocking force/voltage

f4v_blk = f3v_blk ./ (c + j .* zo ./ zsbk .* s);

% Plot results

semilogy(ww,abs(t1v_free),ww,abs(t1v_blk))
title('Terfenol-D Stress/voltage: free and blocked actuator')
xlabel('Frequency (Hz)')
ylabel('Stress/voltage (Pa/V)')
pause
% meta b

semilogy(ww,abs(f4v_blk))
title('Actuator Output Blocking Force/voltage')
xlabel('Frequency (Hz)')
ylabel('Force/voltage (F/V)')
pause
% meta c

semilogy(ww,abs(f3v_blk))
title('Input Force (F3)/voltage to Output rod')
xlabel('Frequency (Hz)')
ylabel('Force/voltage (F/V)')
pause
% meta d

% Investigate the total state of stress with a bias
% (driving level of 15 volts pp)

```

```
pstress = -2000 * 4.45 / (.0254)^2;
bias = w .* pstress ./ w;

plot(ww,15 .* real(tlv_free)+bias,ww,bias)
title('Terfenol-D Stress (Free Actuator) driven at 15 vpp')
xlabel('Frequency (Hz)')
ylabel('Stress (Pa)')
% meta a
```

```

% DES.M

% Analysis of System Behavior With the Actuator Driving a SMD

% Load parameter set

paramet

% Choose appropriate drive level

drive = 15;

% Calculate the electrical impedance

imp1_fr = (d^2.*yt.*z_terf./(z_terf+zh_m)).*(tan(t_arg)./t_arg);
imp2_fr = u-d^2.*yt;

impthm = dc_res+j.*w.*N^2.*at.*(imp1_fr+imp2_fr)./lt;

% Actuator stroke/voltage output

xlv_m = d.*N./impthm.*(tan(t_arg)./t_arg).*z_terf./(z_terf+zh_m)
;
x4v_m = zo .* xlv_m ./ (zo .* c + j .* zsm .* s);

% Actuator force/voltage output

f3v_m = zc_m .* xlv_m .* j .* w;
f4v_m = f3v_m ./ (c + j .* zo .* s ./ zsm);

% Actuator impedance

zs2 = z_terf + z_fix;
% zr2 = zo .* (zs2 + j .* zo .* t) ./ (zo + j .* zs2 .* t);
zr2 = zr_mass + zs2;

% Plot results

semilogy(ww,abs(zr2),ww,abs(zsm))
title('Actuator and External Structure Impedance Magnitudes')
xlabel('Frequency (Hz)')
ylabel('Impedance (ohms)')
% meta one
pause;

semilogy(ww,drive .* abs(zrm),ww,drive .* abs(f3v_m ./ (j .* w .*
* xlv_m)))
title('Driving point impedance comparison')
pause

semilogy(ww,drive .* abs(x4v_m))
title('Output Stroke Magnitude vs. Frequency')
xlabel('Frequency (Hz)')
ylabel('Stroke (m)')
% meta two
pause;

```

```

semilogy(ww,drive .* abs(xlv_m),ww,drive .* abs(f3v_m ./ (zrm .*
j .* w)))
title('T Stroke Magnitude vs. Frequency')
xlabel('Frequency (Hz)')
ylabel('Stroke (m)')
% pause

semilogy(ww,drive .* abs(f4v_m))
title('Force Magnitude vs. Frequency')
xlabel('Frequency (Hz)')
ylabel('Force (N)')
% meta three
pause

semilogy(ww,abs(zsm),ww,abs(f4v_m ./ (j .* w .* x4v_m)))

```



```

% EIMP.M

% This code calculates the theoretical electrical impedance and
% performs the correlation between experimental data and the
% theoretical expression

% load experimental impedance data
ex2

% Load parameter set
paramet

% Theoretical free, blocked, and SMD electrical impedance
imp1_fr = (d^2.*yt.*z_terf./(z_terf+zh_free)).*(tan(t_arg)./t_ar
g);
imp2_fr = u-d^2.*yt;
imp1_blk = (d^2.*yt.*z_terf./(z_terf+zh_blk)).*(tan(t_arg)./t_ar
g);
imp1_m = (d^2.*yt.*z_terf./(z_terf+zh_m)).*(tan(t_arg)./t_arg);

impth = dc_res+j.*w.*N^2.*at.*(imp1_fr+imp2_fr)./lt;
impth_blk = dc_res+j.*w.*N^2.*at.*(imp1_blk+imp2_fr)./lt;
impth_m = dc_res+j.*w.*N^2.*at.*(imp1_m+imp2_fr)./lt;

% Saving the theoretical free and blocked electrical impedances
% for use in other codes

ff = ww;
save temp ff impth impth_blk impth_m;

% Plotting results

plot(ww,impth,f,funct,'w')
title('Real Electrical Impedance vs. Frequency')
xlabel('Frequency (Hz)')
ylabel('Impedance (ohms)')
pause;

plot(ww,imag(impth),f,imag(funct),'w')
title('Imaginary Electrical Impedance vs. Frequency')
xlabel('Frequency (Hz)')
ylabel('Impedance (ohms)')
pause;

plot(ww,abs(impth),f,abs(funct))
title('Electrical Impedance Magnitude vs. Frequency')
xlabel('Frequency (Hz)')
ylabel('Impedance (ohms)')
pause;

plot(ww,impth_blk)
title('Real Blocked Electrical Impedance vs. Frequency')
xlabel('Frequency (Hz)')
ylabel('Impedance (ohms)')

```

```

% ITF.M
% Calculates the free-stroke/current transfer function
% Load experimental data
    ex1
% Load parameter set
    paramet
% Actuator free-stroke/current transfer function
    x4_free=d.*N.*(tan(t_arg)./t_arg).*z_terf./(z_terf+zh_free);
% Plot results
    semilogy(ww,abs(x4_free),fe(35:420),xe(35:420))
    title('Stroke/Current vs. Frequency')
    xlabel('Frequency (Hz)')
    ylabel('Stroke (m)')

```

```

% PARAMET.M

% This code holds the values for the actuator parameters
% and performs several calculations common among all the
% simulation codes

% Fixture

% 1. ks = pre-stress spring constant
% 2. kc = casing stiffness
% 3. keq = equivalent fixture stiffness (ks,kc in series)
% 4. ms = spring mass

% Terfenol-D

% 1. nt = mechanical loss factor
% 2. lt = rod length
% 3. yt = Youngs modulus
% 4. pt = density
% 5. at = cross-sectional area
% 6. kt = stiffness
% 7. ch = speed of sound (H=0)

% Rod

% 1. nr = mechanical loss factor
% 2. mr = rod mass
% 3. lr = rod length
% 4. yr = Youngs modulus
% 5. pr = density
% 6. ar = cross-sectional area
% 7. kr = stiffness
% 8. cr = speed of sound

% Electrical

% 1. u = permeability
% 2. d = "d" constant
% 3. ne = inductive loss factor
% 4. N = number of turns in the coil
% 5. dc_res = dc resistance of the coil

ks = 350393.7 .* (1 + .1 .* j);
kc = 3.36E8 .* (1 + .005 .* j);
keq = (ks .* kc) ./ (ks + kc) .* 88;

ms = 0.001;

nt = 0.03;
lt = 0.2;
yt = 0.99 .* 20E9 .* (1 + nt .* j);
pt = 9.25E3;
at = 3.1669E-5;
kt = at .* yt ./ lt;
ch = 1 .* sqrt(yt ./ pt);

nr = 0.001;

```

```

mr = 0.069;
ar = 3.1669E-5;
lr = 0.05715;
yr = 207E9 .* (1 + nr .* j);
pr = 7801.35;
kr = ar .* yr ./ lr;
cr = sqrt(yr ./ pr);

ne = 0.33;
u = 1.8E-5 .* (1 - j .* ne);
d = 1.6E-8;
N = 2000;
dc_res = 6;

j = sqrt(-1);

% Frequency increment and vector length
w = (1:60:33000);
ww = w ./ (2 .* pi);

% Alternate frequency vector needed when converting and
% using experimental electrical impedance data in the
% free-stroke/voltage transfer function
ww = (100:12.25:5000)';
w = ww .* 2 .* pi;

% Terfenol impedance calculation
t_arg = w .* lt ./ ch;
t_const = kt .* lt ./ ch;
t_term = -(t_const ./ tan(t_arg)) .* j;
z_terf = t_term .* (1 + j .* nt);

% Actuator fixture impedance (spring and casing)
z_fix = (ms .* w - keq ./ w) .* j;

% Free rod (mass) impedance
zr_mass = j .* w .* mr;

% External impedances defined
zsbk = -j .* 1E50 ./ w;
zsm = j .* w .* 2 - j .* 1.974E7 ./ w + 125.66;
zh_free = z_fix + zr_mass;

% Characteristic rod impedance
zo = ar .* sqrt(pr .* yr);

% General rod impedances (fixed and SMD boundary conditions)

```

```

r_arg = w .* lr ./ cr;
c = cos(r_arg);
s = sin(r_arg);
t = s ./ c;
zrm = zo .* (zsm + j .* zo .* t) ./ (zo + j .* zsm .* t);
zrbk = zo .* (zsbk + j .* zo .* t) ./ (zo + j .* zsbk .* t);

% Define external impedance (blocked actuator)

zc_blk = zrbk;
zc_m = zrm;
zh_blk = z_fix + zc_blk;
zh_m = z_fix + zc_m;

```

```

% PHI.M

% Looks at the behavior of the transduction coefficient and
% the various defined energy ratios

% Load parameter set

paramet

% Load the electrical impedance (impth)

load temp;

% Open-circuit mechanical impedance

z_mof = z_terf + z_fix + zr_mass;

% Calculate Energy Ratios

% Energy ratios and mechanical dual form transduction coefficient
% k1 based on material properties
% kf derived from two-port network (free actuator)
% kblk derived from two-port network (blocked actuator)

phif = j.* w.*d.*N.*(tan(t_arg)./t_arg).*z_terf./z_mof;
phim = j.* w.*d.*N.*(tan(t_arg)./t_arg).*z_terf./(z_terf+zh_m);

k1 = w .* d.^2 .* yt ./ (w .* u);
kf = phif .^2 .* z_mof .^2 ./ (impth_blk .* z_mof);
km = phim .^2 .* z_mof .^2 ./ (impth_m .* z_mof);

% Plot results

semilogy(ww,abs(kf),ww,abs(km),ww,abs(k1))
title('Energy Ratio Magnitude vs. Frequency')
xlabel('Frequency (Hz)')
% meta twelve

semilogy(ww,abs(kf),ww,abs(k1))
title('Energy Ratio Magnitude vs. Frequency')
xlabel('Frequency (Hz)')
% meta eleven

```

```

% POWER.M
% Investigation of the actuator dissipative power consumption
% Load free and blocked electrical impedances
load temp;
% Load parameter set
paramet
% Choose driving voltage at 15vpp
V = 15;
% Calculate the free and blocked electrical admittances
yef = 1 ./ impth;
yeb = 1 ./ impth_blk;
% Calculate the power consumption
pf = V.^2 ./ 2 .* real(yef);
pb = V.^2 ./ 2 .* real(yeb);
% Plot results
semilogy(ww,pf,ww,pb,'w')
title('Dissipative Power For Free and Blocked Actuators')
xlabel('Frequency (Hz)')
ylabel('Power (watts)')
% meta g
semilogy(ww,yef,ww,yeb,'w')
title('Electrical Admittance for Free and Blocked Actuators')
xlabel('Frequency (Hz)')
ylabel('mho')

```

```

% SINGLELA.M

% Studying the effects of Terfenol-D rod length and cross
% sectional area on actuator stroke and force output

nt = 0.03;
yt = 0.99 .* 20E9 .* (1 + nt .* j);
pt = 9.25E3;
ch = 1 .* sqrt(yt ./ pt);

% Choose operating frequency

ww = 1200;

% Choose appropriate drive level (15vpp)

drive = 15;

% Parameter variation

for z = 1:3
    a(z) = 2.2E-5 + 1E-5 .* z;
    at = a(z);
    for i = 1:50
        l(i) = 0.03 + i .* .005;
        lt = l(i);
        ks = 350393.7 .* (1 + .1 .* j);
        kc = 3.36E8 .* (1 + .005 .* j);
        keq = (ks .* kc) ./ (ks + kc) .* 88;

        ms = 0.001;

%         lt = 0.1524;

%         at = 3.1669E-5;

        kt = at .* yt ./ lt;

        singlep

        imp1_fr = (d^2.*yt.*z_terf./(z_terf+zh_m)).*(tan(t_arg)./t_a
rg);
        imp2_fr = u-d^2.*yt;
        impthm(i,z) = dc_res+j.*w.*N^2.*at.*(imp1_fr+imp2_fr)./lt;

        x4v_m(i,z)=d.*N./impthm(i,z).*(tan(t_arg)./t_arg).*z_terf./((
z_terf+zh_m);

        f3v_m(i,z)= zc_m.*j.*w.*d.*N./(impthm(i,z)).*z_terf./(z_terf
+zh_m).*tan(t_arg)./t_arg;
        f4v_m(i,z) = f3v_m(i,z) ./ (c + j .* zo ./ zsm .* s);
    end
end

% Plot results of parametric study

plot(l,drive .* abs(x4v_m))

```



```
title('Stroke Magnitude at 1200 Hz')
xlabel('Terfenol-D Rod Length')
ylabel('Stroke (m)')
% meta eight
pause

plot(l,drive .* abs(f4v_m))
title('Force Magnitude at 600 Hz')
xlabel('Terfenol-D Rod Length')
ylabel('Force (N)')
% meta nine
```

```

% SINGLEMK.M

% Studying the effects of fixture stiffness and mass variation
%   on actuator stroke and force output

nt = 0.03;
yt = 0.99 .* 20E9 .* (1 + nt .* j);
pt = 9.25E3;
ch = 1 .* sqrt(yt ./ pt);

% Choose operating frequency

ww = 810;

% Choose appropriate drive level (15vpp)

drive = 15;

% Parameter variation

for z = 1:3
    k(z) = 2.5E5 + 0.5E5 .* z;
    ks = k(z) .* (1 + 0.1 .* j);
    for i = 1:50
        m(i) = 0 + i .* .00004;
        ms = m(i);
%       ks = 350393.7 .* (1 + 0.1 .* j);
        kc = 3.36E8 .* (1 + .005 .* j);
        keq = (ks .* kc) ./ (ks + kc) .* 88;

%       ms = 0.001;

        lt = 0.1524;

        at = 3.1669E-5;
        kt = at .* yt ./ lt;

        singlep

        imp1_fr = (d^2.*yt.*z_terf./(z_terf+zh_m)).*(tan(t_arg)./t_a
rg);
        imp2_fr = u-d^2.*yt;
        impthm(i,z) = dc_res+j.*w.*N^2.*at.*(imp1_fr+imp2_fr)./lt;

        x4v_m(i,z)=d.*N./impthm(i,z).*(tan(t_arg)./t_arg).*z_terf./(
z_terf+zh_m);

        f3v_m(i,z)=zc_m.*j.*w.*d.*N./(impthm(i,z)).*z_terf./(z_terf+
zh_m).*tan(t_arg)./t_arg;
        f4v_m(i,z) = f3v_m(i,z) ./ (c + j .* zo ./ zsm .* s);
    end
end

% Plot results of parametric study

plot(m,drive .* abs(x4v_m))
title('Stroke Magnitude at 810 Hz')

```

```
xlabel('Spring Mass')
ylabel('Stroke (m)')
% meta six
pause

plot(m,drive .* abs(f4v_m))
title('Force Magnitude at 810 Hz')
xlabel('Spring Mass')
ylabel('Force (N)')
% meta seven
```

```

% SINGLEP.M

% The fixed parameter set for the actuator output performance
% parameter study

nr = 0.001;
mr = 0.069;
ar = 3.1669E-5 .* 4.8;
lr = 0.05715;
yr = 207E9 .* (1 + nr .* j);
pr = 7801.35;
kr = ar .* yr ./ lr;
cr = sqrt(yr ./ pr);

ne = 0.33;
u = 1.8E-5 .* (1 - j .* ne);
d = 1.6E-8;
N = 2000;
dc_res = 6;

j = sqrt(-1);

% Operating Frequency

w = ww .* 2 .* pi;

% Terfenol impedance calculation

t_arg = w .* lt ./ ch;
t_const = kt .* lt ./ ch;

t_term = -(t_const ./ tan(t_arg)) .* j;
z_terf = t_term .* (1 + j .* nt);

% Actuator fixture impedance (spring and casing)

z_fix = (ms .* w - keq ./ w) .* j;

% External impedance of SMD

zsm = j .* w .* 2 - j .* 1.974E7 ./ w + 125.66;

% Characteristic rod impedance

zo = ar .* sqrt(pr .* yr);

% General rod impedance with SMD boundary condition

r_arg = w .* lr ./ cr;
c = cos(r_arg);
s = sin(r_arg);
t = s ./ c;
zrm = zo .* (zsm + j .* zo .* t) ./ (zo + j .* zsm .* t);

% Define external SMD impedance

zc_m = zrm;
zh_m = z_fix + zc_m;

```

```

% SYS2.M
% Looking at system resonance behavior
% Load parameter set
    paramet
% Define the total equivalent mass
    meq = mr + ms;
% Calculate each frequency equation
    wn_ext = sqrt(keq / meq);
    den = j .* w .* meq - j .* keq ./ w;
    exp1 = j ./ den;
    exp2 = tan(t_arg) ./ (at .* pt .* ch);
% Plot results
    semilogy(ww,abs(exp1),ww,abs(exp2))
    title('Frequency Functions for Terfenol and Fixturing vs. Freque
ncy')
    xlabel('Frequency (Hz)')
    ylabel('Magnitude')

```

```

kt := w / ch
arg := kt * lt
p1 := Tan[arg] / arg
zt := Kt / (I * w * p1)
zf := - I * k / w
zm := I * w * m

c1 := I * w * NN^2 * at / lt
c2 := d * NN * Kt / (I * w)
p2 := 1 / (zt + zf + zm)

zef := c1 * (d^2 * yt * zt * p2 * p1 + ut - d^2 * yt)
tf := c2 * p2 / zef

at := 3.1669 * 10^-5
lt := 0.1524
yt := 20 * 10^9 + (1 + 0.03 * I)
Kt := at * yt / lt
ch := Sqrt[yt / (9.25 * 10^3)]
NN := 2000
d := 1.5 * 10^-8
ut := 1.8 * 10^-5 * (1 - 0.33 * I)

```

# Vita

Anthony E. Ackerman was born on September 12, 1969 at Wright-Patterson Air Force Base in Dayton, Ohio. Having a father in the military, he grew up in several parts of the United States and in Europe. He graduated from William Howard Taft High School in San Antonio, Texas in June 1987 and once again returned to Dayton, Ohio to begin his undergraduate studies in Mechanical Engineering at Wright State University in September of that same year. He finished his Bachelors of Science degree in June 1992 and began his graduate studies at Virginia Tech the following August. Anthony finished his Masters of Science degree in Mechanical Engineering in December 1993. Having had more than enough of education for the present time, he proudly accepted a position with Cummins Engine in Columbus, Indiana instead of pursuing a PhD. He will work in engineering support for their Marketing Department designing electronic control systems and plans to have a great time and be successful. It appears as though his breaking and working on cars through the years paid off in an important way.